AFRL-OSR-VA-TR-2013-0417

Characterization of the Time-Dependent Fluid-Structure Interaction of Passive Flow Control of Low Reynolds Number Membrane Wings

James P. Hubner, Lawrence Ukeiley, Peter G. Ifju and Amy W. Lang

University of Alabama

JULY 2013
Final Report

AIR FORCE RESEARCH LABORATORY
AF OFFICE OF SCIENTIFIC RESEARCH (AFOSR)
ARLINGTON, VIRGINIA 22203
AIR FORCE MATERIEL COMMAND

REPORT DOCUMENTATION PAGE

The public reporting burden for this collection of information is estimated to average 1 hour per response, including the time for reviewing instructions, searching existing data sources, gathering and maintaining the data needed, and completing and reviewing the collection of information. Send comments regarding this burden estimate or any other aspect of this collection of information, including suggestions for reducing the burden, to the Department of Defense, Executive Services and Communications Directorate (0704-0188). Respondents should be aware that notwithstanding any other provision of law, no person shall be subject to any penalty for failing to comply with a collection of information if it does not display a currently valid OMB control number.
PLEASE DO NOT RETURN YOUR FORM TO THE ABOVE ORGANIZATION.

1. REPORT DATE *(DD-MM-YYYY)*	2. REPORT TYPE	3. DATES COVERED *(From - To)*

4. TITLE AND SUBTITLE

5a. CONTRACT NUMBER

5b. GRANT NUMBER

5c. PROGRAM ELEMENT NUMBER

6. AUTHOR(S)

5d. PROJECT NUMBER

5e. TASK NUMBER

5f. WORK UNIT NUMBER

7. PERFORMING ORGANIZATION NAME(S) AND ADDRESS(ES)

8. PERFORMING ORGANIZATION REPORT NUMBER

9. SPONSORING/MONITORING AGENCY NAME(S) AND ADDRESS(ES)

10. SPONSOR/MONITOR'S ACRONYM(S)

11. SPONSOR/MONITOR'S REPORT NUMBER(S)

12. DISTRIBUTION/AVAILABILITY STATEMENT

13. SUPPLEMENTARY NOTES

14. ABSTRACT

15. SUBJECT TERMS

16. SECURITY CLASSIFICATION OF:			17. LIMITATION OF ABSTRACT	18. NUMBER OF PAGES	19a. NAME OF RESPONSIBLE PERSON
a. REPORT	b. ABSTRACT	c. THIS PAGE			
					19b. TELEPHONE NUMBER *(Include area code)*

Final Report: Characterization of the Time-Dependent Fluid-Structure Interaction of Passive Flow Control of Low Reynolds Number Membrane Wings

Executive Summary

A collaborative effort of researchers at the University of Alabama and the University of Florida investigated the unsteady fluid-structure interaction and passive flow control of fixed, flexible membrane wings in low Reynolds number flows. Fluid dynamic research of low Reynolds flows (10,000 – 100,000) over lifting surfaces and plates usually experiences separation near or at the leading-edge, creating an aerodynamic shear layer that either reattaches to form a separation bubble due to shear layer transition or remains unattached and separated (Carmichael, 1981; Lissaman, 1983; Mueller, 1999). Lifting surface designs employing highly flexible membranes have shown that the membrane can greatly modify the separated region, demonstrating beneficial effects (Ifju *et al.*, 2006; Shyy *et al.*, 2007; Albertani *et al.*, 2007; Song *et al.*, 2008; Hu *et al.*, 2008; Rojratsirikul *et al.*, 2009). Both time-averaged and dynamic deformations of the membrane can produce flow curvature or increased momentum transfer, delaying or limiting the extent of flow separation and corresponding wake size, which advantageously affects the resulting aerodynamic forces.

To better understand the flow physics that underpins these advantageous characteristics and extract the temporal nature of the fluid-structure coupling and to better understand how this coupling can passively control the flow, the investigators developed and used synchronized, point-wise and planar, time-resolved experimental techniques to measure the flow features (thermal anemometry and particle image velocimetry) and surface deflections (laser vibrometry and dynamic visual image correlation). The use of synchronized surface deflection and planar flow measurements represented an important, critical development of this program by combining experimental technologies and creating a unique tool that provides a foundation for a much larger class of fluid-structure problems. The program focused on free trailing edge, low-*AR* membrane wings (2 – 5) in low-*Re* flow (25,000 – 75,000) with various applied pre-strain levels (<10%). Abudaram *et al.* (2013) describes a new pre-strain fabrication technique using silicon rubber developed as part of the investigation.

A common phenomenon of low-*Re* membrane wings is the flow-induced, large-amplitude vibration (sometimes referred to as flutter) of the membrane. This vibration is substantially larger for free trailing-edge geometries compared to perimeter constrained geometries (fixed trailing-edge), enabling greater interaction with the flow. Trailing-edge scalloping decreases the vibration intensity, decreasing drag and increasing aerodynamic efficiency (Hubner and Hicks, 2011). In the post-stall region, where most prior studies are conducted, the fluidic driver and resulting vibration frequencies are likely related to blunt-body shedding. However, for lower incidences, prior to full separation and blunt-body shedding, the vibration characteristics are driven by the membrane. Before the onset of visible, large-amplitude vibration (or limit cycle oscillations—Johnston *et al.,* 2010), small amplitude vibrations with characteristic fundamental frequencies related to membrane properties exist. Initially, the amplitude energy increases with aerodynamic dynamic pressure but the frequency remains relatively constant. This is an indication that the overall energy in the flow is exciting the resonant frequency of the membrane. If the vibration was driven by a specific fluidic feature, for instance vortical shedding, then the membrane fundamental frequency would change as the flow phenomena frequency changed with increased flow velocity. It is not until an onset condition (Scott *et al.,* 2012) is achieved that a shift (increase) in the frequency occurs due to aerodynamic tensioning. At this condition, the effect of the membrane vibration is detectable in the shear layer.

High-speed, time-synchronized particle image velocimetry (PIV) and digital image correlation (DIC—also referred to as visual image correlation, VIC), Timpe *et al.* (2013), shows that the vibration frequency of peak energy increases with angle-of-attack and membrane pre-tension for low angles-of-attack, prior to the onset of stall conditions. At higher angles-of-attack, the frequency shows less dependency on pre-strain and angle-of-attack. In this post-stall region, the rate of tensioning of the membrane decreases due to stall, and, here, the membrane becomes more susceptible to blunt-body shedding. At low angle-of-attack, however, flat plates do not exhibit strong blunt-body shedding, thus, is an unlikely driver. Additionally, shedding is a relatively constant Strouhal number phenomenon, predicting a decrease in frequency due to the increase of the projected chord as angle-of-attack increases—the opposite trend to what is measured. Thus, this is another indication that the membrane is driving the flow.

The time-average separation region substantially decreases, resulting in wakes with smaller peak deficit velocities but a wider wake footprint. Peak Reynolds shear stress levels above the center-cell membrane shift upward into the shear layer and wake for the free TE membrane geometry, highlighting how the passive flow control increased the turbulent momentum transport in the region downstream of the membrane. This is a result of the increased momentum transfer induced by the membrane TE shedding or releasing vorticity into the separated region. Time-resolved measurements show how the development of counter-clockwise (positive) vorticity forming at the membrane TE and the higher momentum flow above the shear layer is being pulled downward. High correlation values exist between the flow field and the membrane vibration. As the angle-of-attack is increased, the region of highly correlated, in-phase motion diminishes in intensity and moves away from membrane, indicating less effectiveness of the membrane interaction with the flow. This evolution is consistent with the previous findings. Namely, for relatively low angles-of-attack, the membrane motion is driven by the membranes natural frequency which is due to the combination of pre-tension and aerodynamic tensioning (as well as membrane properties), and this vibration is forcing the features in the wake. The integrated effect of the modified flow field is increased lift, particularly in the post-stall region, and increased aerodynamic efficiency if the trailing-edge is scalloped to reduce undesirable, low-tensioned oscillation of the TE. Zhang *et al.* (2013a) shows these trends are affected by the vibration of the membrane and not solely the time-averaged shape. The aerodynamic response of membrane wings is compared to 3D printed wings in the shape of the time-averaged membrane displacement for five different low *AR* configurations and various angles-of-attack and dynamic pressures. In most cases, the membrane wing outperformed the printed wing.

A simplified model (Zheng *et al.*, 2013b) of the flow-induced membrane vibration assumes the membrane to be a vibrating 2D membrane tensioned in the spanwise direction. The vibration of the membrane is related to the applied pre-strain (non-uniform), aerodynamically-induced strain (dynamic pressure, angle-of-attack), material properties (modulus of elasticity, isotropy), and geometry (thickness, cell shape). Because the strain is relatively low, less than 10%, it is modeled as the linear summation of applied pre-strain and aerodynamically-induced strain. To model the effect of aerodynamic loading, the 2D membrane analogy is expanded by assuming a uniform pressure loading that produces a catenary membrane shape. The distributed aerodynamic loading is estimated by either aerodynamic lifting-line theory or experimental data. The new model shows that aerodynamically-induced strain is proportional to the lift coefficient to the power of 2/3 and can range from $0 - 10\%$ for typical flat plate membrane models in low-Re flow. Two distinct regions of membrane vibration relative to the tensioning aeroelastic parameter exist: for highly tensioned membranes ($\Pi_2 > 2$) the nondimensional frequency was relatively constant but for moderately tensioned membranes ($\Pi_2 < 2$), the nondimensional frequency was inversely related to the relative membrane tensioning.

Contents

Nomenclature

a	=	lift-curve slope
AR	=	aspect ratio
b	=	wing span
b'	=	membrane cell span
c	=	wing chord or characteristic length
c'	=	membrane cell chord
C_D	=	drag coefficient
C_L	=	lift coefficient
C_l	=	lift coefficient per unit span
d	=	particle size or membrane displacement
E	=	membrane modulus of elasticity
f	=	frequency
I	=	cross-sectional area moment of inertia
L	=	lift or characteristic length
L'	=	lift per unit span
m	=	mass
M	=	lens magnification
N	=	number of samples
q	=	dynamic pressure
Re	=	chord-based Reynolds number
St	=	chord-based Strouhal number
t	=	time or membrane thickness
T	=	tension
u,v	=	streamwise and vertical velocity components: $u = \bar{u} + u'$
U,U_∞	=	free stream speed
w	=	membrane loading due to pressure and weight or equivalent width
W	=	weight
α	=	angle-of-attack
ε	=	average spanwise membrane strain (unless designated otherwise with subscript)
λ	=	taper ratio
Π_1	=	stiffness-dominated aeroelastic similarity parameter: $\left(\frac{Et}{qc}\right)^{1/3}$
Π_2	=	tension-dominated aeroelastic similarity parameter: $\frac{\sigma t}{qc}$
ρ	=	density or cross-correlation coefficient
σ	=	average spanwise membrane stress or standard deviation of a measure
τ	=	Glauert correction factor for lifting-line theory $f(AR,\lambda)$ or nondimensional time
ω	=	spanwise vorticity (unless designated otherwise with subscript)

Introduction

Motivation

Micro air vehicles (MAVs) are envisioned to play an important role in the Air Force's comprehensive, integrated sensor network (satellites, conventional aircraft, UAVs, ground stations, etc.) that provides mission-critical information anytime and anywhere (Miller, 2007). The US Air Force goal by 2015 is to introduce their first generation MAVs that are the size of birds and, then, the size of insects by 2030 (Madhani, 2008; Wilson 2009). A new generation of agile MAVs and small UAVs employ flexible (passive) and morphing (active) wing structures in fixed- and flapping-wing designs to improve flight performance such as endurance, disturbance alleviation and maneuverability. Because of the small size of the vehicles, rapid in-house fabrication and quick evaluation of global characteristics is possible. This feedback is important, especially for the validation of novel vehicle designs and the development of flight controllers; however, a better understanding of the complex fluid and structural dynamics that lead to enhanced performance is necessary for vehicle design beyond *ad hoc*, trial-and-error approaches. The flow field is quite complicated and includes—especially in the nonlinear flight regimes—flow separation, transition and reattachment, turbulence, vortex shedding, tip vortices, three dimensional flow along with structural deformations and vibrations. An improved understanding of the fluid-structure interaction (FSI) of highly-flexible membrane wings at low Reynolds number will lead to a superior means to design passive wing control strategies that produce advantageous flight qualities. At the time of the proposed research effort, the majority of the existing research has focused on rigid, two dimensional airfoil geometries with some recent investigations with flexible geometries and dynamic response. As such an in-depth investigation of the FSI has been conducted, particularly focusing on geometries with unattached trailing-edges and the resulting aerodynamic benefits and passive control mechanisms.

Background

MAV designs generally fall under three areas: fixed, flapping or rotary wing. Typical fixed wing MAV designs (Mueller *et al.* 2006)—the primary interest of this proposed effort—must deviate from conventional high-*Re* wing designs due to phenomenological flow issues as well as weight/sizing constraints. Lissaman (1980) and Laitone (1997) have demonstrated deteriorated performance effects of high-*Re* airfoils at low *Re*. For *Re* between 30,000 and 200,000 (Carmichael 1981, Mueller 1999), the incoming laminar boundary separates nearer the leading-edge and either reattaches forming a separation bubble due to shear layer transition or remains unattached. The presence and size of the separation bubble, or the lack of reattachment, greatly affects the airfoil performance. Factors such as surface roughness, pressure gradient, free stream turbulence and wing planform/camber influence the formation of separation bubbles and, thus, aerodynamic performance (Torres and Mueller, 2004; Aki *et al.* 2006; Lian and Shyy, 2006;).

Passive flexibility incorporated in fixed-wing MAV wing designs has shown to improve deleterious effects of flow separation, improving performance and disturbance alleviation. Shyy, Jenkins and Smith (1997) demonstrated a hybrid airfoil design, a conventional airfoil shape with a latex sheet mounted on top of a curved wire upper surface mesh that improved lift-to-drag characteristics in unsteady (gusting) conditions. A significant amount of research has been performed by Ifju *et al.* (2001, 2005 and 2006) using passively flexible wing designs (< 2% thickness, moderate camber) in which extensible membranes were attached to carbon-fiber frames. Assessment of flying quality (Jenkins *et al.,* 2001) between rigid and flexible wings showed lower frequency pilot input control for flexible wings, even in gusting environments. Their biologically inspired wing designs have the ability to passively

control geometric twist (batten reinforced wing) or aerodynamic twist (perimeter reinforced wing), which can improve longitudinal stability and increase maximum lift. The out-of-plane deformations due to aerodynamic loading on the membranes indicate the ability of the wing to create adaptive washout or adaptive billowing, respectively (Albertani *et al.*, 2007). For both wing designs the static longitudinal stability was increased compared to a rigid wing of the same geometry.

Researchers at the University of Florida and the University of Michigan (Shyy *et al.* 2005; Lian and Shyy 2006; Stanford *et al.* 2007 & 2008) have developed numerical models of the static aeroelastic response and theoretical tailoring of the configuration; however, limited static experimental results are available to validate much of their efforts. While qualitative trends were generally matched, discrepancies exist due to model infidelity arising from turbulence effects, unsteady flow, massively separated regions and membrane wrinkling. Rojratsirikul *et al.* (2009) studied the flow-induced oscillations of a 2D reinforced membrane (rigid leading- and trailing-edge) in low-*Re* flow. Coupling was indicated between unsteady flow and membrane oscillations, suggesting that the flexibility may have caused a smaller separated region, a decrease in drag and a delay in stall. Gordnier and Attar (2009) developed an implicit LES simulation of 2D flexible membrane wing studied by Rojratsirikul at transitional Reynolds numbers. The numerical simulation showed good qualitative agreement with the available experimental data; however, better experimental structural characterization of the membrane was deemed necessary.

Hu *et al.* (2008) studied the effect of wing flexibility by adjusting batten spacing on the wing (*Re* = 70,000) and leaving the trailing-edge free. The tension of the membrane (batten spacing) proved to be a contributing factor in the aerodynamic performance of the wing; although, it was not explicitly characterized. Since the membrane was not constrained at the trailing-edge (but not scalloped either), sparse spacing of the battens provided less tension upon aerodynamic induced deflection, causing a trailing-edge "fluttering effect" that decreased aerodynamic performance. These measurements provided some insight into the flow over passively extensible wings; however, characterization of the structural deformation is necessary for a more complete picture of the effects of the flexibility.

Mastramico and Hubner (2008) characterized the wake profile behind high-*AR* plates (to minimize spanwise effects) with various membrane geometries that included repeating perimeter, batten and batten-scalloped cells (Fig. 1). The scalloped geometry mimics the scalloping seen on bats (Swartz *et al.* 2007). For these tests, the *Re* = ~50,000 and $\Pi_1 = 4$. Significant differences existed in the wake deficit and turbulence intensity. The free trailing-edge geometries, at sufficient *Re* (> 20,000), exhibited significant vibration. The scalloped geometry showed a consistent decrease in the wake profile and turbulence intensity and increase in fluctuation frequency for both flat and cambered plates, especially when approaching stall. While the wake profile was broader than the solid model, the deficit was much lower. Spectral analysis of the measurements showed strong, well-developed, spatially-bimodal frequency peaks and harmonics at low angle-of-attack (α < 16°) but not at higher angles-of-attack. At angles below and around stall (α ~ 4°-12°), the peak frequency values were relatively constant with angle-of-attack. The fluctuations initiated at a *Re* > 20,000 and the peak frequency scaled relatively linearly with velocity, showing a tensioning effect. The peak frequency was relatively independent of the chordwise depth of the cell but increased as the cell spanwise width was decreased. Peak frequencies do appear in the perimeter reinforced geometry, but only at higher angles-of-attack when the flow was fully separated.
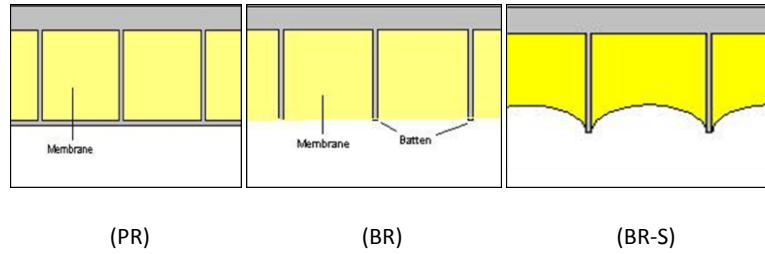
<div align="center">(PR)   (BR)   (BR-S)</div>

Figure 1. Perimeter, batten and batten-scalloped reinforced geometry

Abudaram *et al.*, Ifju (2009) reported on a detailed series of wind tunnel tests aimed at obtaining a relationship between structural deformation and aerodynamic performance for fixed, flexible MAV wings. In addition to varying the cell size of the flexible membrane, the stiffness of the carbon-fiber supporting structure was investigated as well. The investigators showed that extremely thin battens can provide substantial trailing-edge washout, with peak twist at 50% of the semi-span. Conversely, thicker battens were unable to alleviate these flight loads through twist and showed a sizeable spanwise bending whose severity increased with batten thickness and dynamic pressure. Increasing the distance between battens led to a sustained vibration along the membrane's trailing edge once a critical dynamic pressure was exceeded. This generally decreased the pre-stall lift, but for some cases, showed higher post-stall lift spikes.

Objectives

At the time of the proposed effort, the prevailing research associated with low-*AR*, low-*Re* wings was focused on static structural and aerodynamic measurements. Some unsteady characterization was reported, but results were limited and not sufficient for model development and validation. Surface deformation features were linked to aerodynamic performance, and the geometry and extent of passive flexibility was shown to improve performance metrics: decreased drag, increased maximum lift, delayed stall, gust alleviation. These investigations were fruitful but, by their design, did not reveal the fundamentals of the FSI and how this interaction may or may not assist in the improvement or detriment of global performance parameters.

Thus, our primary objective of this investigation was to understand and extract the temporal nature of fluid-structure coupling and how this coupling passively controls the flow on low-*AR* wings with extensible membranes in low-*Re* flow. To complete this objective, we proposed to develop and use synchronized, point-wise and full-field, time-resolved experimental techniques to measure the flow features (thermal anemometry and particle image velocimetry) and full-field surface deflections (laser vibrometry and visual image correlation). The use of synchronized surface deflection and planar flow measurements represented an important, critical development of the program, combining experimental technologies and creating a unique tool that would provide a foundation for a much larger class of fluid-structure problems. Estimation and modeling of both the flow field and the structure would be used as necessary to develop a detailed understanding of how the flexible membranes interact with the flow. The experiments would also provide high-fidelity benchmark datasets available for validation of computational tools.

Attention was focused on thin airfoils (nominally 2-3%) with free trailing-edge membranes in low-*Re* flow typical (25,000 − 75,000). Membrane extensibility, Π_1 , ranged from 3 to 8 and aspect ratio, *AR*, ranged from 1 to 5. The effort included the following tasks

(1) surface/flow visualization and force-moment surveys to assist in the definition of preferred geometries, to characterize surface separation and reattachment on models, and to assess the effectiveness of preferred geometries and tailored passive control strategies,

(2) synchronized constant thermal anemometry (CTA) and laser vibrometry (LV) to establish a linkage between the separated shear layer/trailing-edge wake and the vibration of the surface membrane,

(3) synchronized, time-resolved, full-field flow-structure measurement using particle image velocimetry (PIV) and visual image correlation (DIC) to further characterize and understand the configurations that exhibited coherent fluid-structure interaction in part (2),

(4) detailed correlation/spectral analysis and estimation of the flow properties related to the surface deflections, and

(5) characterizing structural parameters and planform geometry to assist in the coupling with the flow for enhanced performance characteristics.

Experimental Facilities and Test Articles

The experiments were conducted in facilities at the University of Alabama and the University of Florida. The measurements involved aerodynamic loads, velocity fields (over the wing and in its wake) and surface deformations. The following section overviews the facilities, equipment and models used in the investigation.

UA Facilities

<u>Wind Tunnel</u>

The UA wind tunnel is an open-circuit, closed test section facility. The test section is 1.82 m long and has width and height of 0.76 m. The air is moved by a centrifugal fan upstream of the reservoir which is then diffused, feeding a reservoir with a honeycomb flow straightener and four flow conditioning screens. Before entering the test section the flow is accelerated through a contraction section with a 4:1 ratio. The flow speed ranges from 2 to 22 m/s, and the centerline free stream turbulence intensity is less than 0.7% at 5 m/s and 0.5% at 10 m/s. The angle-of-attack of most tests ranged from -4° to 22° at 2° increments (±0.2°).

<u>Force Measurement</u>

Aerodynamics forces were measured with a calibrated, six-component load cell (*ATI Industrial Automation* Nano17) connected to an 8-channel strain gage module (*National Instruments*, SCXI 1520). The test model was attached to the load cell by a small, streamlined connecting plate. The resolution of the force measure was 0.006 N. The voltage data from the load cell were acquired at the rate of 1 kHz for a total time ranging between 2 s. The closed test section wake- and solid-blockage corrections were estimated using a simplified correlation by Shindo (1995). At the highest angle-of-attack for the largest

AR test plate, the corrections C_L and C_D were 2.5%. The estimated uncertainty in the force coefficient measures based on manufacturer resolution and measured precision at 95% confidence were 0.06 for *AR* =2 and *Re* = 25,000 (worst case) and 0.004 for *AR* = 5 and *Re* = 75,000 (best case).

High-speed Imagery

High speed imaging of the membrane vibrations was one technique used to quantify the frequency. Video clips were captured with a *Vision Research* MIRO EX2 camera. A typical movie included a total of 5,000 images captured at rates between 800 fps (640 x 480 resolution) and 1900 fps (320 x 240 resolution). The video clips were imported into an image processing software package to measure the fundamental frequency of the vibration. This was accomplished by monitoring the intensity change of the high contrast 12 membrane markers within specified regions of interest and calculating the corresponding power spectrum of the time-intensity trace.

UF Facilities

Wind Tunnel

The Aerodynamic Characterization Facility (ACF) is an open-jet, open-return wind tunnel specifically designed to work in the low-*Re* regime. The flow environment available in the open-jet test section has relatively low-turbulence steady flow in the 1-20 m/s range. The tunnel is powered by a 1.52 m diameter, 37.3 kW axial blower, combined with variable frequency drive. Flow entering the wind tunnel is straightened by a metal honeycomb section and passes through multiple settling screens to further remove the organized turbulence before it is contracted through an 8:1 area ratio resulting in a 1.07 m by 1.07 m square jet test section of 3.05 m length. The flow has been characterized with 0.16 percent turbulence intensity in the streamwise velocity at the 10 m/s working velocity. A more detailed description of the ACF, including flow uniformity measurements, can be found in Albertani *et al*. (2009).

Open-Jet Flow Facility

Synchronized hotwire anemometry and laser vibrometry measurements were conducted in the potential core of a 15.3 cm x 15.3 cm open-jet flow facility. The jet is capable of maintaining steady free stream of speeds between 1 and 15 m/s. The potential flow core is 12 cm wide 15 cm downstream of the exit. Centerline free stream turbulence intensity (FSTI) was evaluated via hotwire anemometry at the center of the jet's core flow region 15 cm downstream and oriented parallel to the spanwise axis. Centerline FSTI at test conditions between 1 and 3 m/s is nominally 2.7 to 1.3%, respectively. At higher free stream velocities, the turbulence intensity is 0.5 to 0.7%. Test articles were suspended within the jet flow downstream of the jet's exit plane via two optical posts located outside of the jet flow. The connection between the optical posts and test article permitted free adjustment while allowing the airfoil to be locked at a given angle-of-attack.

Synchronized Laser Vibrometer and Hotwire Measurements

To assess FSI between membrane and its surrounding flow field, single-point flow velocity and membrane vibration velocity measurements were recorded via a hotwire (HW) anemometer and laser vibrometer (LV), respectively. Hotwire anemometry was performed via a constant temperature

anemometry system (*Dantec* 55M) with a cylindrical single wire probe oriented parallel to the test article's leading edge. The hotwire probe was placed within the leeside free shear layer. The vibrometer's scanning head (*Polytec* PSV-400) was located below the test article and was manually positioned to align the beam on any point of interest on the windward side (underside) of the membrane. Typically, the vibrometry measurement point on a test article's surface was along the cell's spanwise centerline and located beneath the hotwire probe position.

To relate temporal events of the membrane vibration to oscillation of the surrounding flow field, hotwire and vibrometer measurements were simultaneously sampled via the laser vibrometry system's analog-to-digital (A/D) card (*National Instruments* PCI-6154). The raw hotwire signal was decoupled into separate AC and DC components and passed through a two channel low-pass filter (*Stanford Research System Model* SR640) to prevent aliasing. Signal decoupling was implemented to improve the measurement resolution, thus, enabling maximum signal amplification within A/D card range limits. Throughout testing, the signals were acquired at 2560 Hz. Frequency domain transforms were generated by ensemble averaging results from 100 1.6 s data sets recorded at each test point. This window size provided 20+ convective scales at 1 m/s and 40+ cycles for the lowest vibration frequency Velocity averages and standard deviations were calculated from the total time-domain data set recorded at each test point.

Synchronized DIC and PIV Measurements

Developing a synchronized DIC-PIV measurement technique was a significant achievement of the research effort and enabled unique full-field synchronized flow and membrane displacement measurements. This DIC system consisted of two high speed CMOS cameras (*Vision Research* Phantom v7.1). The cameras had a maximum frame rate of 4800 Hz at full resolution of 800 x 600 pixels and were equipped with aspherical 28-300 mm *f*-length lenses set to *f*/# = 5.6. The camera control and image processing was performed with *Correlated Solutions* VIC-3D 2006 and VIC-Snap as well as *Vision Research* Phantom Camera Control v675.2. The software calibrated the stereo setup and performed digital image correlation, obtaining three-dimensional membrane displacements. A small amount of paint was used to create random speckle patterns on the membrane surfaces and gray-scale cross-correlation analyses compared images of the deformed membrane to a reference image.

Cubic B-spline interpolation was used to achieve sub-pixel accuracy, while normalized sum of squared differences (NSSD) correlation criterion was used for its insensitivity to scales in lighting. The membrane region was divided into subsets of 25 pixels square with 5 pixel step size, providing a spatial resolution in *x* and *z* (stream and spanwise directions) of 0.64 mm between data points. Out-of-plane (or *y*) membrane displacement calculations were accurate to ±0.1 mm based on static displacement tests. Membrane displacements were calculated normal to an automatically-generated reference plane (based on the reference image) through the geometric center of the reference membrane position. For the low pre-tension model, due to membrane sag, post-processing techniques were implemented to set the reference plane parallel with and flush to the model surface, correcting for small deviations. Once the reference plane was set, displacements were normal to the model surface and knowledge of model markers and angle-of-attack were used to rotate and translate the DIC data into the PIV reference frame for combined plotting.

Preliminary high-speed imaging was used to detect the membrane vibration frequency range from 40 to 100 Hz. As such, a sampling rate of 800 Hz was used to minimize aliasing membrane motions and to capture the time dependence of membrane shape changes. Typically 1600 samples were

obtained at each angle-of-attack, while certain cases for the ε = 1.3% wing utilized synchronized DIC/PIV and the sample count was fixed to that of the PIV system.

Flow field measurements were acquired with a time-resolved (TR) PIV system (*Dantec Dynamics*). This system consisted of a Series 800 double-cavity Nd:YAG laser (Lee Laser) set to a wavelength of 532 nm and two high-speed CMOS cameras (*IDT* XS-5) equipped with 105 mm *f*-length macro lenses set to *f*/# 2.8. The TR-PIV system was sampled at 800 Hz which resulted in the cameras being set to a reduced total pixel count of 1280 x 600 pixels. The time delay for image pairs was set to Δt = 60 µs for all cases. The cameras were oriented normal to the flow field to obtain PIV in 2D fashion over the model and in the near wake. One camera was positioned such that the field of view (FOV) investigated flow directly above the model while the other was positioned aft, with a slightly larger FOV, to focus on the immediate wake. The FOV of the model camera was 8.9 x 4.2 cm while the wake camera FOV was 11.9 x 5.6 cm.

Dantec software (*Dynamic Studio* v3.10) was used to compute two-component vector fields in the light sheet plane through a three-step iteration, adaptive-window, and cross-correlation algorithm. Interrogation areas were reduced each pass from 128 by 128 pixels to a final of 16 by 16 pixels, using a 25% overlap. This created vector fields with spatial resolutions of 1.18 vectors/mm for the model view and 0.89 vectors/mm for the wake view, while the grid resolution was ~2% of chord. Due to a broadening wake and shear layer size at α = 24°, the cameras' resolutions were set to full (1280 x 1024 pixels) and data were acquired at 450 Hz for these cases. For α < 24°, 1024 PIV samples were obtained at each angle-of-attack, while 814 were acquired for α = 24°.

Atomized olive oil seed particles with vendor quoted diameters, d_p, of 1-5 µm were generated with an aerosol generator (ATI Technologies tda-4B). Under Stoke's flow assumption for very small diameter spheres and where $\rho_p \gg \rho_f$, (*f* represents fluid density, $\rho_f \approx$ 1.20 kg/m^3, while *p* represents the particle density, $\rho_p \approx$ 970 kg/m^3), the relaxation time, τ, of these particles was estimated to be 2.8E^{-5} s (~30 kHz) and is sufficient for the flow scales resolved and investigated. Diffraction will cause the reflected light to spread as an Airy disk, and the diffraction limited particle size calculation, d_s, is defined in Prasad (2000). With the combination of seeding and optics, the diffraction limited particle size is approximately the effective particle size. With *M* being the lens magnification (0.16 on average for these experiments), d_s was estimated at 4.2 µm or approximately 1/3 the size of a pixel (12 µm). Hence, the images were slightly defocused to increase the imaged particle size to offset pixel locking effects. The low lens *f*/# of 2.8 was required to allow sufficient light to the sensors.

Reference image background removal (reducing sensor noise), vector validation and outlier rejection were utilized to enhance the vector accuracy for data sets. Free stream flow values computed by PIV were compared with Pitot measured values to ±0.1 m/s or within 1%. From Bendat and Piersol (2010), the inherent random error is shown to scale as $\frac{1}{\sqrt{N}}$. Using *N* ≥ 800 samples, random error is expected ≤ 3.5%. Running statistical analysis showed first- and second-order flow statistics converged to ±2% with 800 samples in recirculating and highly fluctuating regions.

Force Measurement

In the ACF, aerodynamic forces were measured via a custom-built MC-0375 six-component strain gage force balance (*Allied Aerospace*). Data was acquired with a *NI* SCXI 1520 8-channel strain gage module. The resolution of the force measure was 0.02 N. The leading-edge of the model was mounted to the force balance via a streamlined 5 cm aluminum stand-off located at the center span of

the wing as discussed above. The force balance was connected via a sting to a two degree-of-freedom pitch-plunge apparatus that allowed PC-controlled angle-of-attack positioning. Angle-of-attack sweeps were designed such that the leading-edge of the model was kept aligned with the tunnel centerline. The force-balance data acquired at the rate of 1 kHz for 10 s. The angle-of-attack the tests ranged from -6° to 50° at 2° increments (±0.3°). Hysteresis was checked and determined to be negligible. A drag correction for the model stand-off between the test plate and the force balance was estimated by measuring the zero angle-of-attack drag (without the test plate) and subtracting it from the drag measurement for each test condition. The ACF open test section wake- and solid-blockage effects were considered as outlined by Rae and Pope (1984). Corrections to C_L and C_D were less than 1%. The estimated uncertainty in the force coefficient measures based on manufacturer resolution and measured precision at 95% confidence was 0.014 for the test conditions.

Test Articles

    <u>Membrane Wings</u>

        A baseline description and designation of the membrane wings are presented in this section. For some tests, this baseline was altered, and these changes are described in the corresponding Results and Discussions section. Most of the membrane wings were fabricated from rectangular aluminum (7075-T6) frames with silicone rubber (*McMaster-Carr* 86435K) adhered to the surface. Typical models are shown Fig. 2. Depending on the wing and cell aspect ratio, the wing contained from 1 to 9 cells. Cell aspect ratio (cell span to cell chord: b'/c') ranged from 0.5 to 2.0. For most models, the length of the cell chord was 80% of the wing chord, creating a rigid leading edge that extended 20% of the chord. For all models, the wing chord was 7.62 cm, the battens (or ribs) were 0.32 cm and the thickness was 0.21 cm. At the trailing edge, the membrane was scalloped in the shape of circular arc with a depth of 20 to 25% of the cell span. Scalloped membranes were used because of the increased aerodynamic efficiency compared to unscalloped membranes (Hubner and Hicks, 2011). Silicon rubber was used in most tests being a more durable and consistent membrane compared to latex rubber. Additionally, the black color of the silicon rubber greatly improved the imaging environment for laser-based flow measurements. The nominal modulus of elasticity and thickness of the silicon rubber membrane, tested in-house, were nominally 385 kPa (+/- 5%) and 0.34 mm (+/- 2.5%), respectively. In the synchronized laser vibrometer/hotwire tests, some latex rubber (Thera-Band) specimens were tested: 1.36 MPa (+/- 5%) and 0.102 mm (+/- 2.5%). In various figures throughout the report, the color black represents the silicone rubber membrane and the color yellow represents the latex rubber membrane.
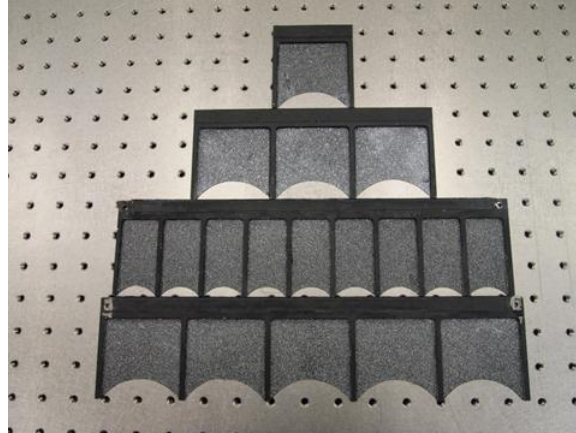
Figure 2. Image of the membrane (silicone rubber) test articles; underside

<u>Model Fabrication</u>

The membrane model fabrication procedure (Abudaram *et al.*, 2013) is shown schematically in Fig. 3. First, a random speckle pattern is applied on the silicone membrane via flat white spray. The paint has a negligible reinforcement effect on the membrane. The silicone membrane is then repeatedly (approximately 10 times) heated up to ~200 °C and cooled down to ~0 °C to eliminate effects of hysteresis. Because silicone rubber does not easily adhere on any surface by nature, a silicon adhesion primer (*GE Silicones* SS4155 01P) was applied on the frame surface at room temperature. Application of the silicone primer was through filter paper, providing a more even distribution of the primer. After waiting for the solvent in the primer to evaporate for approximately 30 minutes, the two parts of raw silicone (*Dragon Skin* Shore 20A) were mixed in a separate cup to immediately attach the membrane on the frames (the pot life of raw silicone mixture is 15 minutes at room temperature) at the desired elevated temperature. At higher temperatures (150-200 °C), the raw silicone cures quickly (~1 s). The cure time increases as the attachment temperature decreases; therefore, for lower temperatures the frame/membrane assembly sat together for longer durations to ensure a proper cure before cooling. Images were acquired with increments of 20°C during the cooling process.

To heat the silicone membrane uniformly, a commercially available hot-plate was combined with an aluminum plate manufactured to fit inside the hot-plate. The aluminum plate was spray coated with a flat black paint to increase the surface emissivity for the infrared thermometer. To capture the amount of expansion and contraction of the membrane, two DIC cameras are positioned above the specimen and remained stationary throughout the experiments, each at a different viewing angle. Before acquiring each image, the temperature of the membrane was measured with an infrared thermometer that has a sensitivity of ±1 °C between 10 °C to 30 °C and outside that range a sensitivity of ±1.5 °C.

All the deformations were measured using DIC. The main concept of DIC is to evaluate the displacement field by tracking deformations of a sample with an applied random speckling pattern to its top (Sutton *et al.*, 1986). The cameras were calibrated employing a calibration grid which enabled the re-positioning of the test bed anywhere within the field of view. Two video cameras (*RETIGA* 1300) were connected to the controlling PC via firewire, and a synchronization unit was installed to capture images simultaneously. Images were digitalized via a standard acquisition board and processed (*Correlated*

Solutions DIC3D-2007). Accurate gray-value interpolation schemes were implemented to optimize sub-pixel accuracy (Scheirer *et al.*, 2000). A post-processing option of calculating the in-plane strains (ε_{xx}, ε_{yy}, and ε_{xy}) was executed. The strain resolution of the DIC system is estimated to be 300µε.

Highlighting the steps as shown in Fig. 3:

Step 1: A speckle pattern is applied to the membrane. Then an initial image of the speckled membrane at room temperature is acquired as a reference.

Step 2: The membrane temperature is elevated on an aluminum hot plate. For this investigation, a 50 mm thick aluminum plate was placed on a commercial hot-plate to effectively diffuse heat from the hot-plate coils in a uniform field. Temperature and uniformity was measured with a hand-held infrared thermometer that had an accuracy of ±1.5 °C over the surface of the hot plate.

Step 3: The membrane is attached to the frame using silicone adhesive.

Step 4: Images of the membrane are acquired as it cools to room temperature at desired intervals, leading to a temperature-strain calibration curve.

Step 5: Images of the membrane are acquired after it cools to room temperature.

Step 6: Membrane overhangs are cut and another picture is acquired at room temperature.

Step 7: Optional (performed for technique evaluation): the membrane is cut from the frame and a final image is acquired to assess hysteresis.

Step 1
Room Temperature:
Speckle membrane and
acquire initial field
for reference

y   x
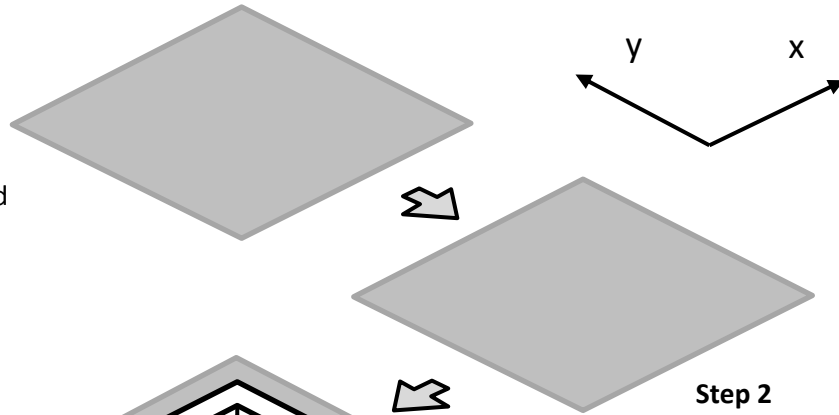
Step 2
Elevated Temperature:
Measure deformation

Step 3
Elevated Temperature:
Attach frame and
measure deformation
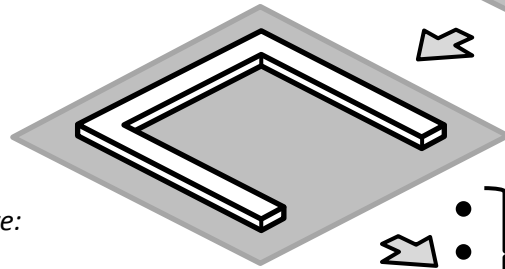
Steps 4
Cool Down:
Measure deformation
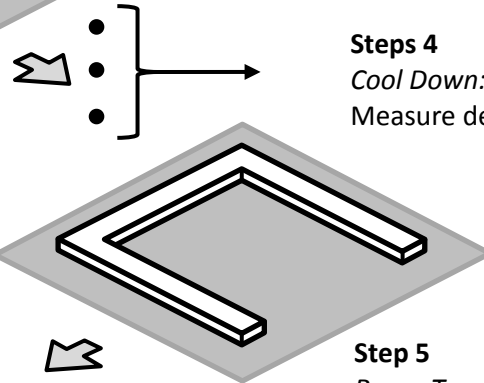
Step 5
Room Temperature:
Measure deformation

Step 6
Room Temperature:
Cut trailing edge and
measure deformation
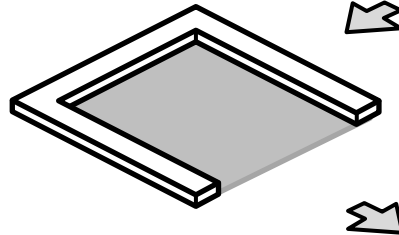
Step 7 (optional)
Room Temperature:
Cut membrane from
frame and measure
deformation
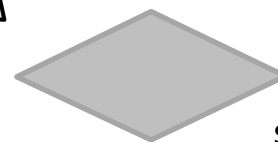
Figure 3. Method to measure pre-tension on membranes using DIC system

16

Results and Discussions

Assessing Model Pre-tension (Abudaram *et al.*, 2013)

The thermal expansion coefficient of the silicon rubber was verified by placing a sample of black silicone rubber with a white speckling pattern unto the hot-plate and acquiring thermally-induced strain measurements with the DIC system. A plot of the strain results against various temperatures from approximately 40°C to 200°C is shown in Fig. 4. The slope of the line was calculated to be $2.8E^{-4}$/°C, typical of silicone rubbers. Also shown, as a check of the technique, is the thermal expansion response of ultralow expansion (ULE) glass.
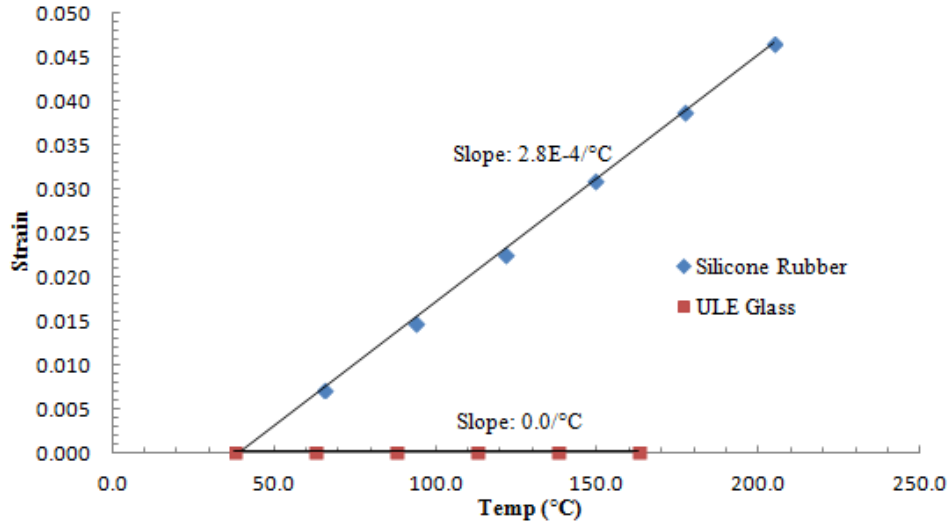
Figure 4. Strain vs. temperature plot for silicone rubber (diamond) and ULE glass (square)

Strain results are presented for a membrane attached at 140°C to an open frame with the inner dimensions of 2.5cm by 2.5cm in Figs. 5-7. Strains were computed at the increments of 20°C for this particular experiment. At the 140°C free expansion state, the membrane was uniformly expanded in both directions. Once the specimen was cooled to room temperature, a symmetric strain field developed, predominantly in the spanwise direction. The spatially-averaged strains at each step were calculated and plotted in Fig. 8. A similar procedure was repeated for the attachment at 100°C and 180°C. The same procedure was repeated five times to determine the margin of error and repeatability of the experiments; standard deviation bars are drawn in Figure 8. At 140°C the average strains in the x- and y-directions for free thermal expansion were computed to be within three significant figures of each other. The slight difference in two directions after attachment may be caused by the raw silicone (adhering agent) flow when the frame was pressed down. Average strain values in the y-direction decreased linearly during the cool down process due to the open geometry of the frame, which is not constricted at one end. Average strain values in x-direction were relatively constant as the membrane movement is restricted in the x-direction. This effect is diminished when the experiment is conducted with a perimeter reinforced model. Initially, a large amount of hysteresis was observed. The effect of hysteresis (about 0.5% strain) was greatly diminished by cooling and heating the silicone about 20 times before conducting the experiments.

17
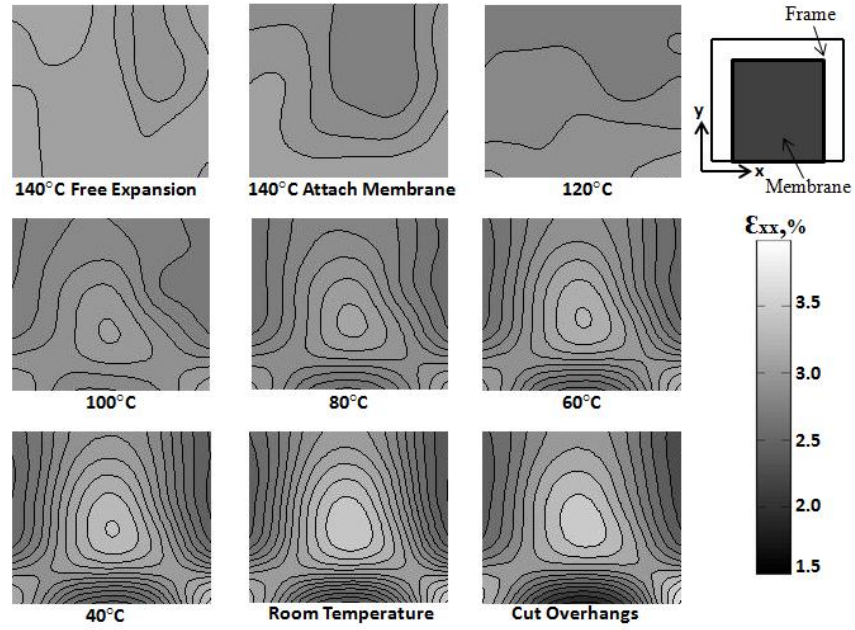
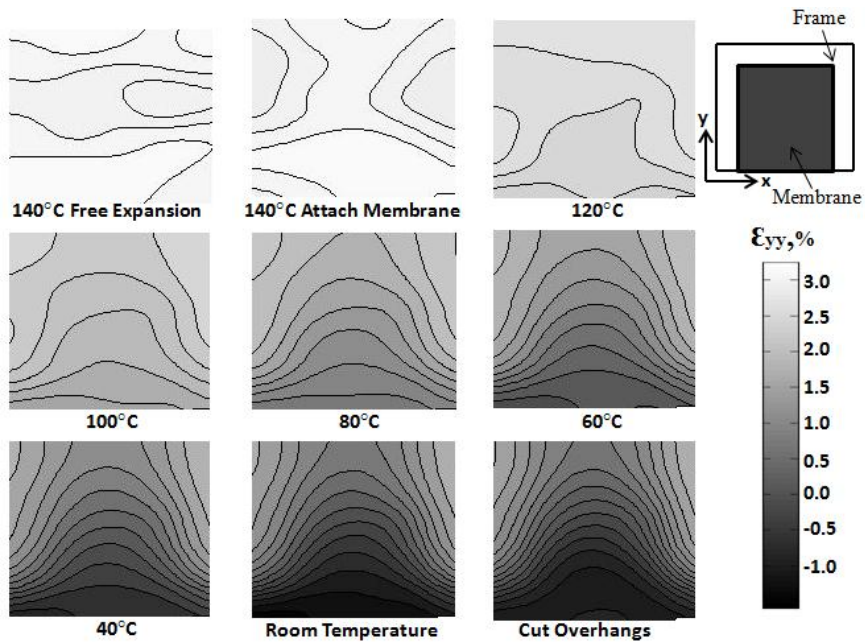**Figure 5.** Normal strain in x-direction (spanwise) when attached at 140°C for the open frame model

Figure 6. Normal strain in y-direction (chordwise) when attached at 140°C for the open frame model
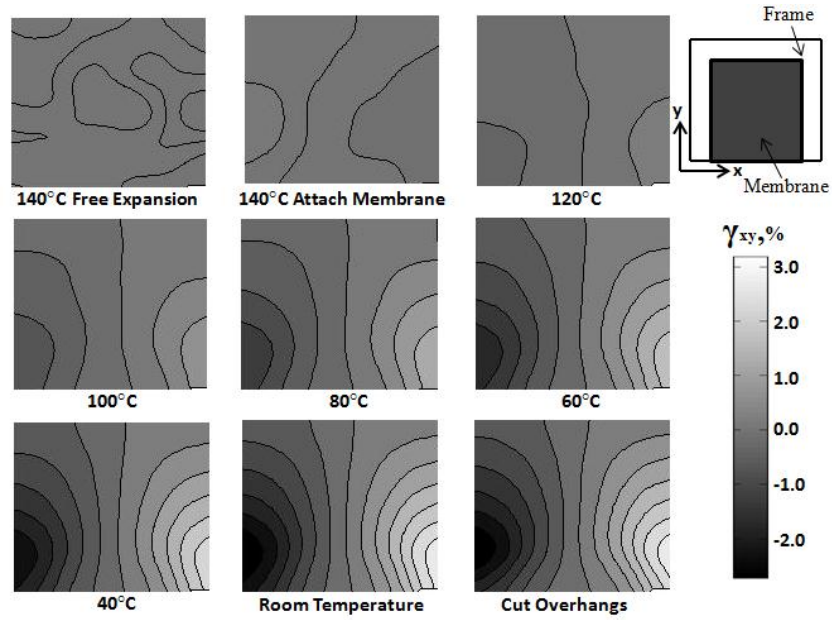
18

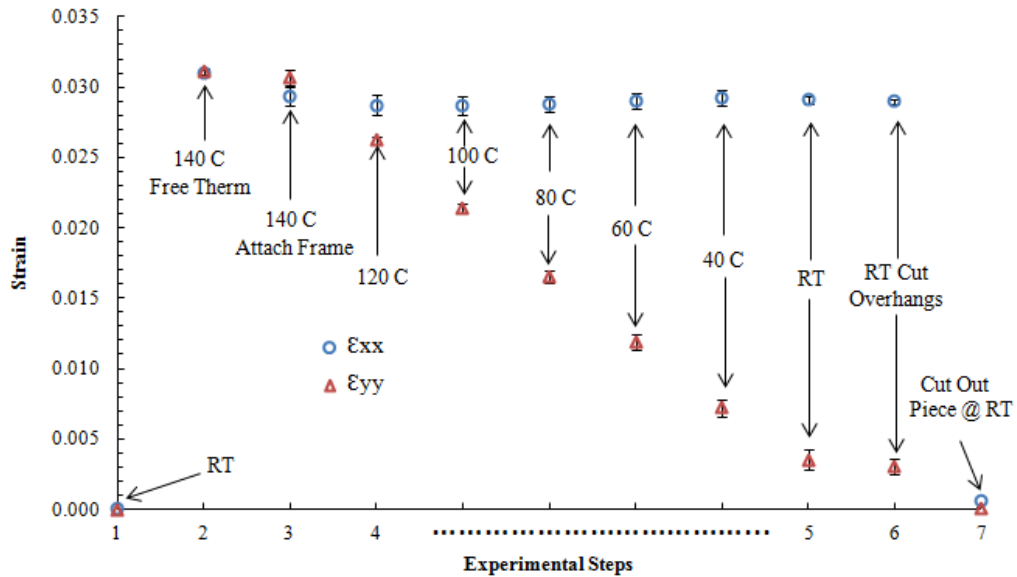**Figure 7.** Shearing Strain when attached at 140°C for the open frame model

Figure 8. Average strain versus experimental steps plot when attached at 140°C for open frame model

The same procedure was conducted by attaching the silicone at 100 °C and 180 °C and each additional experiment was repeated three times. Then the specimen was allowed to cool down to room temperature and the average stress values were plotted as seen in Figure 9. Quadratic regression lines enabled the desired tension to be set within approximately 17 kPa on average in the spanwise direction for the given geometry.
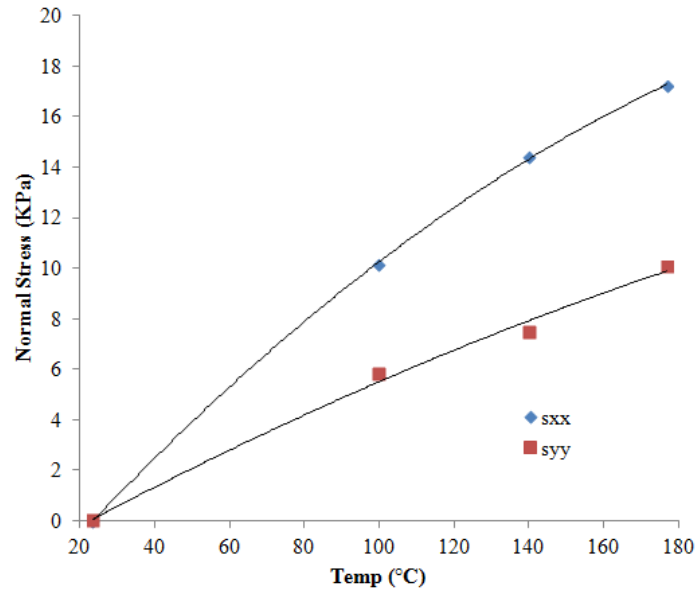
Figure 9. Average normal stresses versus temperature for the open frame model

The stress plots shown in Figure 9 for normal and shear were achieved using Hooke's law for isotropic elasticity utilizing the previously calculated values for elastic modulus and Poisson's ratio, along with the strains that were computed with the DIC system. A more uniform stress distribution is perceptible in the x-direction compared to the y-direction as the frame is constrained by the two legs of the frame; however, because the frame is open in the y-direction, the free edge exhibits no stress. The center line of the shearing stress image has no shearing stress while two extreme values (±5.5 KPa) are detected symmetrically on both corners.

To compare to a perimeter-reinforced frame (no free edge), a second frame was constructed out of carbon fiber with the same inner dimensions of 2.5cm by 2.5cm, adhered on sides and elevated to 180 °C. Stresses (Fig. 11) are plotted for the perimeter-reinforced frame. The perimeter-reinforced frame is fairly uniform in both directions; however, slightly greater strains in the x-direction are observed in comparison to y-direction, which could be due to the different flow of adherent agent. Nevertheless, approximately zero shear stress is reported on the surface of the silicone membrane, which confirms the uniformity of stress distribution. Figure 12 shows that the averaged strains for the perimeter-reinforced frames in both the x and y directions are relatively constant as temperature is decreased. Compared to the open frame (Fig. 9), the average chordwise strain is much larger for the perimeter-reinforced frame.
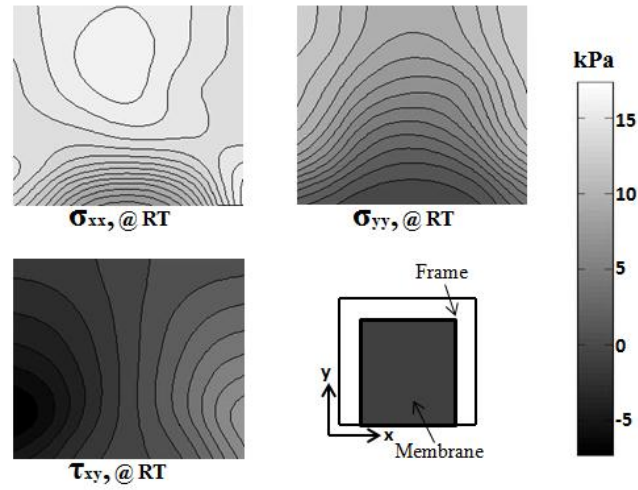
Figure 10. Stress plots in x- and y- direction along with shearing stress at room temperature for open frame when attached at 140°C
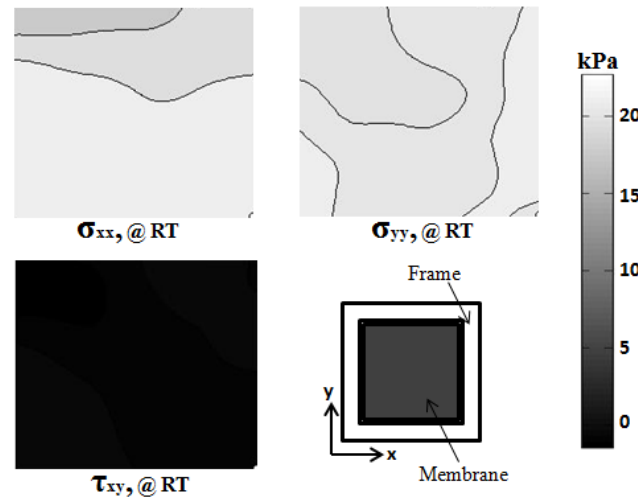
Figure 11. Stress plots in x- and y- direction along with shearing stress at room temperature for perimeter reinforced frame when attached at 180°C
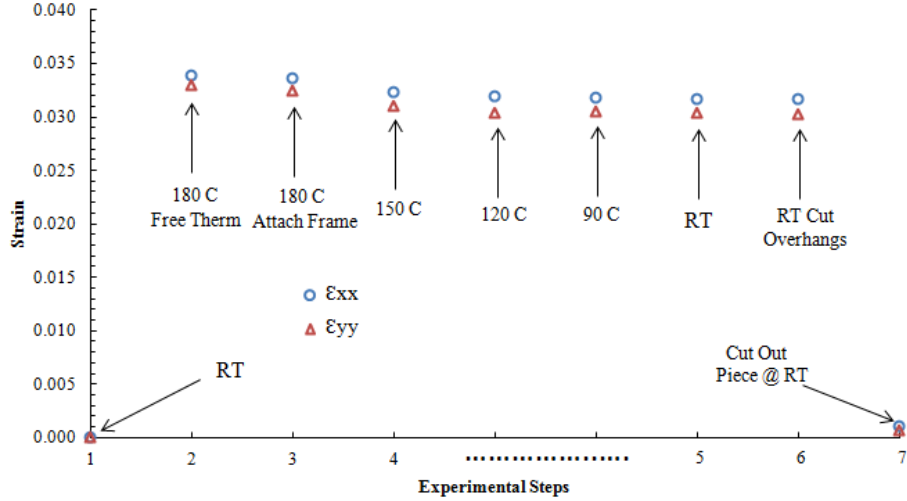
Figure 12. Strain versus experimental steps plot when attached at 180°C for perimeter reinforced model

Onset of Membrane Vibration (Scott *et al.,* 2012)

As a test procedure was formalized to attach and quantify (post-attachment) the strain-field of tensioned membranes to metal frames, the investigation initially surveyed the vibration of a free trailing-edge membrane with no applied pre-tensioning except for the self-weight of the membrane. Figure 13 presents our initial test configuration for vibration onset tests in the open-jet flow facility. The single-cell, flexible-membrane plate consisted of a rigid frame with a single rectangular cutout centered along the frame's span and extending forward from the frame's trailing edge. The aluminum frames were 0.21 cm thick with a chord of 7.62 cm (3") and a span of 38.1 cm (15"). The membrane chord was 80% of the plate chord and the membrane span was 80% or 40% the plate chord. Both silicone rubber (black) and latex (yellow) membranes were tested.

While the *AR* = 5 frames extend, in the spanwise direction, beyond the potential core of the open-jet flow, the potential core is twice as wide as the larger cell span, enveloping the membrane. The *Re* for the 7.62 cm chord ranged from 5000 to 50,000 (1 to 10 m/s at standard sea level atmospheric conditions). Most tests were conducted at 8° angle-of-attack. At this angle, reattachment for a rigid plate is near the trailing-edge. At higher angles the lift curve slope decreases, but still pre-stall, and drag starts to substantially increase. Thus, aerodynamic efficiency (lift/drag) generated by the membrane are generally maximum near this angle. For all tests discussed, it was desired to locate the hotwire probe within the shear layer emanating from a test article's leading-edge.
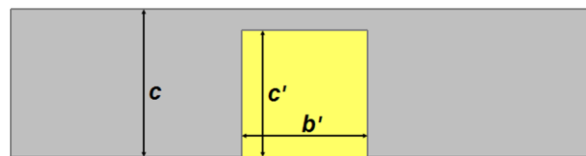

Figure 13. Generic test article geometry

22

<u>Shear Layer Size and Probe Placement</u>

To determine specific hotwire placement locations, measurements starting near the surface (at 20% and 60% of the chord) and traversing perpendicular to the free stream were performed for a solid, flat plate—identical geometry (chord and thickness) but without a cell cutout. The free stream velocity was 10 ± 0.2 m/s. Beginning at a 1 mm offset from the surface, hotwire measurements were recorded at 1 mm increments. Two metrics were used to estimate shear layer size and subsequent hotwire placement within the shear layer where turbulent fluctuations are the largest: velocity magnitude and standard deviation. Because a single wire sensor aligned parallel to the leading-edge was used, velocity vector decomposition and direction was not possible, leading to apparent but false interpretation of no flow reversal at higher angles-of-attack. However, vector decomposition was not the intent of the scan and the rectified magnitude of velocity indicated in Fig. 14 includes the contribution of a vertical component as well as the streamwise component. Figure 14 displays (a) the mean, u, and (b) standard deviation, u_{std}, velocity magnitudes relative to the free stream speed, U, for the probe traversed vertically starting at 0.6c. As angle-of-attack increases, the free stream flow speed is reached at a greater offset distance above the surface. Present in the shear layer is a maximum in the velocity magnitude standard deviation (b), driven by the vertical velocity gradient (a). For 8°, a displacement of 6 mm (0.08c) from the airfoil surface was chosen for the 0.6c location downstream from the leading-edge.

(a)   (b)
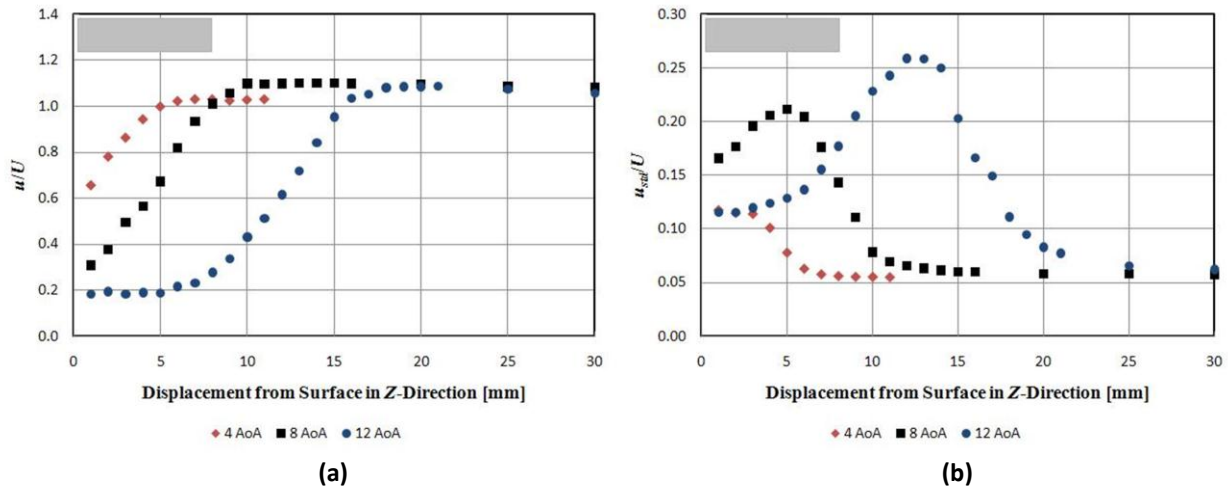
Figure 14. Solid plate shear layer sizing at 0.6c: (a) relative mean velocity magnitude, (b) relative velocity standard deviation.

To measure the effect of a vibrating membrane on the leeside shear layer, the 80x80 latex model was tested at 10 m/s with an 8° angle-of-attack. Figure 14 compares the results with those of the flat plate. Comparing (a) the velocity magnitude and (b) the velocity fluctuation, the shear layer above the membrane plate is closer to the undisturbed surface and the fluctuation energy with the shear layer is less than that of the solid plate under similar conditions. This observation is consistent with prior reports (Song *et al.*, 2008; Rojratsirikul *et al.,* 2009) and demonstrates the potential for improved aerodynamic efficiency.

A series of tests were performed via laser vibrometry to determine the natural frequency of each test article membrane. Each test article was positioned and secured as if flow testing was to be

23

performed. The laser vibrometer was focused on the 0.6c measurement point (middle of the membrane). While the wind tunnel was powered-off, membrane vibration was recorded as the membrane was excited by manually tapping the aluminum frame and swiping the surface of the membrane itself. Although each test article was fabricated initially without applied pre-tension, self-weight induced strain (on the order of 0.1%) enabled measurement of a natural frequency. While multiple energy peaks were measured, indicating the complex nature of the vibration and potential frequency coupling in flow (as well as artifacts of the testing technique), the larger energy peaks from each excitation method occurred at consistent frequencies across multiple trials for a given test article. The natural frequencies (frequency of maximum energy, ±0.5Hz) for each test article are listed in Table 1, where wings with a black insert represent the silicon membrane and wings with a yellow insert represent the latex membrane.
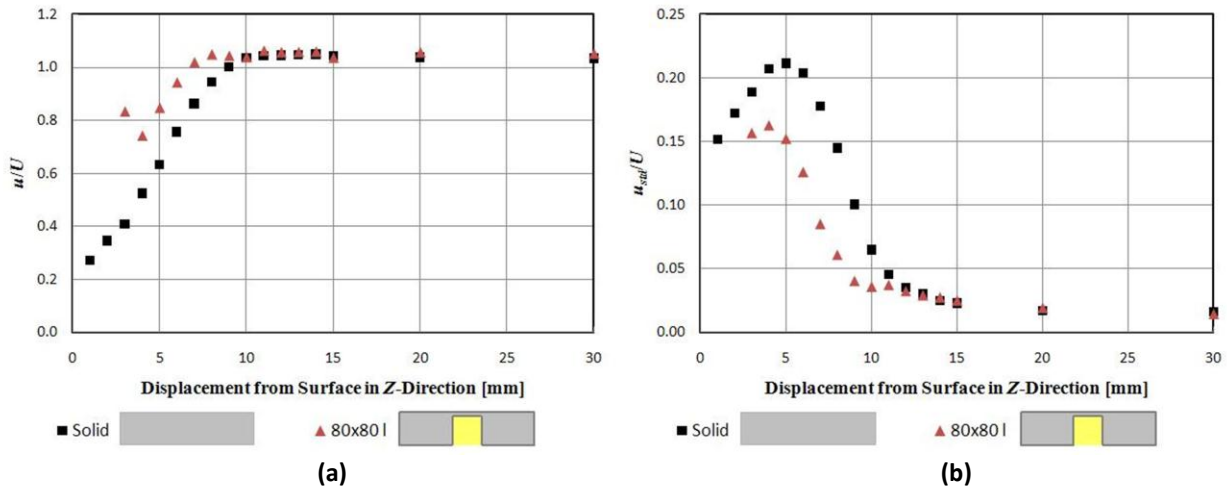
Figure 15. Shear layer size comparison between solid plate and 80x80 latex membrane at 8° angle-of-attack: (a) relative mean velocity magnitude, (b) relative velocity standard deviation

Table 1. Membrane airfoil natural frequency.

Test Article		Natural Frequency[*] ± 0.5 Hz
80x80 s		42.5
40x80 s		80.6
80x80 l		25.6
40x80 l		44.4

Comparing the effect of geometric and material properties on the peak frequencies presented in Table 1, the silicon rubber and the shorter span geometry have higher natural frequencies. The latter is

rather intuitive when considering that a simple vibrating beam or string has a higher frequency for a shorter length. As shown in the previous section regarding the induced strain field of free trailing edge membranes, the strain is dominant in the spanwise direction. The material effect (considering membrane thickness as a material property) is less intuitive: the silicon rubber has a lower modulus but higher thickness. The product, Et, which is often used in a measure of membrane stiffness relative to the product of dynamic pressure and wing chord (Shyy *et al.*, 2007), is about the same for the two materials. However, the natural frequency of the silicon rubber is nearly double that of the latex. Further expanding the simple beam analogy, noting the over-simplification of the geometry and the exclusion of tension, the theoretical natural frequency is proportional to

$$f \propto \sqrt{\frac{EI}{mL^3}},$$ (1)

where I is the cross-section area moment of inertia, m is the mass and L is the characteristic length. Substituting the cell geometry, c' and b', and the membrane thickness, t, yields

$$f \propto \sqrt{\frac{Ewt^3}{\rho t c'(b')^4}} \propto \frac{\sqrt{E}t}{\sqrt{\rho}(b')^2}\sqrt{\frac{w}{c'}},$$ (2)

where ρ is density and w represents an equivalent beam width which would be a function of the cell aspect ratio, b'/c'. Thus, for the same cell geometry and noting that the density for both materials is approximately the same (~1 g/cm^3), the natural frequency is simply proportional to $\sqrt{E}t$. Based on the values from Table 1, the calculated frequency ratio due to the material differences (silicon rubber-to-latex) is 1.76. This agrees well with the experimental results of 1.82 for the 40x80 geometry and 1.66 for the 80x80 geometry (an average of 1.74).

To estimate the geometric effect on the natural frequency (same material), Eq. 2 reduces to

$$f \propto \frac{1}{(b')^2}\sqrt{\frac{w}{c'}},$$ (3)

but the value of w is not easily approximated. Another approach for estimating the geometric effect would be to consider that membrane as half of a rectangular membrane bounded on all four sides. Exploiting symmetry, the effective chordwise and spanwise lengths are $2c'$ and b'. The natural frequency of a rectangular membrane is proportional to (Rossing and Fletcher, 1995)

$$f \propto \sqrt{\frac{1}{(2c')^2} + \frac{1}{(b')^2}} = \frac{1}{b'}\sqrt{\frac{(b')^2}{4(c')^2} + 1}.$$ (4)

Substituting the cell span and chord yields a geometric frequency ratio (40x80-to-80x80) of 1.84. This too agrees reasonably well with the experimentally measured values of 1.73 for the latex and 1.90 for the silicon rubber (an average of 1.82).

<u>Membrane Spectra</u>

Membrane flutter onset (and subsequent limit cycle oscillations) is readily observable but varies with free stream speed depending on material and geometric properties. Figure 16 shows two images of the 80x80 s membrane. Each airfoil was positioned at 8° angle-of-attack and the flow speed was varied. Images were recorded at 500 fps via a 1280 x 1024 pixel resolution (PIV cameras). The left image was acquired at a free stream speed of 3 m/s and no large amplitude vibration is visible. The right image was acquired at 4 m/s and clearly large amplitude deflection indicating a limit cycle oscillation was present at

the trailing-edge. Based on the videography technique and free stream intervals of 1 m/s, the onset velocity for each configuration is listed in Table 2.
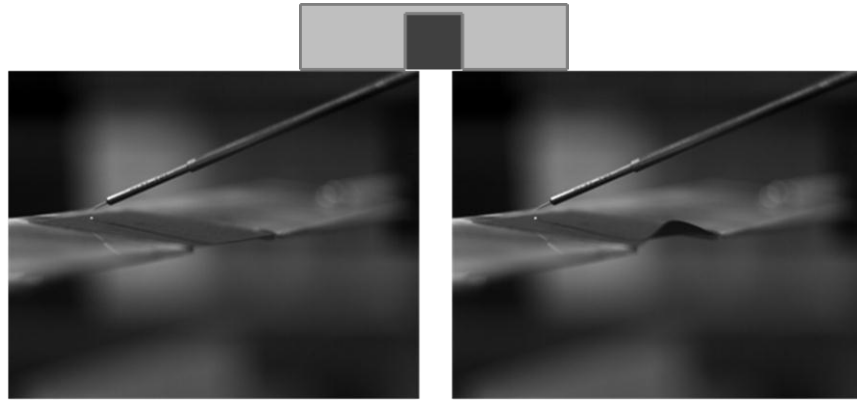

Figure 16. Visual vibration onset of 80x80 silicone rubber: left – 3 m/s; right – 4 m/s

Table 2. Membrane airfoil fundamental frequency

Test Article		Visual Flutter Onset Velocity ±0.5 m/s
80x80-s		4
40x80-s		8
80x80-l		2
40x80-l		2

To assess membrane vibration amplitude, power spectral density (PSD) characteristics of the membrane velocity were compared at multiple free stream velocities. Vibrometry measurements were recorded at 0.6c for each test article. A PSD plot was generated for each data ensemble and, then, averaged to produce those presented in Fig. 17. While multiple peaks are present, indicating membrane vibration, a dominant peak clearly exists. As the free stream velocity increases, the global energy level at all frequencies increases. For the 80x80-s configuration (upper left chart, Fig. 17), the fluctuation energy increases significantly between 2 m/s (no flutter visualized) and 4 m/s (flutter onset). Membrane vibration, though, clearly exists at 2 m/s (f_{pk} = 42 Hz), as detected by the vibrometer. Comparing to the results in Table 1, this low-level peak is the natural frequency of the membrane dictated by the membrane properties, geometric shape and self-weight tension. As velocity (or dynamic pressure) increases, flutter initiates at the natural frequency and increases in frequency as indicated by the rightward shifts in the frequency peaks.

Visually, vibration amplitude is highest at the trailing-edge, and the trailing-edge vibrated out-of-phase with the leading portion of the membrane. The increase in frequency is due to the tensioning of the membrane at higher dynamic pressure. This velocity-frequency trend is present in all the plots, noting that for the 40x80-s membrane (upper right chart, Fig. 17) the onset—visually—does not occur until 8 m/s; thus, the frequency is constant while the membrane is vibrating at lower speeds. While not measured in this investigation, Johnson *et al.* (2010) measured a slight increase vibration amplitude with increasing free stream speed. If initial pre-tension exists, as in the case of Johnston *et al.* (2010), the onset flutter condition can be delayed. For self-weight pre-tensioned membranes, Hubner and Hicks (2011) showed that the frequency-velocity trend scales linearly during post-flutter limit cycle oscillations. Comparing the two membrane materials, visual flutter detection corresponded to a peak energy of at least ~0.01 $m^2s^{-2}Hz^{-1}$ for the silicon rubber membranes and ~0.0001 $m^2s^{-2}Hz^{-1}$ for the latex (thinner, less mass) membranes.
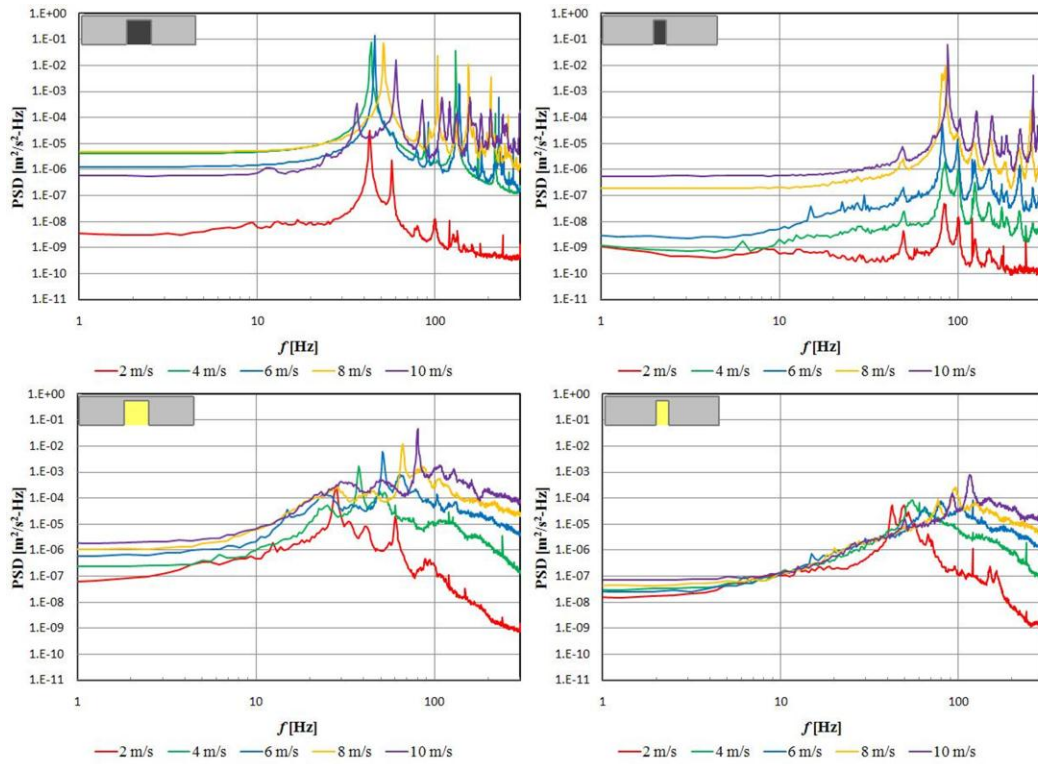

Figure 17. Velocity power spectral density (PSD) obtained from the membrane vibrometer measurements at multiple free stream velocities: 0.6*c*, 8°

<u>Velocity Spectra</u>

Figure 18 consists of velocity magnitude PSD plots obtained from the hotwire probe placed in the shear layer for each test article over a range of free stream speeds. For the silicon rubber specimens, membrane-induced flow oscillation is characterized by a sharp spectral peak or peaks in the PSDs. The 40x80-s configuration (upper right chart, Fig. 18) is a good example. A sharp spectral peak in the flow is present at (U = 10 m/s; also exists for the 9 m/s case not shown). At lower velocities ($U \leq 8$ m/s) prior to flutter onset, no characteristic peak in the flow at the membrane vibration frequency is present. Clearly,

at the hotwire measurement location above the LV measurement point and within the middle of the leeside shear layer, the membrane-induced vibrations have not created flow disturbances greater than the overall turbulent energy within the shear layer. As shown by the 80x80-s data (upper left chart, Fig. 18) where the onset condition is ~4 m/s, higher velocities (higher dynamic pressures) correspond to a shift in the fluidic spectral peak to higher frequencies. The lower mass latex membranes, interestingly, do not always show the existence of sharp flow fluctuation peaks once membrane flutter onset appears. The 40x80-l membrane (lower right chart, Fig. 18) shows no discrete spectral peaks in the flow despite visual and measured membrane limit cycle oscillations at 2 m/s and higher. The 120 Hz spectral peak at 2 m/s is believed to be an electronic interference artifact. For the 80x80-l configuration (lower left chart, Fig. 18), flow fluctuation peaks at the same frequency of the membrane exist for 4 m/s and higher. At this flow velocity, the peak spectral energy of the membrane vibration has reached ~0.01 $m^2s^{-2}Hz^{-1}$. This level of membrane energy is not achieved in any of the 40x80-l cases.
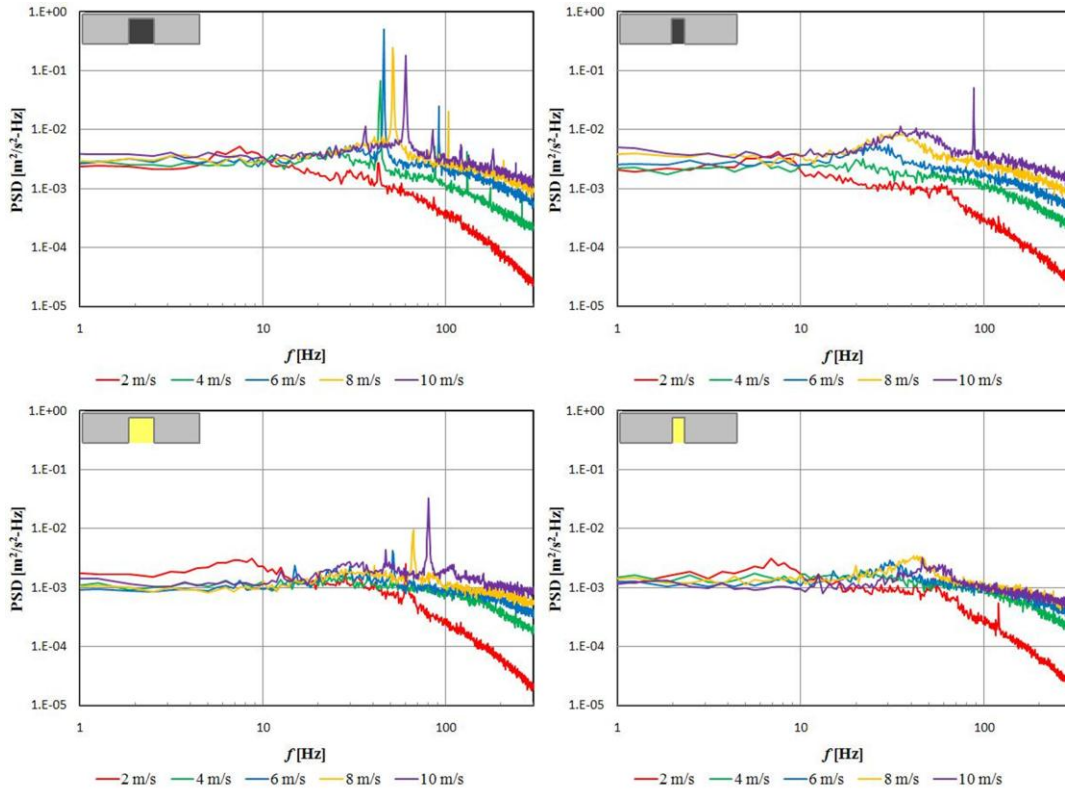

Figure 18. Velocity power spectral density (PSD) obtained from the hotwire placed in the shear layer at multiple free stream velocities: 0.6c, 8°

Coherence Measurement

Simultaneous sampling of hotwire anemometer and laser vibrometer measurements permitted coherence analysis between the two time-resolved data series. Coherence assessment between the two is a measure to which the structural and fluidic responses are related. Thus, the coherence plots depicted in Fig. 19 can be interpreted as the relative significance of fluid-structure interaction pre- and post-flutter onset. For values of coherence above 0.5, membrane-induced flow fluctuations are readily detectable via the hotwire. High coherence exists for $U \geq 4$ m/s for the 80x80-s membrane, $U \geq 9$ m/s for the 40x80-s and $U \geq 8$

m/s for 80x80-l membrane. The fluid-structure coupling between airfoil membrane and the flow for these cases is more likely to influence global aerodynamic characteristics. Small membrane vibration, which was present at all low velocities due to extraneous flow or environment disturbances, produces low coherence with surrounding flow, implying that these vibrations were not of sufficient strength to propagate into the flow.
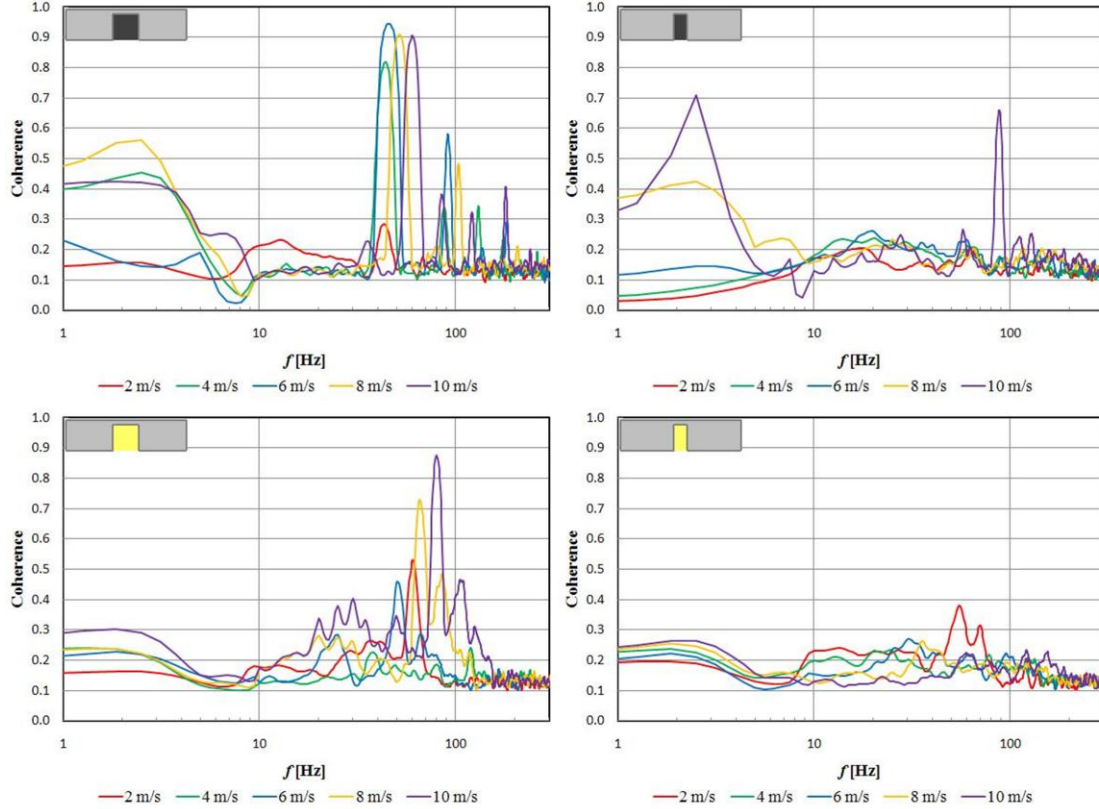

Figure 19. Hotwire-vibrometer coherence at multiple free stream velocities: 0.6*c*, 8°

Aerodynamic Lift and Drag Characterization (Zhang *et al.*, 2012; Zhang *et al.*, 2013a)

Force Coefficient Trends

For the force coefficient figures within this section, the open symbols represent data from the UF wind tunnel and the filled symbols represent data from the UA wind tunnel. Figures 20 through 22 display the lift coefficient, drag coefficient and lift-to-drag ratio, respectively, for two tensioned, multi-celled models (*AR* = 4.3): a 5-cell silicone rubber membrane with 2.8% pre-tension (circle symbols) and the 5-cell silicone rubber membrane with 1.3% pre-tension (triangle symbols). Also plotted are the results of a rigid flat-plate (square symbols). As evident in Fig. 20, the lift trend is initially linear for all models and agrees fairly well with traditional bound circulation theory for finite wings. Then as the angle-of-attack approaches 10°, the initial onset of stall (or pre-stall region) decreases the lift curve slope substantially, while still being positive, and a broad, shallow stall region exists over the next 20°. Maximum lift occurs around 25 to 30°. This is typical for low *AR*, low *Re* rigid wings as discussed in (Torres and Mueller, 2004; Okamoto and Azuma 2011). Clearly, the benefit apparent in the figure for the

membrane wings is the increase in lift relative to the rigid wings: ~20% at 10° and ~25% at 25° (stall region).
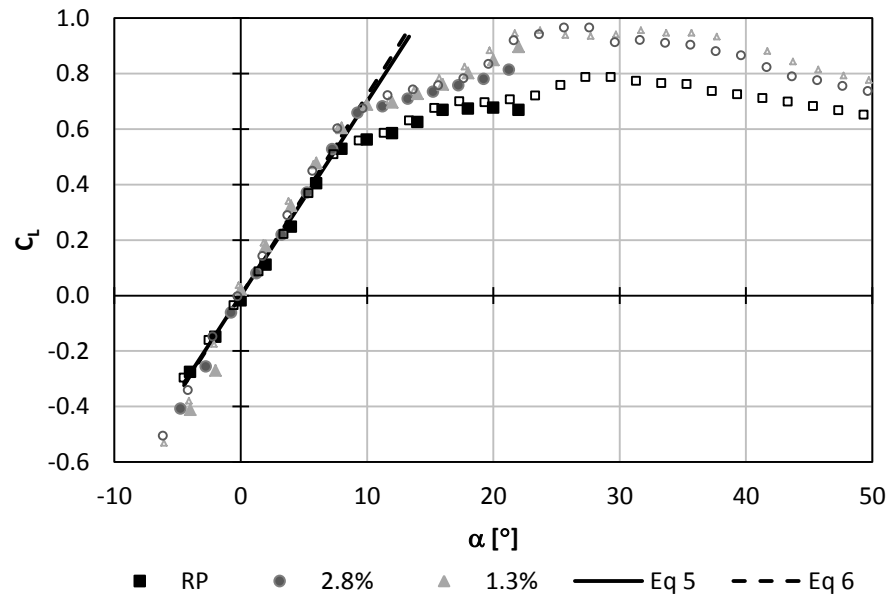

Figure 20. Lift coefficient trend for the rigid plate and two membrane wings: *Re* = 50,000; filled-symbol UA; open-symbols UF
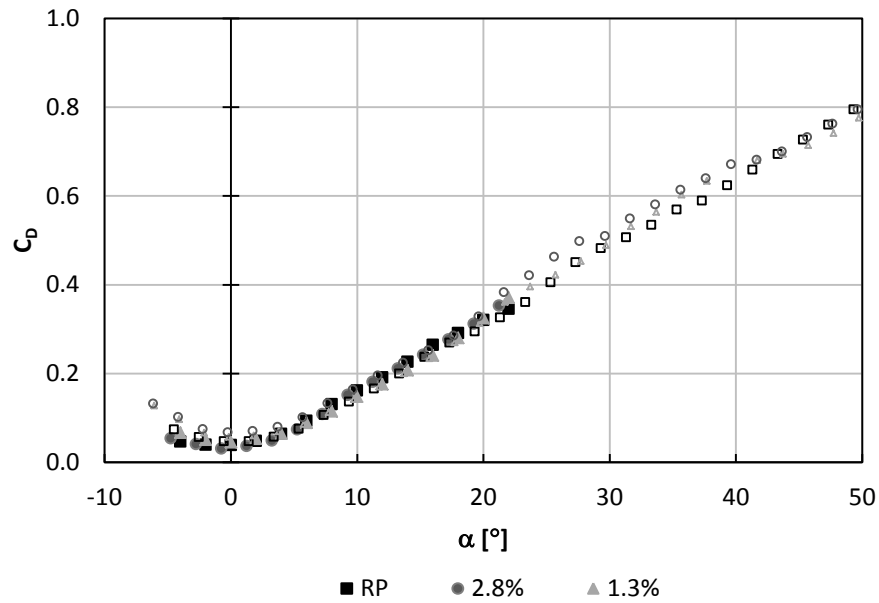

Figure 21. Drag coefficient trend for the rigid plate and two membrane wings: *Re* = 50,000; filled-symbol UA; open-symbols UF
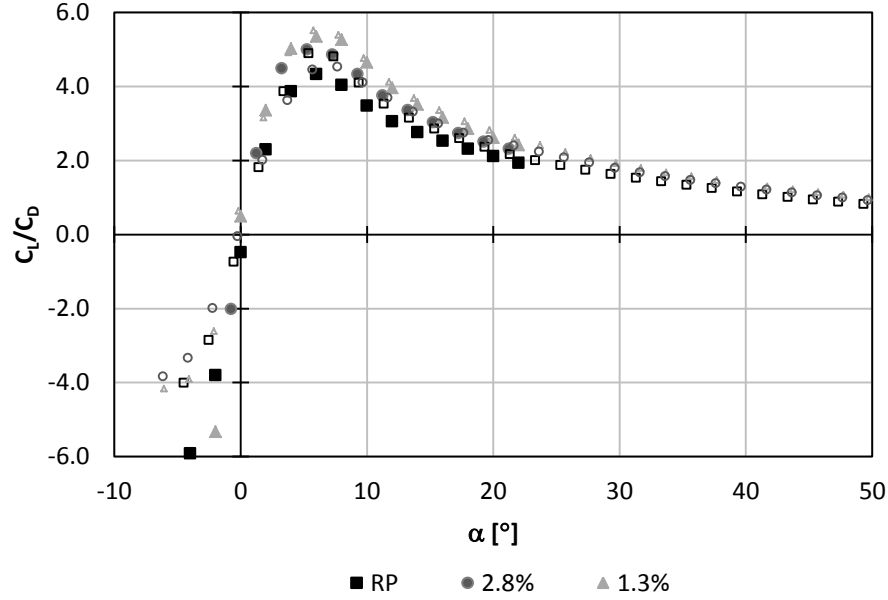
Figure 22. Lift-to-drag ratio trend for the rigid plate and two membrane wings: *Re* = 50,000; filled-symbol UA; open-symbols UF

The lift-curve slope for the membrane wings are also greater than the rigid plate: 0.084/° for the 1.3% pre-tension, 0.079/° for the 2.8% pre-tension and 0.067/° for the rigid plate. This was also shown in Hubner and Hicks (2011). Interestingly, despite the assumptions of lifting-line flow (high *Re,* inviscid, attached flow), the modified lifting-line equation by Helmbold for small *AR* as detailed in Anderson (2011) and shown in Eq. 5 is a reasonable assumption for a low *Re* rigid flat-plate with leading-edge separation: $C_{L,\alpha,Eq5} = 0.70$. For the calcuation, the two dimensional lift-curve slope was set to 2π/rad. The traditional lifting-line equation (Eq. 6) predicts a slightly higher lift-curve slope: $C_{L,\alpha,Eq6} = 0.72$, where the Glauert correction parameter τ is 0.12 for a rectangular wing of *AR* = 4.3. Eq. 6 better predicts the membrane wing lift curve slope for wings of *AR* = 1 to 4 which is typically higher than the rigid counterpart. Secondary effects due to low *Re* such as leading-edge separation are counteracted by increased membrane cambering, vibration and interaction with the leeside shear layer.

$$C_{L,\alpha} = \frac{c_{l,\alpha}}{\sqrt{1+\left(\frac{c_{l,\alpha}}{AR\cdot\pi}\right)^2}+\frac{c_{l,\alpha}}{AR\cdot\pi}} \tag{1}$$

$$C_{L,\alpha} = \frac{c_{l,\alpha}}{(1+\frac{c_{l,\alpha}}{AR\cdot\pi})(1+\tau)} \tag{2}$$

Drag results are presented in Figure 21. A typical nonlinear increasing drag coefficient is displayed at low alpha, indicating a quadratic dependence on lift. At higher angles, the drag dependency is relatively linear. The difference between the membrane and rigid plate data is not significant when considering the measurement uncertainty for the low drag measures. Drag measures between the two facilities compare well except for the rigid plate in which the ACF measures (open squares) are consistently lower than the MAV-WT measures (filled squares).

Aerodynamic efficiency measures are shown in Fig. 22. All three models exhibit a peak lift-to-drag ratio around 6–8°. This angle is just prior to the point where the lift curve slope decreases due to

the onset of stall conditions. Measures from the UA tunnel (filled symbols) show that the membrane wings increase the aerodynamic efficiency. The lowest pre-tension (1.3%) exhibits the highest L/D ratio at 5.4. This increased aerodynamic efficiency persists at high alpha where the relative uncertainty in the measures further decreases. The UF results also show the highest L/D ratio of 5.5 for the 1.3% pre-tension wing. The rigid plate produces lower aerodynamic efficiency until the angle-of-attack approaches 30°, where values become similar for all models, as the wing effectively is a blunt body and the drag is dominated by the overall wing geometry and not the membrane characteristics.

Effect of Aspect Ratio

To assess whether these benefits remained at for lower AR geometries, tests were performed on three models with a membrane cell AR of 1: 5-cell (AR = 4.3), 3 cell (AR = 2.6) and 1 cell (AR = 0.9). An additional 9-cell model was test with a membrane cell AR of 0.5. While it is expected that the lift curve slope decreases with aspect ratio, Fig. 23 shows that the lift curve slope continues to remain steeper for the membrane wing compared to the rigid wing. The steeper lift curve slope exists for both high and low Re (31,000 and 50,000). On average, the membrane increases the $C_{L\alpha}$ by approximately 15%. Figure 24 compares the lift curve slope values to the Helmbold modified lifting-line equation (Eq. 5-orange curve) and classical lifting-line theory (Eq. 6-blue curve). The two dimensional lift-curve slope was set to 2π/rad. The Glauert correction parameter (λ = 1) is 0.049, .082, 0.12, 0.13 for the four AR models tested: 0.9, 2.6, 4.0, and4.3, respectively. Again, the classical lifting-line equation compares more favorably than the low-AR corrected equation due to the increased lift generation by the membrane.

As Fig. 25 shows, the membrane wing produces higher lift in the stalled region, and it persists at lower AR. On average for the Re and AR range tested, the membrane increases the lift in the stalled region by more than 10%. Figure 26 summarizes the peak lift-to-drag ratio results. The peak efficiency occurs prior to the initial onset of stall where the lift curve slope begins the decrease and the drag, both form and induced, becomes more substantial (quadratic effect). Cleary, while aerodynamic efficiency decreases with AR, the membrane increases the aerodynamic efficiency, as expected, relative to the rigid plate, and this gain exists at lower AR as well (extrapolating the rigid plate trend). The net gain in aerodynamic efficiency is 12%, with a slightly higher gain associated with higher Re. Not shown in Fig. 26, but detectable in lift polars is that as AR decreases the angle at which the maximum lift-to-drag ratio occurs is increased—for both rigid and membrane wings. This is a result of both the shallowing of the lift curve and the broadening of the drag curve, both due to the dominance of the tip vortices and its effect on flow separation/reattachment.
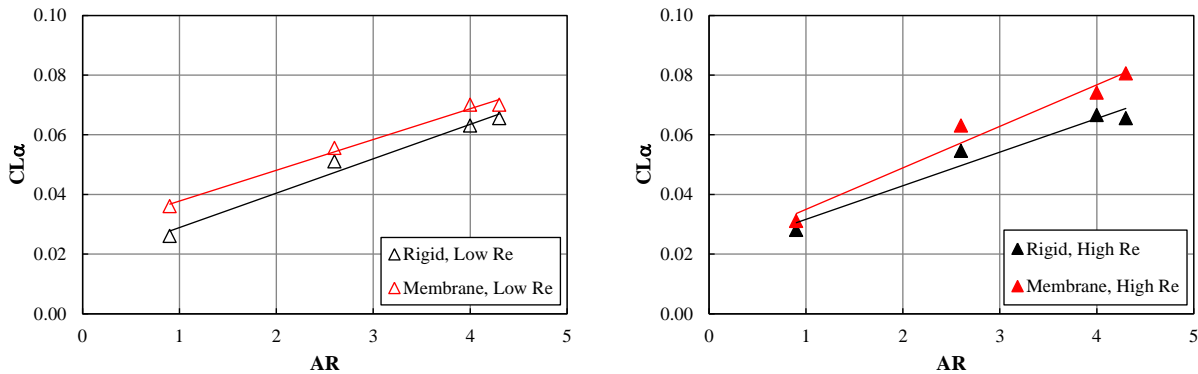

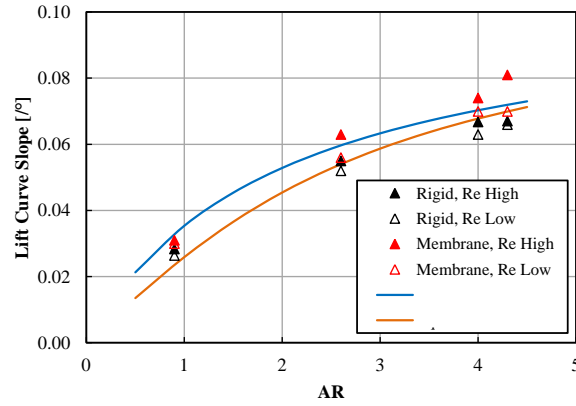**Figure 23.** The effect *AR* on the lift curve slope: *Re* = 31,000 and 50,000

Figure 24. Comparison of *AR* effect on lift curve slope: classical lifting-line theory (blue) and modified lifting-line theory for small *AR* wings (orange)
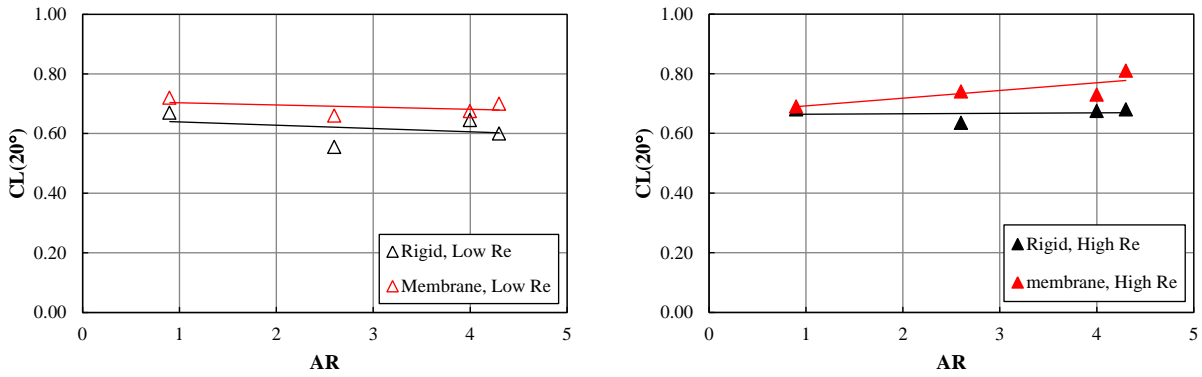

Figure 25. The effect *AR* on lift in the stall region
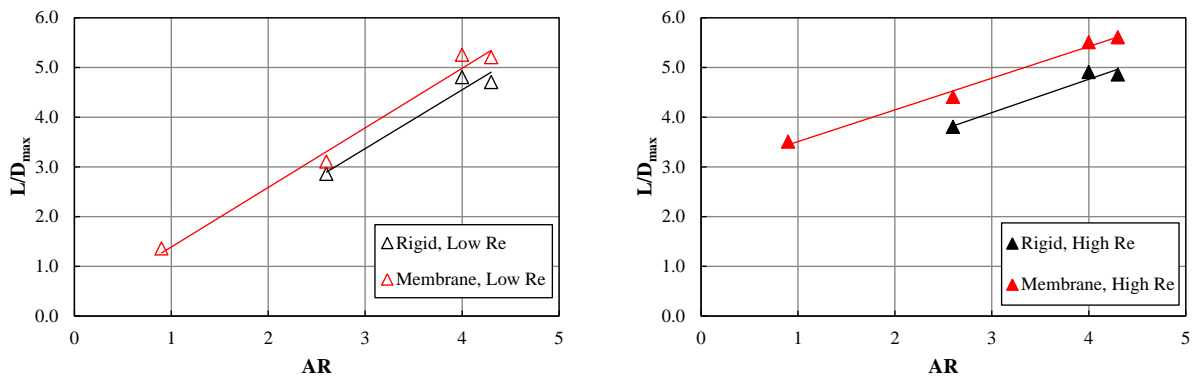

Figure 26. The effect *AR* on aerodynamic efficiency

<u>Dynamic vs Static Camber</u>

The results presented in this section compare the time-averaged and dynamic effect of the membrane for low *AR* wings (*AR* = 2) of varying pre-tension and cell *AR*. Of particular interest is the

objective of determining whether previously measured aerodynamic benefits of low-*AR* membrane wings with free trailing edges derive from time-averaged effects or dynamic fluid-structure interactions. Three *AR* = 2 planform designs with one, two and three membrane cells, as shown in Fig. 27, were tested. Each planform was pre-strained to three different pre-strain levels: 1%, 2%, and 4%. Thus, nine membrane models were tested. Figure 28 shows the corresponding Π_2 value based on the average spanwise pre-strain of the cells (Fig. 29), the cell span and the dynamic pressure. The trailing-edge of the membrane was free (unattached) and scalloped. A tenth, flat, rigid plate model was used as a control. The pre-tension effect on the lift, drag, pitching moment, aerodynamic efficiency, and time-averaged membrane shape were quantified and are presented for *Re* = 50,000. For a few geometry/pre-strain combinations that showed the largest deviations in lift and aerodynamic efficiency, rigid models of the time-averaged deformation were printed using fused deposition modeling (FDM, a type of 3D printing) and tested at the same α and dynamic pressure conditions. Flow field and membrane deformation results are discussed Arce *et al*. (2013) in the next section.
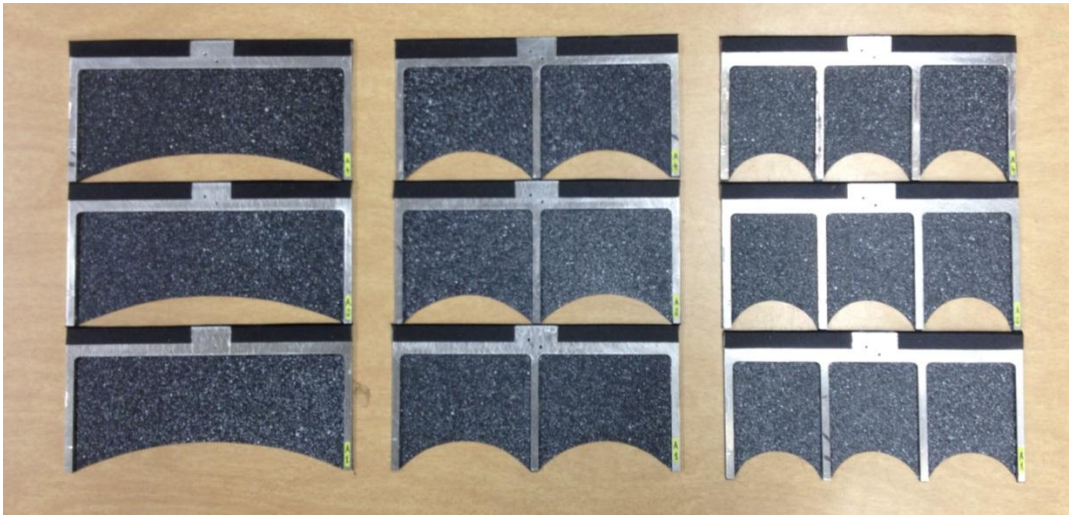

Figure 27. Membrane wing models: one, two and three cells (left to right) with pre-strain of 1%, 2% and 4% (bottom to top)
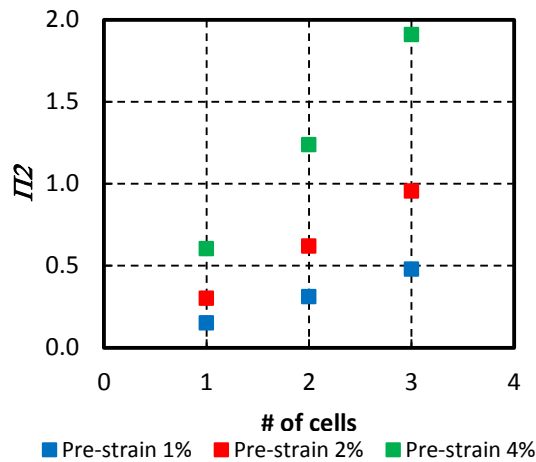

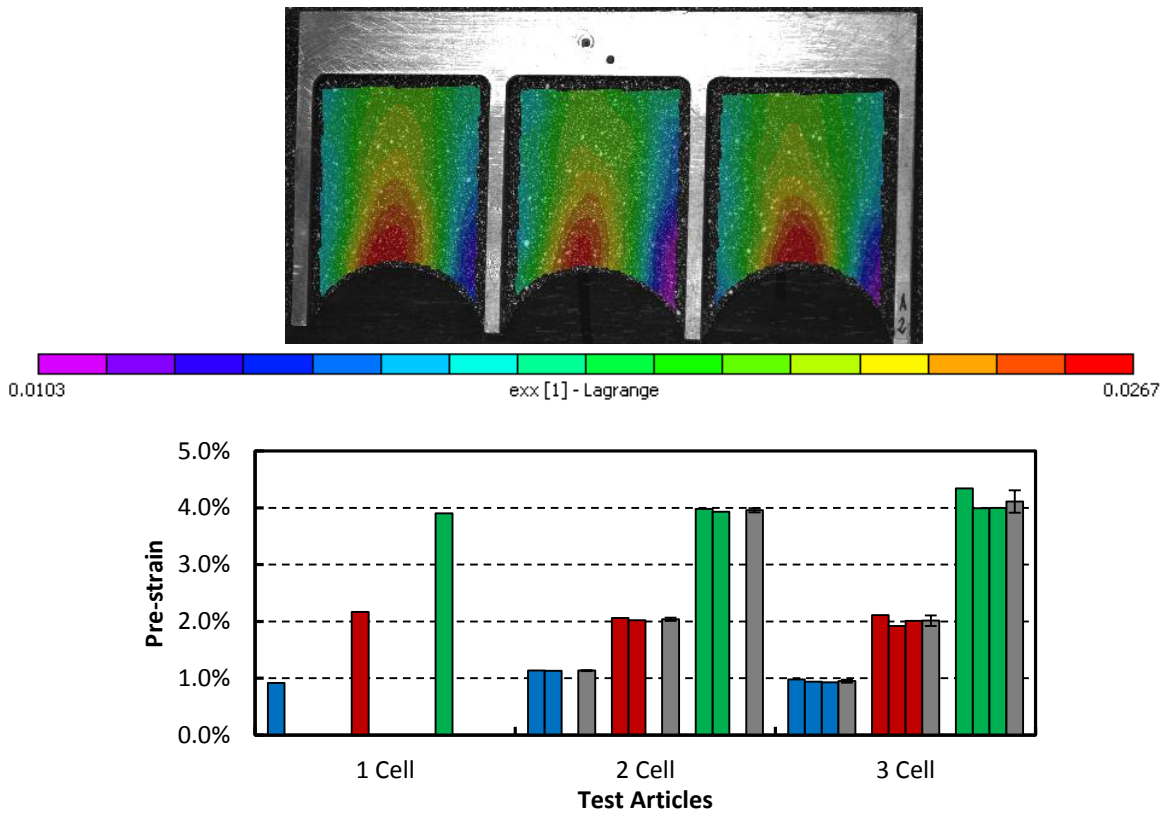**Figure 28.** Π_2 range of the membrane wings

34

Figure 29. Spanwise strain distributions for the three-cell, 2%-strain membrane wing (top) and the individual cell average pre-strain for all the test articles (bottom: blue = 1%; red = 2%; green = 4% and grey = average pre-strain for the model)

The rapid prototyping technique used to fabricate the rigid wings is a layered build approach which uses acrylonitrile butadiene styrene (ABS) thermoplastic. The process can reach a layer resolution of 0.25 mm. The time-resolved deformation of the membrane wings were captured with a DIC system at 6° and 18°. These angle-of-attack locations correspond to the peak aerodynamic efficiency and nominal peak lift coefficient for the two- and three-cell membrane wings. The following steps describe the procedure on how the time-averaged deformation wings were fabricated. First, the time-resolved deformations were averaged to obtain a mean deformation shape. Next, outlier DIC measures and data near the edges of the frame were removed, and the data sets were smoothed. Ideally, the flow over the membrane wing would generate a symmetric deformation; thus, based on this assumption, the spatial deformation field was averaged symmetrically about the central chord to further decrease noise. Then, high-order polynomial curve fits in the chordwise direction at incremental spanwise steps across the cell were then generated to create splines to import into *SolidWorks* and create a Standard Tessellation Language (STL) file compatible with the rapid prototyping software. Finally, the wings were printed using the Dimension 1200es rapid prototyping machine. The time-averaged deformation test models are shown in Fig. 30.
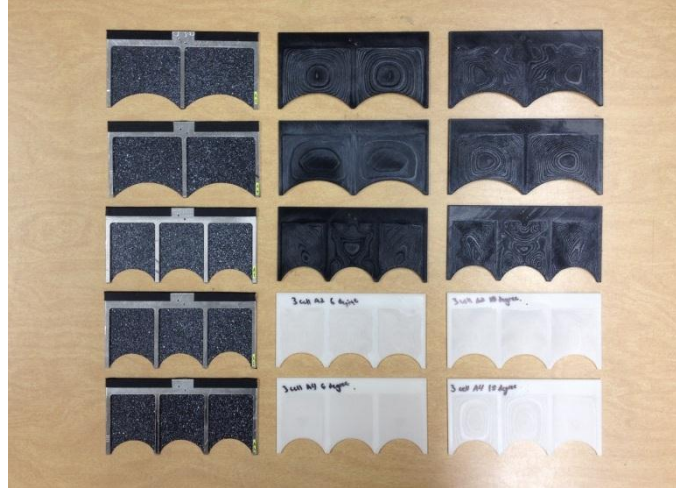
Figure 30. Membrane wings (left) and corresponding 6˚ (middle) and 18˚ (right) time-averaged shape deformation wings (from top to bottom: two-cell 1%, two-cell 4%, three-cell 1%, three-cell 2%, three-cell 4%)

Figure 31 shows C_L trends relative to each frame configuration: 1, 2, or 3 cells. Interesting trends are immediately apparent. For the one-cell frame (b'/c' = 2.37), all the lift curves, despite the level of pre-tension, show a positive zero-lift α. The lift curve slope is nominally the same as the rigid plate; however, the stall region is postponed to higher angles and the maximum lift coefficient is obtained by the one-cell (b'/c' = 2.37), 4% (Π_2 = 0.6) model. The positive zero-lift α indicates an effective time-averaged negative geometric twist or camber of the model. The two-cell frame (b'/c' = 1.16) does not exhibit the pronounced positive zero-lift α, passing through the (0,0) point, but does have a higher lift-curve slope and improved stall region characteristics (greater lift and stall α) compared to the rigid plate and consistent with past membrane wing studies. The three-cell frame (b'/c' = 0.76) is similar to the two-cell frame except the benefits in the stall region are less pronounced as the membrane experiences less deformation and acts more like the rigid plate. Figure 32 compares the lift-curve slope for each of the frames. For the two- and three-cell frame cases, the lowest pre-tension (1%, Π_2 = 0.3 and 0.5) shows the largest lift-curve slope, demonstrating the importance of membrane flexibility to produce effective cambering. However, the one-cell frame performs no better than the rigid plate, indicating a limit to the desired flexibility low-α.
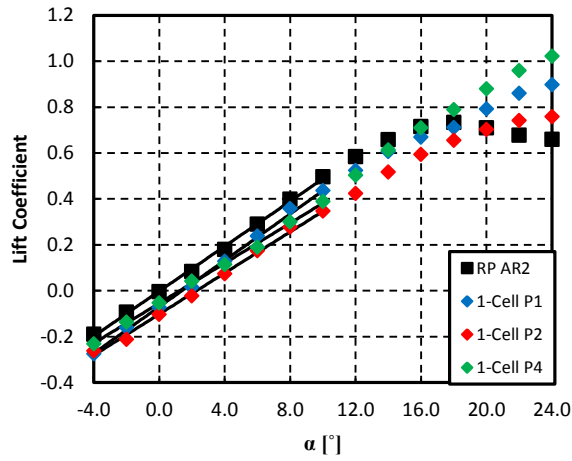
A) One-cell membrane wing
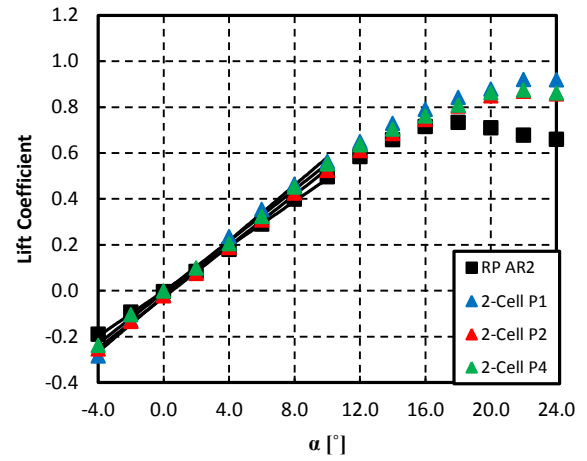
B) Two-cell membrane wing
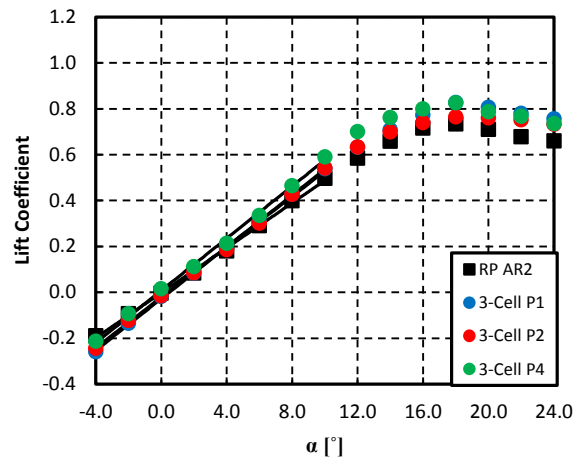
C) Three-cell membrane wing

Figure 31. Lift coefficients of membrane wings (square = rigid plate; diamond = one-cell; triangle = two-cell; circle = Three-cell; blue = 1%; red = 2%; green = 4%)
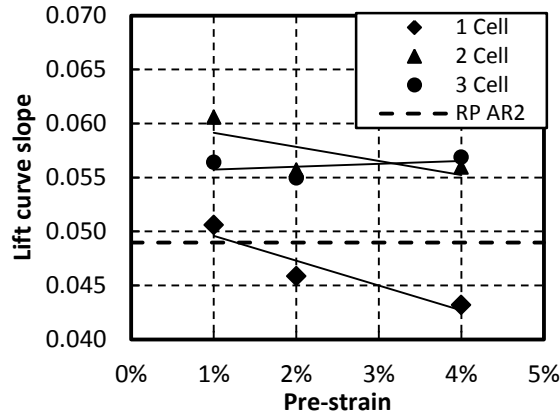
Figure 32. Lift curve slope vs membrane pre-strain

Figure 33 plots the drag coefficient data for each frame. The 1% and 2% one-cell membrane wings show a relatively angle independent C_D (0.25 to 0.30). While the 4% one-cell frame starts to show a general increasing trend with angle-of-attack, it is still a significantly high value of drag. These high drag coefficients are caused by substantial deformation of the vibrating membrane at the trailing edge, despite scalloping. For b'/c' approaching 2 and $\Pi < 0.5$, the wing acts like a lifting blunt body due to the large vibration amplitude. Decreasing the cell aspect ratio near or below 1 substantially decreases the vibration amplitude and increases vibration frequency, creating a more conventional drag curve. In general, membrane drag is nominally higher than the rigid plate drag but is within the range of measurement uncertainty at most angles-of-attack.

Figure 34 compares the effect of cell size on $C_{M,c/4}$. Due to the high drag component of the one-cell frame, the magnitude of the moment at higher α is not as large and the slope with respect to α is not as steep when compared to the rigid plate. Decreasing the membrane cell span and increasing the membrane tension steepens the slope ($C_{M,\alpha}$), but the slope of the membrane wing is still less than the slope of the rigid plate. At low α, the two- and three-cell frames show a slightly negative pitching moment. For a conventional airfoil, this would indicate an effective positive cambering of the wing; however, the lift curves do not indicate positive camber at $\alpha = 0°$. The likely source is the shifting of the drag distribution towards the trailing-edge, due to the larger trailing-edge vibration amplitude. This would induce a nose-down moment tendency about the quarter chord. In the stall region, the trends for the two- and three-cell frames diverge. Near stall, the two-cell frame pitching moment magnitude is larger than that of the rigid plate and three-cell frame.
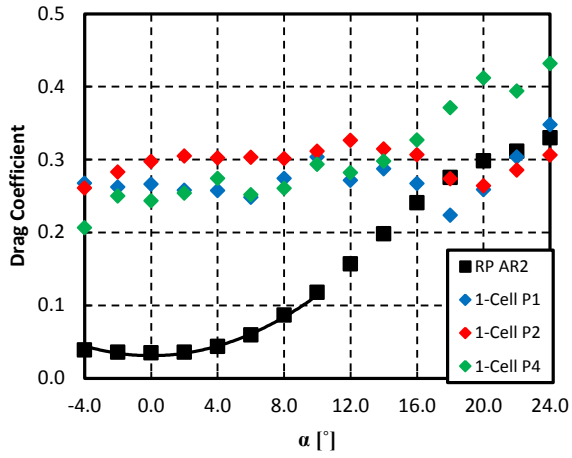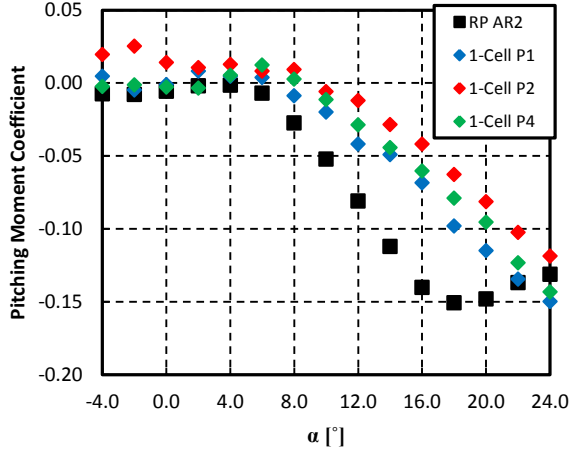
A) One-cell membrane wing
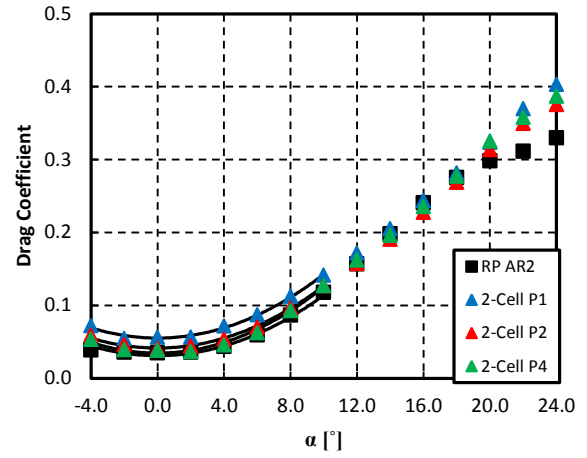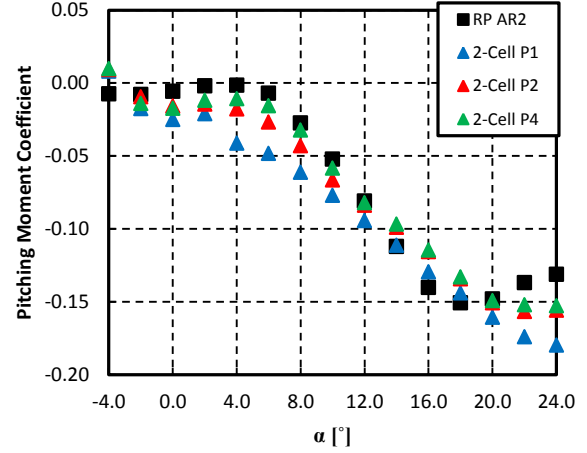
B) Two-cell membrane wing
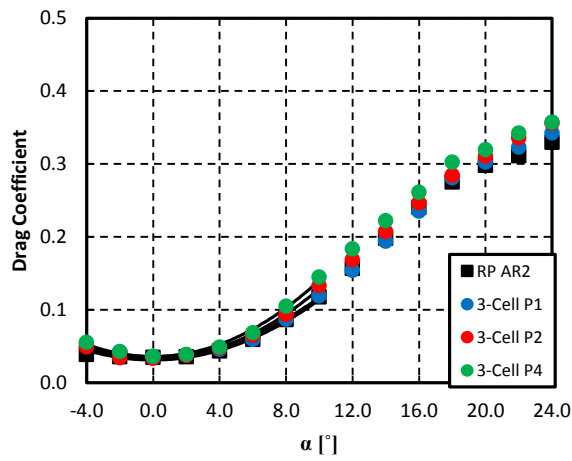
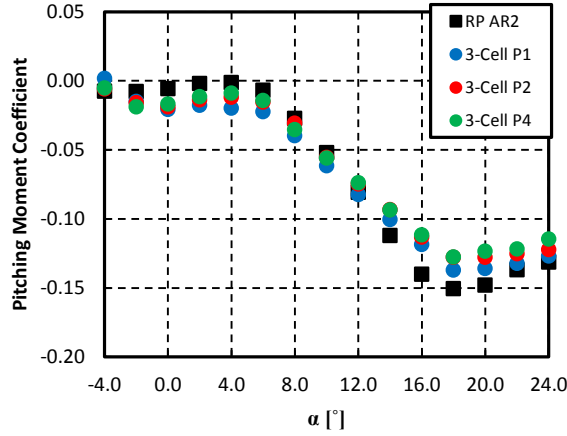**C)** Three-cell membrane wing

Figure 33. Drag coefficients of membrane wings (same legend at Fig. 31)
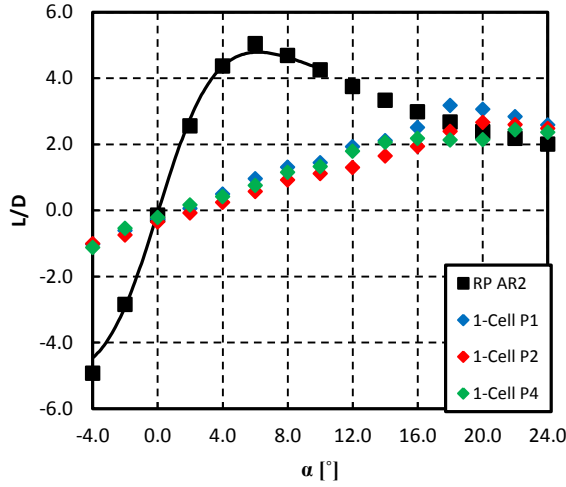
A) One-cell membrane wing
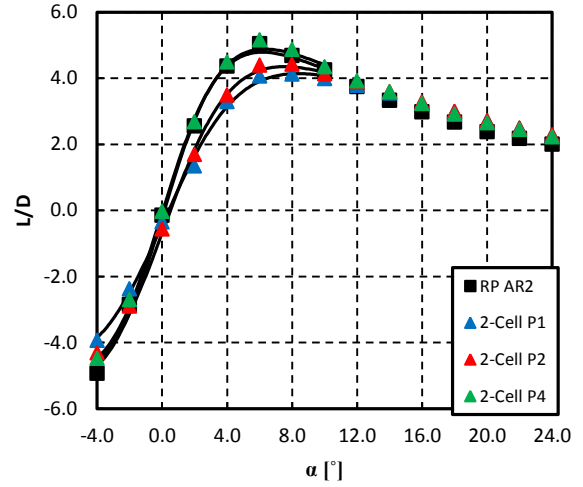

B) Two-cell membrane wing

C) Three-cell membrane wing

Figure 34. Pitching moment at quarter chord of membrane wings (same legend at Fig. 31)

Due to the high C_D value of the one-cell frame, the L/D_{max} is much less than the multi-cell frames and rigid plate (Fig. 35) for low or moderate angles-of-attack. The efficiency increases relatively linearly, following the linear lift trend, peaks near stall (~18-20°), and exceeds its counterparts in the stall region, as shown in Fig.35A. The aerodynamic efficiency for the two- and three-cell models match closely to the rigid plate and within the range of the measurement uncertainty. At higher α, where measurement uncertainty decreases as drag increases, both the two- and three-cell wings show marginally higher aerodynamic efficiency—a benefit arising due to the increased lift of the membrane wings. The α of L/D_{max} is the function of both pre-strain and cell AR. Increasing the pre-strain (except for the one-cell frame) or decreasing the cell span decreases the α in which maximum efficiency occurs. For the two- and three-cell wings, the peak efficiency occurs before the onset of stalling conditions, 6° to 8°, approaching the rigid plate angle of 5°

A) One-cell membrane wing

B) Two-cell membrane wing
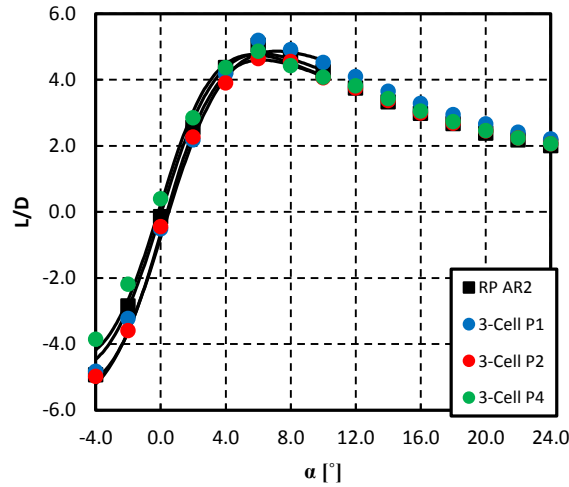
C) 3-cell membrane wing

Figure 35. Lift over drag ratio of membrane wings (same legend at Fig. 31)

Comparing the aerodynamic measures to properties of the wing, some general guidelines appear for the low *AR* models. Figures 36 and 37 plot lift slope, minimum drag and peak efficiency parameters relative to the aeroelastic parameter, Π_2, and the cell aspect ratio, b'/c'. Nominally, for values of $\Pi_2 < 0.5$ and $b'/c' > 2$, the membrane is effectively too loose. Drag values can be high and lift and efficiency values can be lower. This corresponds to large vibration amplitudes of the membrane, which exceeded 50% relative to the chord for the one-cell wing. Amplitudes for the two- and three-cell wings were approximately 20% and 10%, respectively. Pre-tensioning further lowered the vibration amplitude but not to the extent that cell aspect ratio did. An exception to this preferential trend towards lower cell aspect ratio was maximum lift coefficient for the one-cell wing. Despite a cell *AR*

greater than 2, the 4% pre-strain (Π_2 = 0.6) showed considerable lift augmentation at high α. At the other end of the spectrum, towards rigidity, there is also an expected upper limit on the aeroelastic parameter and a lower limit on cell aspect ratio in terms of diminished returns with flexibility. Benefits in maximum lift and aerodynamic efficiency waned for the three-cell model (b'/c' = 0.75) compared to the two-cell model at higher α. The cell AR played a more important role in this trend than the aeroelastic parameter.
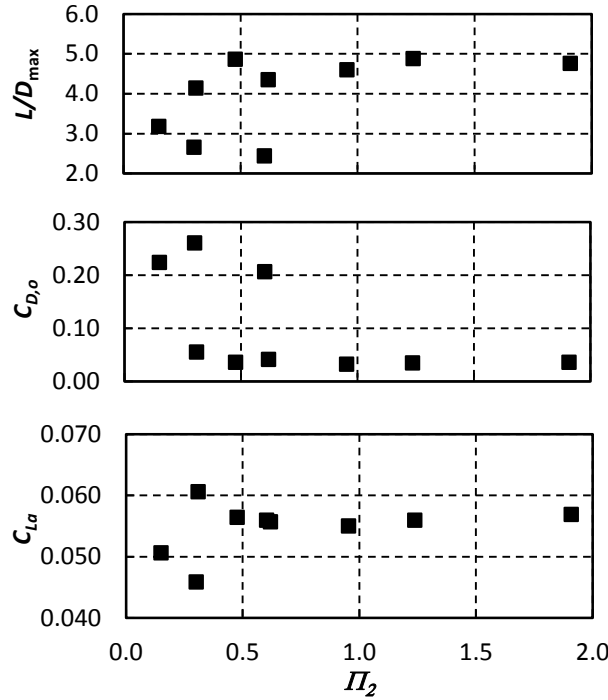

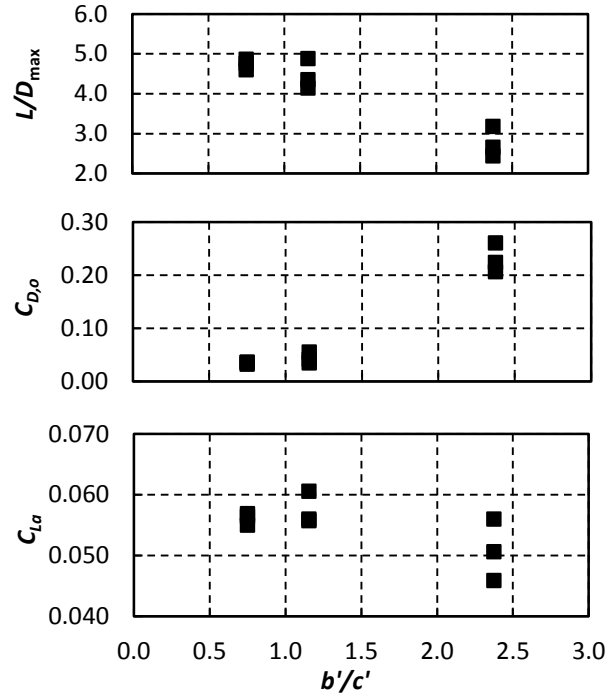**Figure 36.** L/D_{max} , $C_{D,o}$ and $C_{L,\alpha}$ vs Π_2

Figure 37. L/D_{max} , $C_{D,o}$ and $C_{L,\alpha}$ vs b'/c'

Based on the fact that the one-cell frames had such poor drag characteristics, only the time-averaged shapes of the 1% and 4% two-cell wings and all three of the three-cell wings were fabricated at α of 6° and 18°. Rigid models were printed and tested at the same dynamic pressure as the membrane wings. Force measurements were acquired as previously described. Figure 38 shows the time-averaged out-of-plane displacement field for the 1% and 4% two-cell frame. As expected, increased angle-of-attack (aerodynamic loading) and decreased pre-tension caused larger membrane deformation. Only the left cell is shown because, as previously discussed, centerline symmetry was a forced condition (to minimize random and systematic error) in developing the deformation file to print. For three of the four cases shown, a typical billowing pattern develops due to the aerodynamic loading; however, for the low angle, low pre-strain case, time-averaged waviness appears in the deformation pattern. This waviness also appears for the three-cell frame for low pre-strain values. Because the camera frame rate is approximately one-tenth the membrane fundamental frequency, undesired phase-averaging could exist due to unintended synchronization between the membrane fluctuation and the camera frame rate. This, though, was not expected to be significant due to the wandering nature of the membrane fundamental frequency and the fact that the camera frame rate is an average rate, slightly varying in period from image to image.

A) two-cell, 1%

B) two-cell, 4%

$\alpha = 6˚$ $\alpha = 18˚$
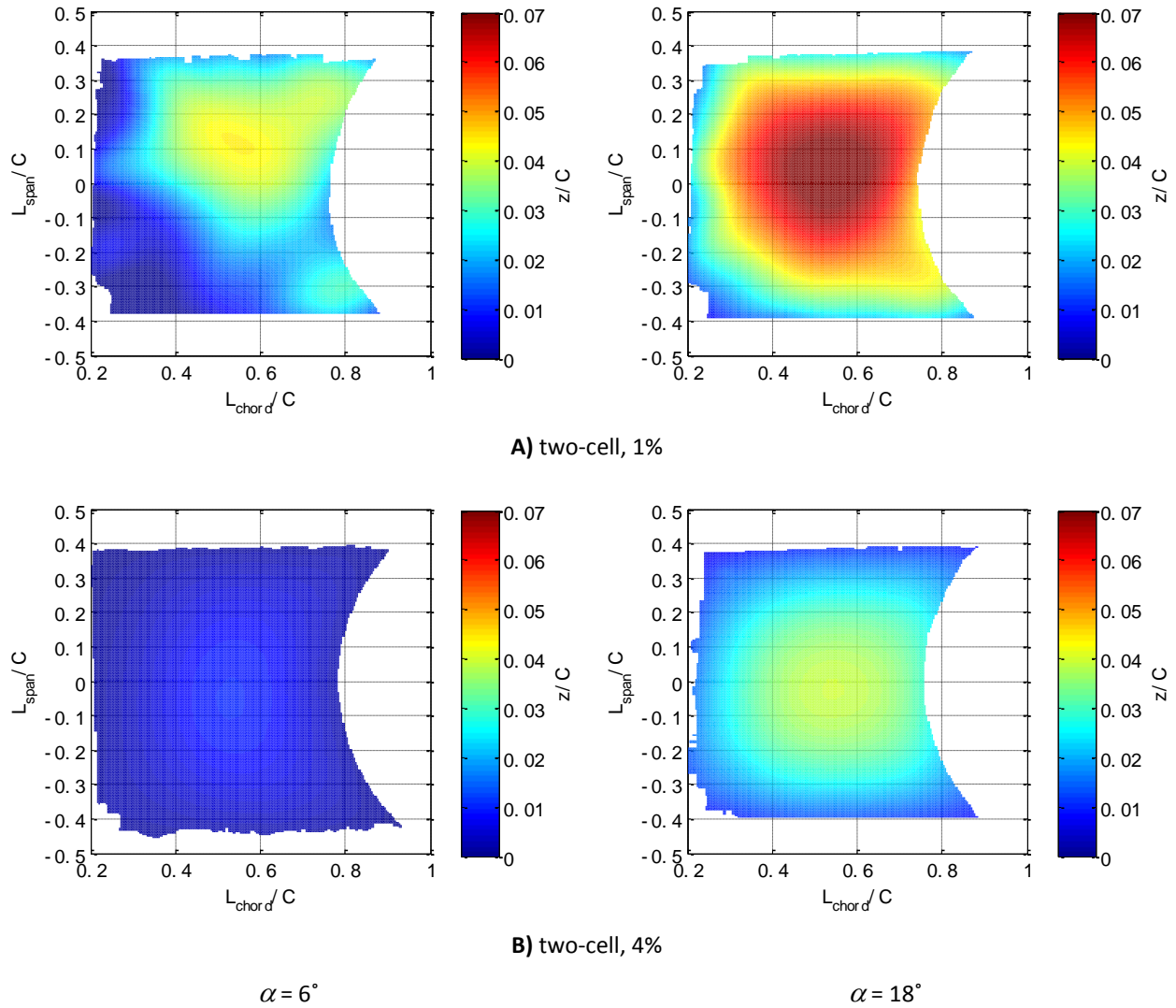
Figure 38. Time-averaged deformation field of one side of the two-cell membrane wing

A computerized mesh for the rigid model was created from these time-averaged deformations. Based on local chordwise slices of the grid, the local geometric twist and camber changes across the span of the membrane was calculated. Figure 39 is a schematic, which also includes the rigid leading-edge of the frames, defining the geometric twist angle, α', and membrane camber. An average twist angle and camber were calculated for each wing. These results are presented in Figs.40 and 41. Solid symbols represent $\alpha = 6˚$ and open symbols represent $\alpha = 18˚$. The average geometric twist, Fig.40, is negative in all cases. Membrane pre-tensioning, as expected, decreases the average geometric twist and camber of the membrane wing. Aerodynamic loading (increased α, open symbols) increases the twist magnitude. In static terms, this should decrease the lift curve slope relative to a flat plate, but as shown in Fig.31, the membrane wing has a higher lift curve slope. From Fig. 41, a modest increase in the

average camber with α exists for all cases. This would correspond to an increase in lift curve slope, thus, an opposing and potentially larger effect than the negative geometric twist in the context of the lift curve results shown in Fig.31 (more discussion to follow).
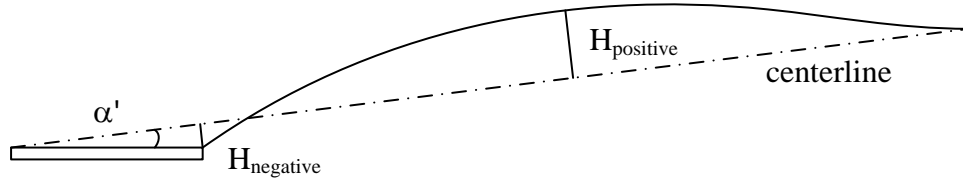

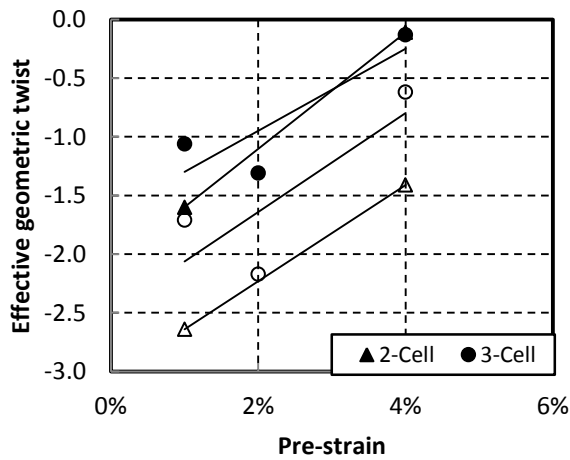**Figure 39.** Schematic of effective geometric twist and average camber

Figure 40. Effective geometric twist of time-averaged deformation wings (solid symbol = 6˚; open symbol = 18˚)
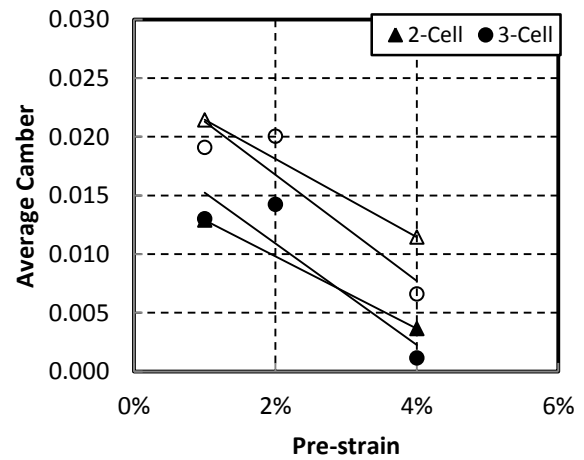
Figure 41. Average camber of time-averaged deformation wing

To assess the differences between the printed models (time-averaged shape) and the membrane models, C_L, C_D and L/D measures were recorded at 6˚ and 18˚. As shown in Fig. 42, compared to membrane wings (blue bars), the printed wings (green bars) produces less lift at the same geometric angle-of-attack. This trend exists for all ten cases (5 models, 2 α's). On average, the membrane lift coefficient is 16% larger compared to the printed wing. Thus, the increase in lift does appear to be directly related to the membrane vibration as supported by PIV measures on the membrane wing (Timpe *et al.*, 2013; Arce *et al.*, 2013). In general, the vibration of the membrane and interaction with the shear layer reduces the time-average size of the separated region compared to the rigid plate. This appears to have greater effect on lift than drag as indicated by the drag results (to discuss shortly). Interestingly, the printed wings on average have less lift than the flat rigid plate by 5%. This is an indication that time-averaged negative geometric twist of the printed wings outweighs the positive camber. These are opposing contributors to lift generation. If the negative twist is the stronger of the two, then this would cause a slight shift left of the lift curve, accounting for the moderately lower lift generated by the printed wings compared to the flat baseline wing.

44

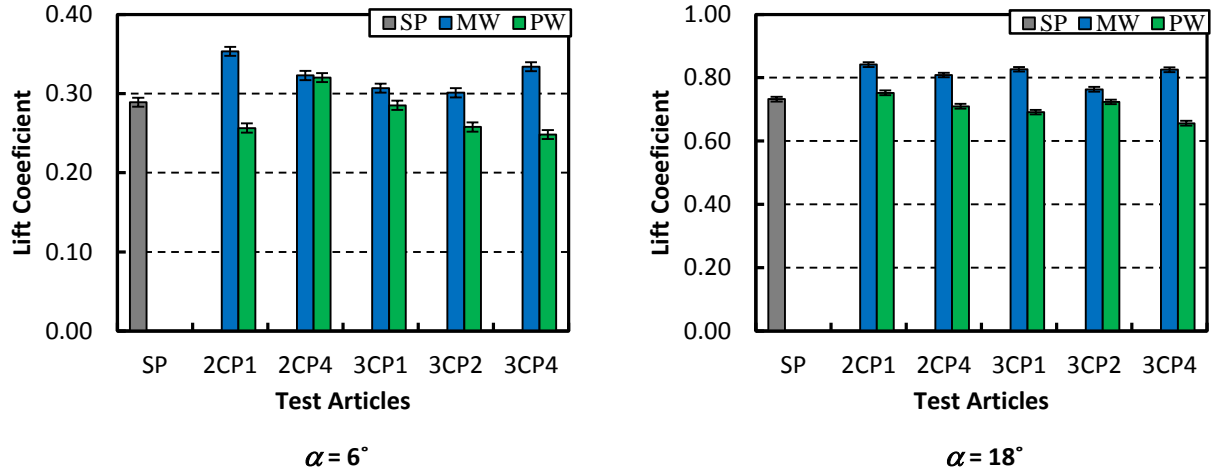$\alpha = 6°$ $\alpha = 18°$

Figure 42. Comparison of lift among rigid plate (SP), membrane wing (MW) and printed wing (PW)

Figure 43 presents the comparison of C_D at both low and high α. At low α, there is no significant difference, relative to the indicated measurement uncertainty, in the drag measures of the membrane and printed wings except for the two-cell, 1% pre-strain model. For this specific case, the membrane wing shows a considerable drag penalty due to the over-flexibility of the membrane caused by the moderate cell AR (b'/c' = 1.27) and low pre-strain (1%). In the stall region (high-α), where there is lower relative drag measurement uncertainty due to the higher drag measurements, the membrane wings produce higher drag for all five cases with an average increase of 12%. In fact, the printed "streamline" wings produce less drag than the flat plate. Thus, while the dynamic effect of the membrane is important for additional lift creation, it also appears to be a source of increased drag, primarily at higher α. The net effect on efficiency is that the lift augmentation of the membrane wings outweighs the drag penalty for nine of the ten test cases, particularly at the lower α were efficiency is highest (Fig. 44). The average increase in L/D was 13% at the peak efficiency α and 3% near stall conditions. Compared to the flat plate, the average aerodynamic efficiency for the printed wings was lower at 6˚ but higher at 18˚.
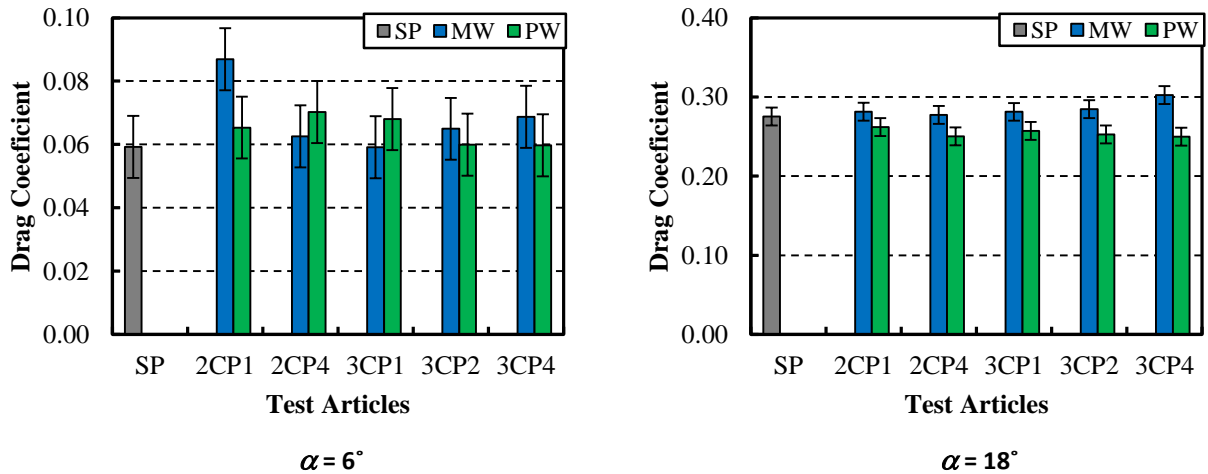

$\alpha = 6°$ $\alpha = 18°$

Figure 43. Comparison of drag among SP, MW and PW
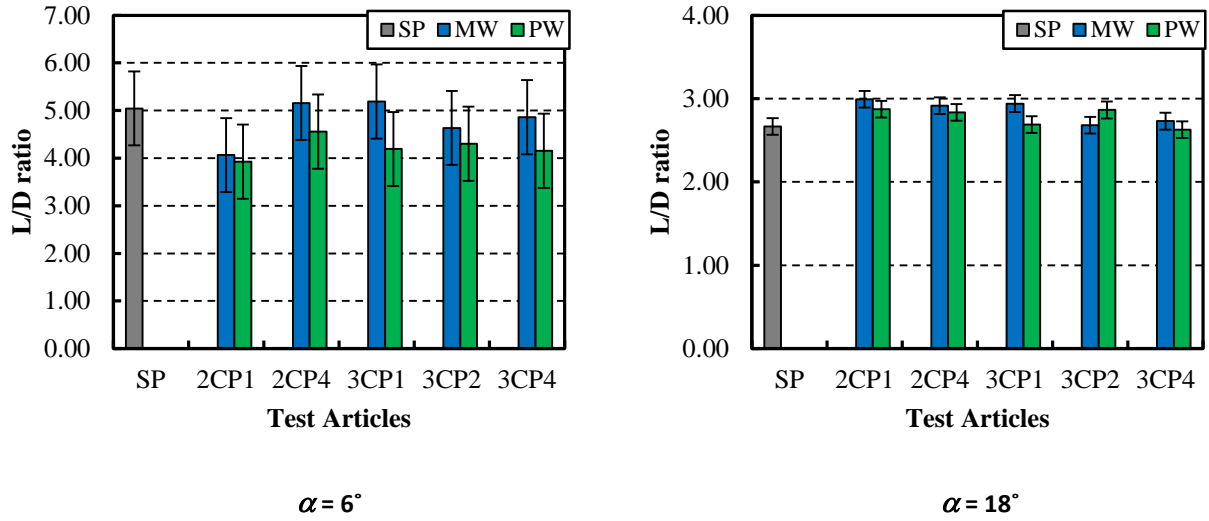
$\alpha = 6°$ $\alpha = 18°$

Figure 44. Comparison of *L/D* among SP, MW and PW

Fluid-structure Interaction (Timpe, *et al.*, 2013; Arce *et al.*, 2013)

Velocity Field Measurements

In this portion of the results, the mean, RMS and Reynolds shear stress quantities from PIV measurements are presented for a 5 cell membrane wing (*AR* = 4.3; aerodynamic coefficients shown in Figs. 20 – 22) over the mid-span of the wing. The *u*-components are associated with the *x* (free stream) direction and *v*-components with the *y* (free stream normal) direction. Following the Reynolds decomposition, $u = \bar{u} + u'$, with u representing an instantaneous velocity, $\bar{u} = u_{\text{mean}}$, and $\sqrt{\langle u'^2 \rangle} = u_{\text{rms}}$; a similar breakdown is applied to *v*. These quantities are computed by time-averaging over all available vectors. Therefore, flow properties are presented including effects of all membrane positions, while the region where the membrane vibrated is masked. In the plots presented in this section several features of the membrane are included for reference. An approximate cycle of instantaneous membrane displacements, extracted from the DIC measurements, are included in the PIV plane as thin black lines to give an idea of the volume and nature of vibrations. The details of the membrane motion statistics will be discussed in the next sub-section. The time-averaged membrane positions are provided as red lines. For membrane wings, the solid leading portion is outlined as a solid black line while the out-of-plane battens are outlined as gray dashed lines.

Figure and 46 present normalized *u*-component, mean contours ($\bar{u}/U_\infty$) and velocity slices at low-α (4, 8°) comparing the baseline rigid plate (RP) and membrane wings (ε = 1.3%, 2.8%; Π_2 = 0.4, 0.9, respectively). At α = 4° the flow around the leading-edge (LE) is similar between all models, while the wake of the RP is characterized by a larger velocity reduction yet narrower wake width than that of the membrane wings (at center span plane). Evidence of a small separation bubble is present close to the leading edge of all three models. At 8° the separation bubble has grown to cover most of the length of the RP in this plane, indicated by the reversed velocity (dark blue region) above the model surface. The membrane wings show a significant reduction in the size of this time-averaged separation region, which also creates a tighter curvature (smaller radius) of streamlines near the LE and higher acceleration in the flow. The normalized $\bar{u}$ profiles from Fig. 46 show the steeper velocity gradient of the membrane wing models at *x/c* = 0.2. This leads to an approximate 25% (1.5 mm) reduction in the shear layer height and

18% higher maximum velocities. The near wake is also broadening for the RP as angle-of-attack increases and the wake-deficit becomes as large as $0.5U_\infty$ of the freestream at $x/c = 1.4$ (while the deficit is merely ~$0.25U_\infty$ and $0.2U_\infty$ for the membrane wings, ε = 1.3% and 2.8%, respectively). These findings at low α coincide with when the membrane wings begin to show enhanced lift characteristics and higher maximum L/D, while still in the first linear $C_{L,\alpha}$ range for the RP (prior to signs of stall effects).

From the force data at $\alpha \approx 8°$, the RP linear $C_{L,\alpha}$ slope undergoes a change becoming less steep, beginning a second lift trend and broad stall region (delayed to higher angles-of-attack by the membrane wings). From Fig. 47 (high α, $\bar{u}/U_\infty$ contours) at α = 12°, the RP shows that on the centerline of the wing the separation bubble has eclipsed the length of the model, extending into the wake. In comparison, the membrane wings show time-averaged attached flow, greatly reducing the amount of separated flow over the wing and showing no reversed flow extending into the wake. This trend continues at higher angles-of-attack with the separated, reversed flow of the baseline RP extending as far as x/c = 1.6 and 2.1 into the wake at α = 16° and 24°, respectively; and a major reduction of reversed flow by the membrane wings. Notably at 24°, there is evidence of the membrane wings greatly influencing the v-component of the flow as indicated by time-averaged streamlines. The wakes of the membrane wings at 24° are also angled down from the free stream direction (downwash), which coincides with the α-range when maximum C_L values were obtained (25% higher than baseline) from force data (Fig. 20). Inspecting the high-α shear layer and wake profiles ($\bar{u}$) at x/c = 0.3, 1.4 (Fig. 48), the trend of higher accelerated velocities and thinner shear layer are particularly apparent at 12°, when the rigid plate is just past the force-predicted angle-of-attack where it is fully separated over the mid-span of the model. Note: flow visualization shows that reattachment exists further outboard at this angle due to the tip vortices. The 2.8% pre-tension wing shows a slightly narrower wake than the 1.3%, while both portray reduced peak wake-deficit velocities.
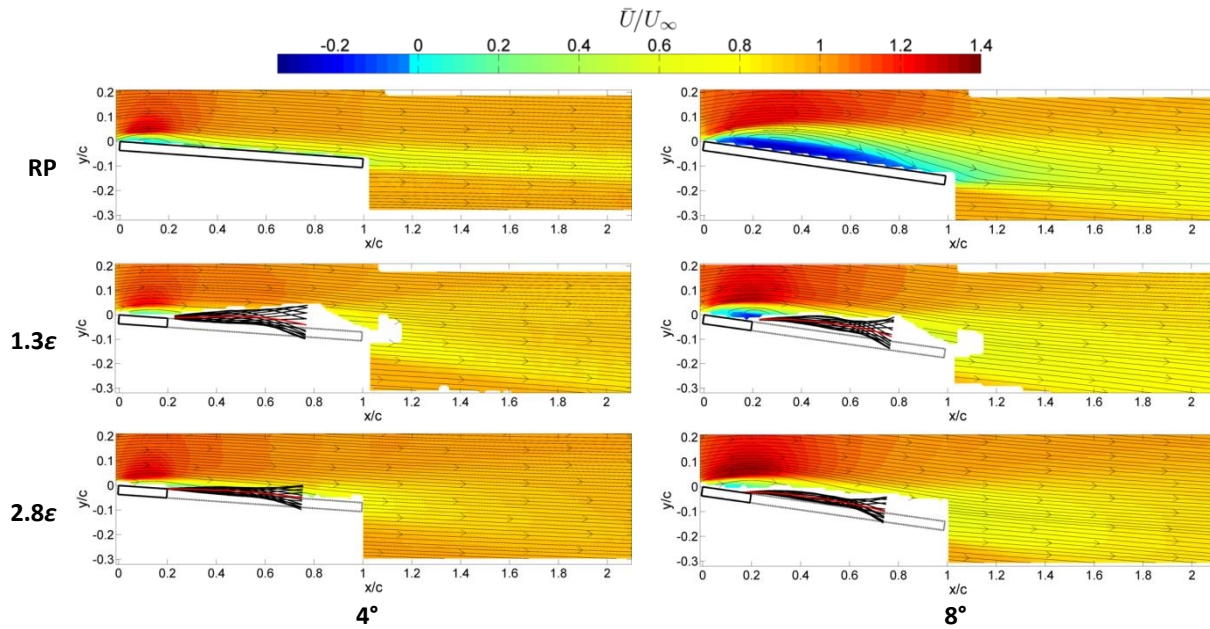
Figure 45. $\bar{u}/U_\infty$ contours on the centerline plane comparing RP and membrane wings at low α: 4° and 8°

47
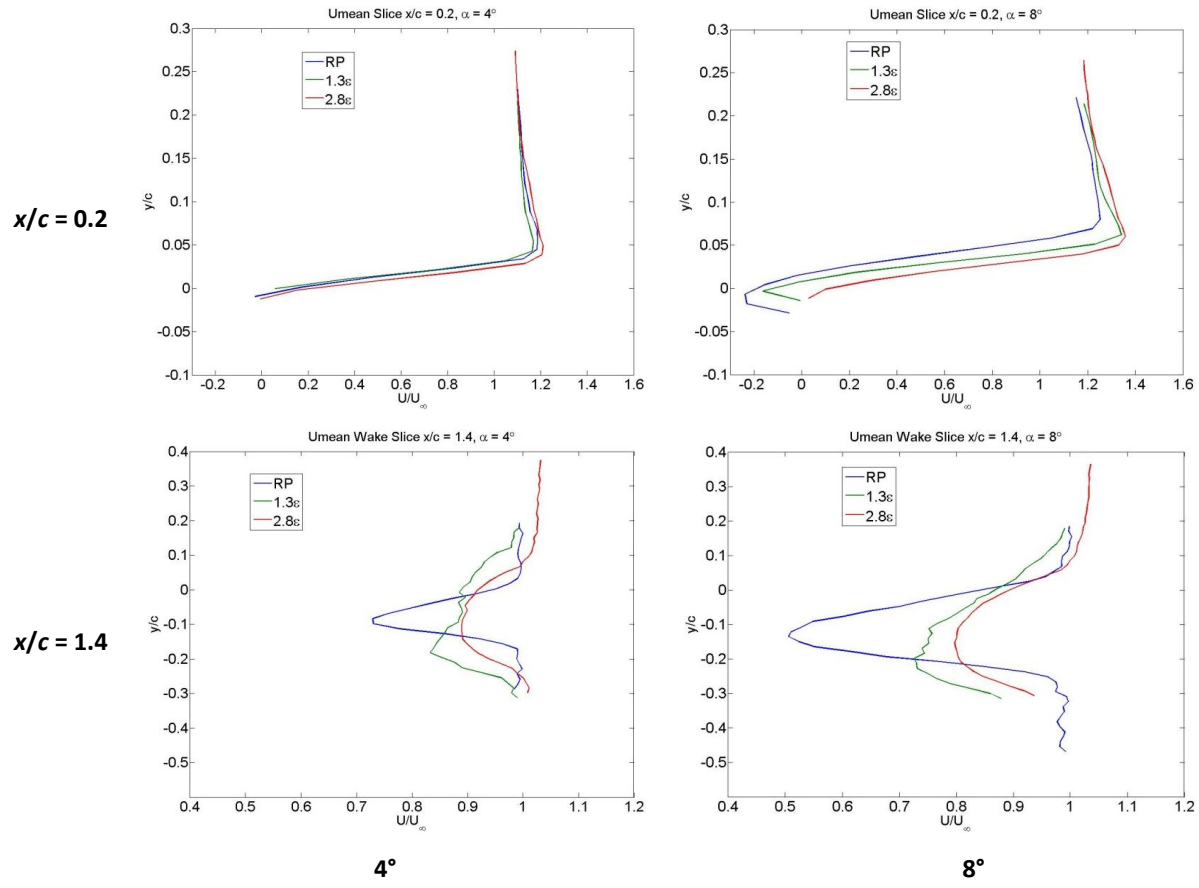
Figure 46. $\overline{u}/U_\infty$ profiles on the wings centerline plane at x/c = 0.2 near LE, and x/c = 1.4 near-wake, comparing RP and membrane wings at low α: 4° and 8°

Figure 47. $\bar{u}/U_\infty$ contours on the wings centerline plane comparing RP and membrane wings at high α: 12°, 16° and 24°
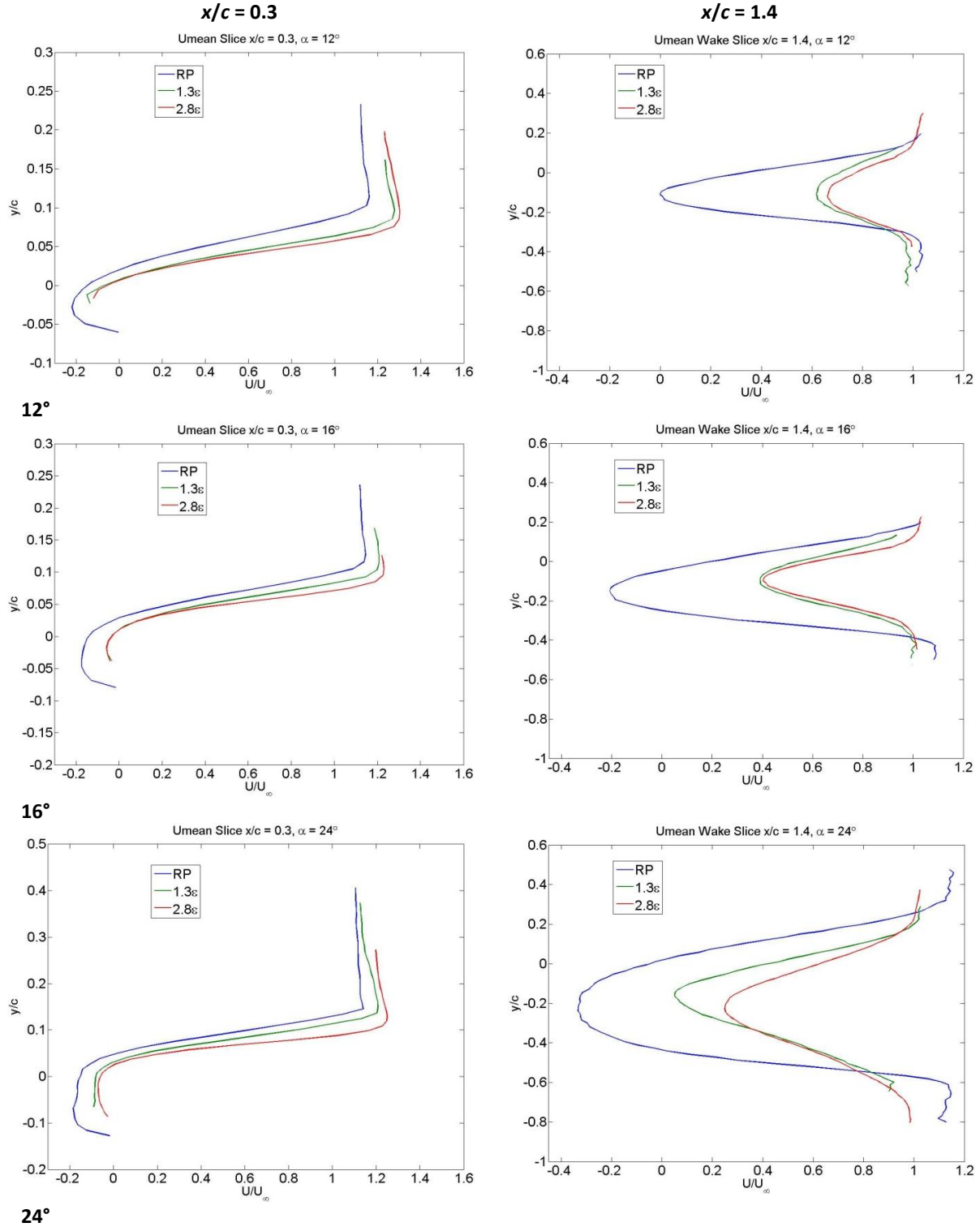
Figure 48. $\bar{u}/U_\infty$ profiles on the wings centerline plane at *x/c* = 0.3, near membrane LE; and *x/c* = 1.4, near-wake; comparing RP and membrane wings at high α: 12°, 16° and 24°

From the u_rms and v_rms flow characteristics at α = 8° and 12° (Figs. 49 and 50) one can see how the membranes motions alter the shear layer emanating from the leading edge of the wing. At α = 8° the membrane extends above the wing into the region where the shear layer from the baseline RP exists disrupting the flow, in the measurement plane, as was evident from the mean flow streamlines presented previously. The behavior at α =12° is similar where the membrane extends upward altering the shear layer, but, due to its increased height away from the wings surface, the membrane does not completely disrupt the shear layer at this location. The membrane wings have enhanced u_rms peak levels towards the trailing-edge of the membrane caused by its motions into the flows which are highlighted in the α = 12° (Fig. 49) case. The motion of the membrane wing also influences the fluctuating velocity field emanating from below the model as well. This can be evidenced by the origin of the trailing edge shear layer, in this plane, moving closer the trailing edge of the membrane and having increased peak values of both u_rms and v_rms.

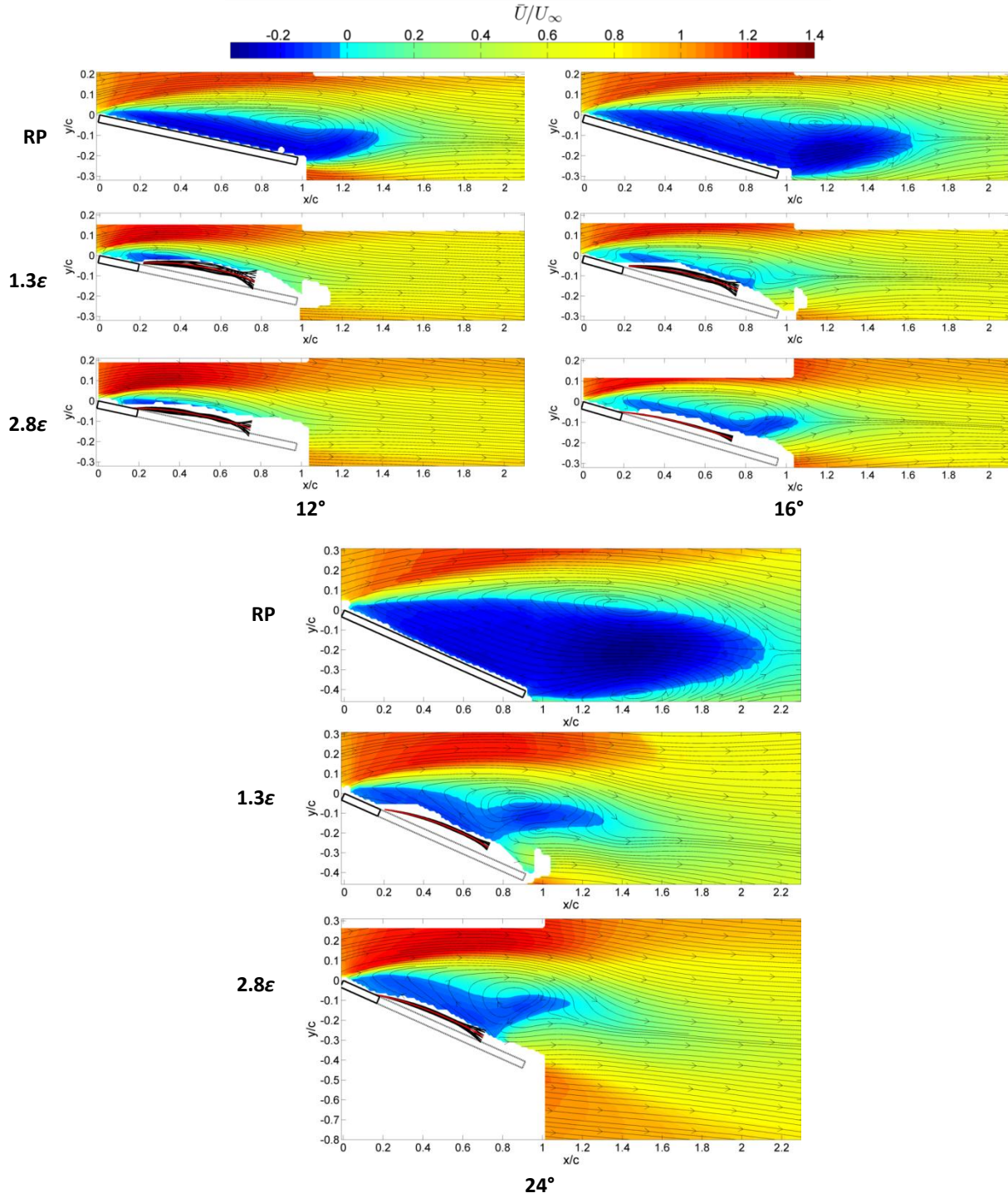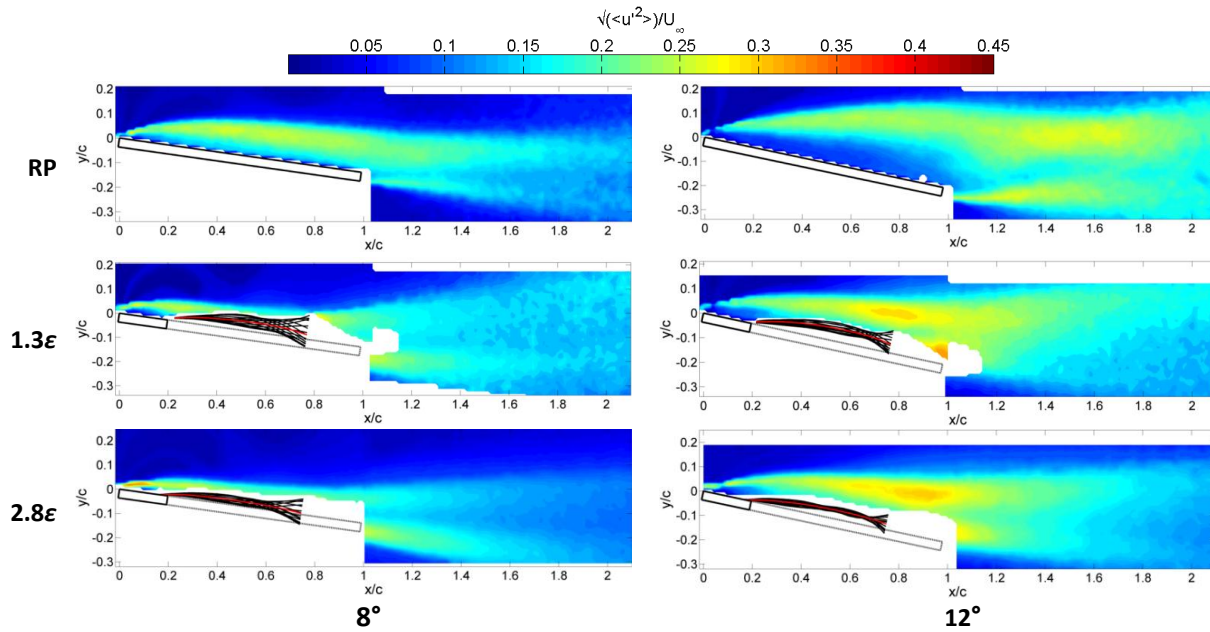**Figure 49.** $\boldsymbol{u_{rms}/U_\infty}$ contours on the wings centerline plane comparing RP and membrane wings at lower α: 8° and 12°
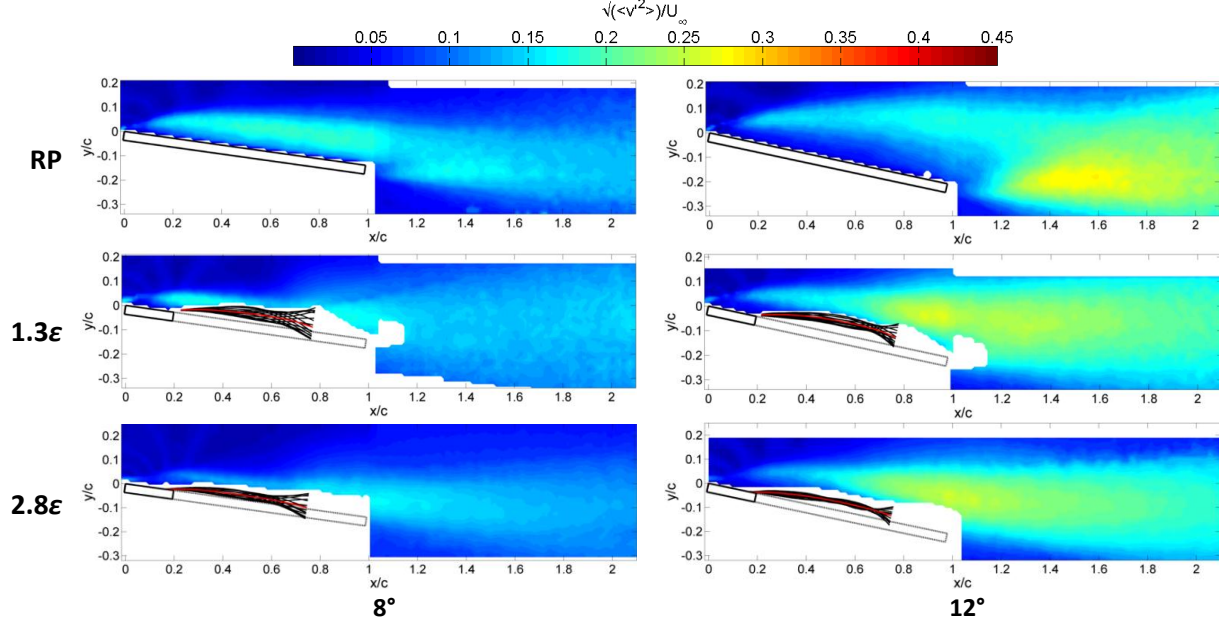
Figure 50. v_{rms}/U_∞ contours on the wings centerline plane comparing RP and membrane wings at lower α: 8° and 12°

At higher angles-of-attack the u_{rms} and v_{rms} behaviors plotted in Figs. 51 and 52, respectively, show significant changes to the fluctuating velocity fields caused by the membrane wings. The baseline continues to show a shear layer emanating from the leading edge rising further away from the wings surface with increasing angle-of-attack as well as evidence of the shear layer emanating from the trailing edge due to the limitations of the measurement extent. This behavior is accompanied with increasing levels of the turbulence. The membrane wings show an enhanced influence on the flow turbulence indicated by the larger and bi-regional u_{rms} values created near the membrane TE. This phenomenon is present at 16° and grows larger and more intense at 24°, with velocity fluctuations as large as $0.5U_\infty$ Fig. 51. The v_{rms} of the membrane wings differs in that there is no sign of intensifying disproportionately when α = 16°, followed by a much larger size and more intense peak region developed at 24° (Fig. 52). The u_{rms} trends well the C_D (Fig. 21), growing steadily with α, while the v_{rms} associates well with the C_L (Fig. 20), where there is one trend for the 10–20° α-range and a second trend of higher values in 20–30° α-range where maximum lift is obtained. The v_{rms} values showed magnitude increase to $0.5U_\infty$ and $0.54U_\infty$, for ε = 1.3% and 2.8%, respectfully, at 24°. The u_{rms} and v_{rms} values show some dependence on pre-tension, with the 2.8% wing generally having a slightly greater impact on flow fluctuations than the 1.3% wing at higher angles-of-attack.

From the velocity fluctuations the normalized Reynolds Shear Stress (*RSS*) is computed and plotted as contour plots for a range of α in Fig. 53. The *RSS* retains the negative sign, i.e., $RSS = \frac{-\overline{u'v'}}{U_\infty^2}$. Therefore, same sign fluctuations (u', v') generate negative regions and opposite sign fluctuations generate positive regions. At α = 8°, there is similar turbulent momentum transport for the membrane wings and the RP, while at α = 12°, 16° and 24°; the RP shows a symmetric (top to bottom) pattern of *RSS* development (in the wake) associated with the shearing and turbulent mixing. The membrane wings, however, show unique patterns of generally enhanced fluctuating momentum transport, also being pulled closer to the membrane's trailing edge.

52
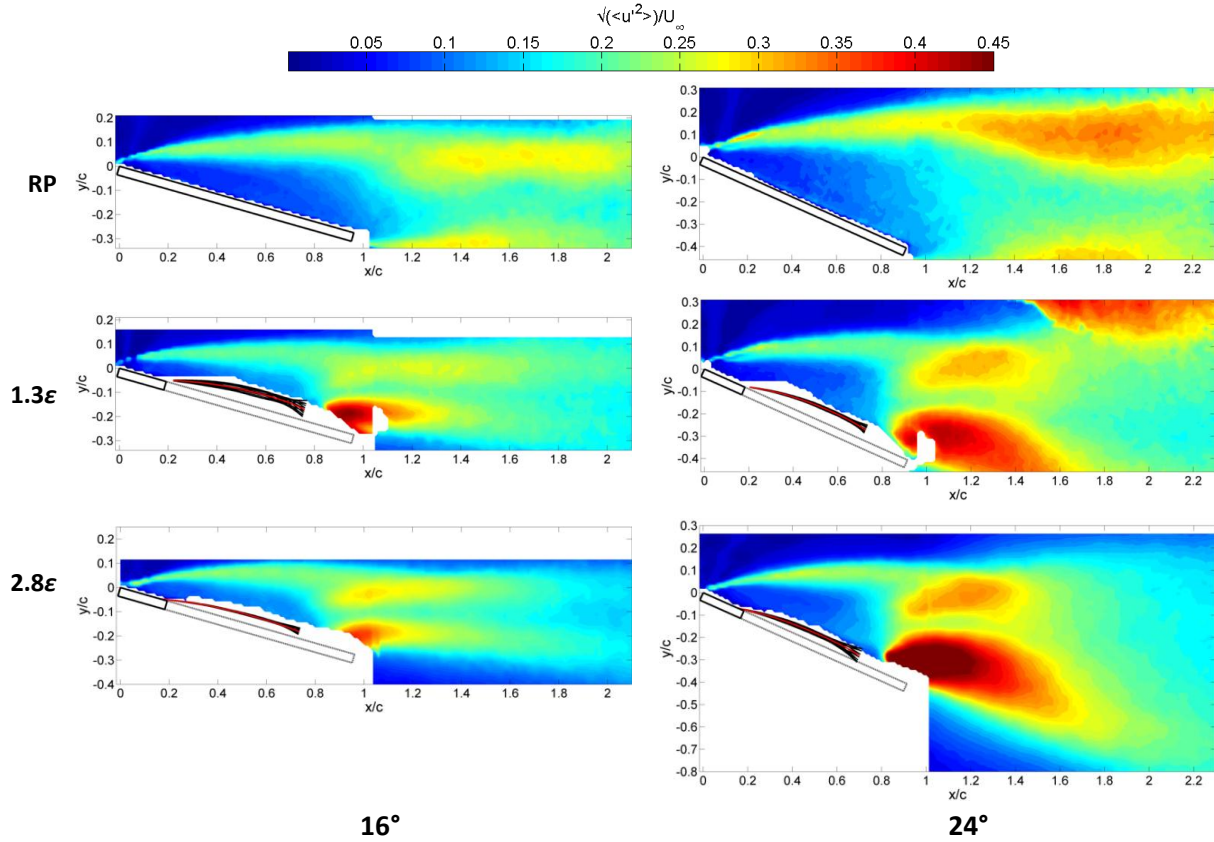
Figure 51. u_{rms}/U_∞ contours on the wings centerline plane comparing RP and membrane wings at high α: 16° and 24°

Specifically at 12°, there is enhanced positive *RSS* created overtop the membrane TE and in the wake (Fig. 53B) as the flow is forced due to the membranes vibrations to fluctuate opposing ($-u'$, $+v'$ when the membrane is up and $+u'$, $-v'$ when down). Alternating u' and v' components are driven by the membrane presence through viscous interaction (a no penetration condition). The membrane's motions force the increased fluctuating velocity components as indicated by the increased values of the *RSS* further upstream compared to the rigid plate counterpart which is representative of an increased turbulent momentum transport in the region immediately downstream of the membrane. This helps explain the difference in the mean velocity fields for this angle-of-attack (Fig. 47) where the recirculation region in the wake of rigid flat plate is not present for the membrane wings. At 16° the *RSS* for the membrane wings and RP appear similar with a nearly symmetric top to bottom wake pattern; however, the membrane wings exhibit the formation of this wake behavior closer to the TE (Fig. 53C).
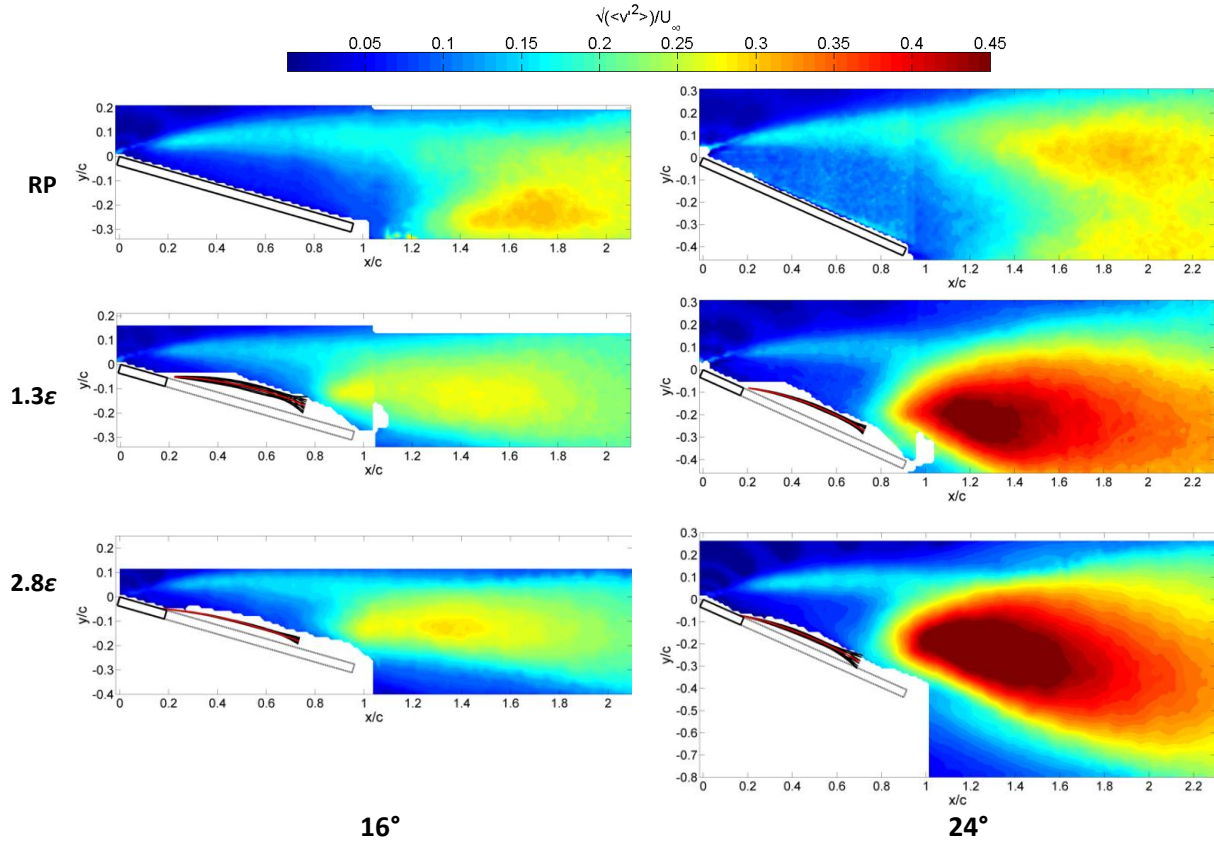
Figure 52. v_{rms}/U_∞ contours on the wings centerline plane comparing RP and membrane wings at higher α: 16° and 24°

Finally, at α = 24° there is unique patterning for the membrane wings, with alternating signs of *RSS* values close the TE caused by vortical structures formed in this region (Fig. 54), and a large oblong region of high magnitude (~ -0.12, or double the peak of the baseline or other α cases) negative *RSS* developed in the near wake (Fig. 53D). This region of large amplitude *RSS* of the flow is dominated by higher speed air that emanates from under the membrane and is pushed upward ($+u'$, $+v'$) as the membrane TE distends upward, followed by a $-u'$, $-v'$ as the TE passes down. Due to unsymmetrical (top/bottom) u-component momentum, a large amplitude burst of high streamwise momentum flow is not created and it ends up as a $-u'$ from the mean in the case where the membrane is down. As with u_{rms} and v_{rms}, the 2.8% pre-tension wing shows greater magnitudes than the 1.3% wing, possibly an effect of vibration frequency or amplitude (characteristics detailed in the following section).

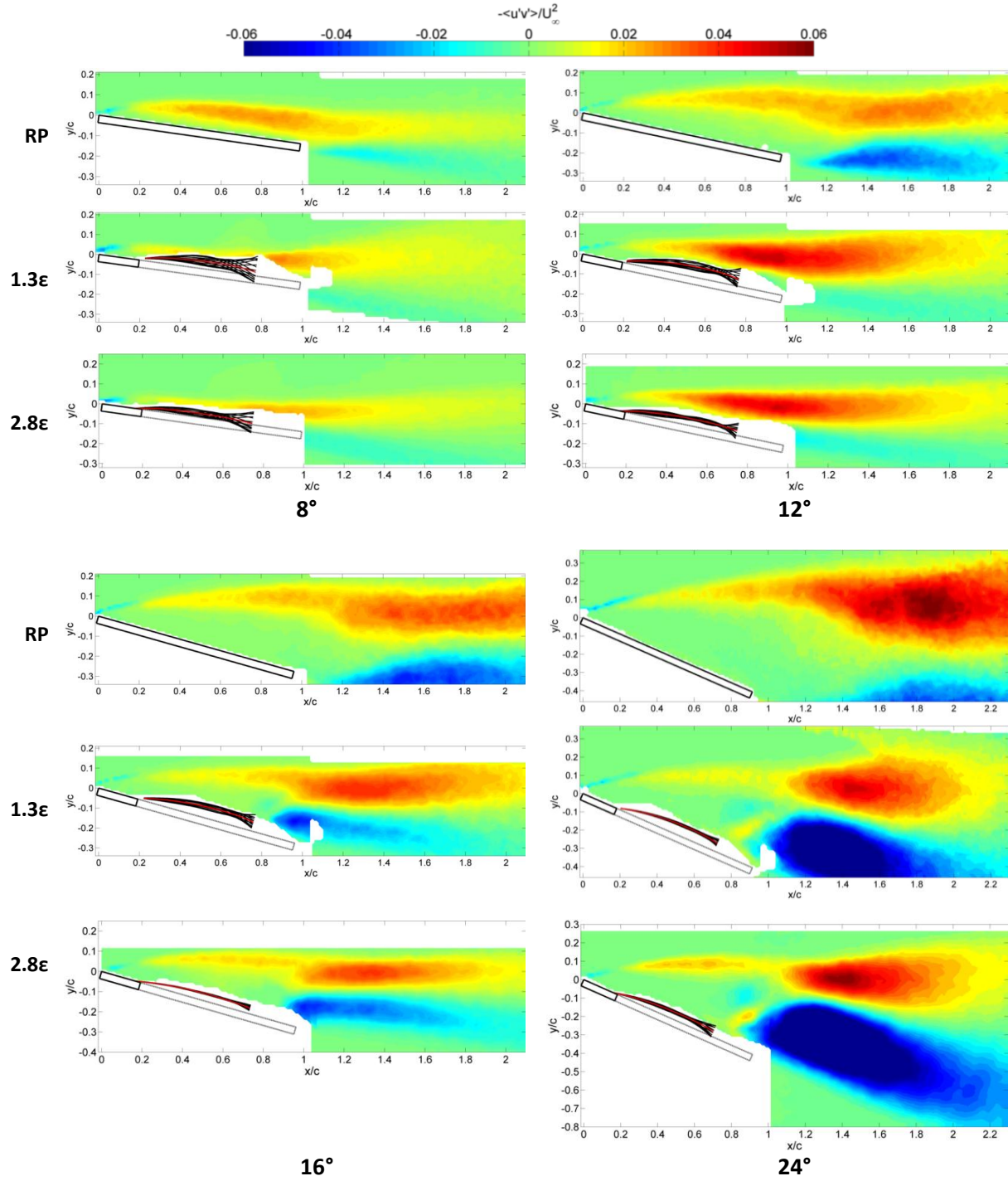**Figure 53.** RSS/U_∞^2 contours on the wings centerline plane comparing RP and membrane wings: 8°, 12°, 16° and 24°

Figure 54 provides an example of the time-resolved development of counter-clockwise vorticity forming at the membrane TE (alluded to in the previous paragraph) as it passes down for α = 24°. These instantaneous data sampled at 450 Hz and synchronized between PIV and DIC for the 1.3% pre-tension wing. A time-scale, τ_f, associated with the membrane dominant cycle frequency (59 Hz for this case), is defined as $\tau_f = t/t_c$, where t_c= 1/59 s and t is time passed. When the membrane is distended maximally up, $\tau = 0$. In these plots vorticity is normalized as: $\omega^* = \vec{\omega}_z \cdot \frac{c}{U_\infty}$. Counter-clockwise rotation (positive vorticity) is shown generated by interaction of flow passing up from under the membrane with flow being pulled down by it. These vorticity structures affect the local streamlines as they advect downstream (0.3 < τ < 0.6). This trailing-edge behavior shows how vorticity formation created by the membrane causes interaction between higher momentum flow further from the model surface and lower momentum flow within the turbulent free shear layer.
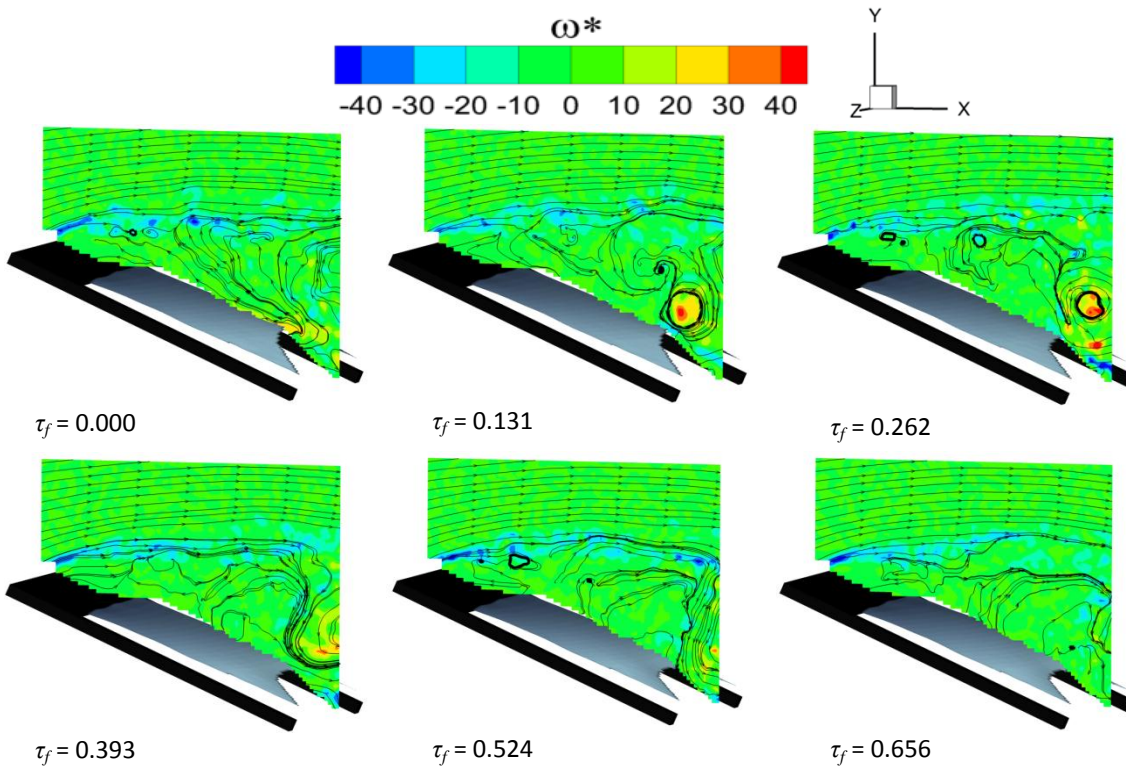
Figure 54. Normalized time-resolved vorticity for 1.3% pre-tension wing at α = 24°

Membrane Motion

General characteristics of the membrane vibrations are determined by investigation of the mean and RMS displacements of the membrane. The time-averaged and normalized membrane displacements (normal to model surface) for ε = 1.3% and 2.8% at α = 8°, 12°, and 16° are presented in Fig. 55. These mean displacements show a clear dependence on pre-tension and angle-of-attack, where lower pre-tension allows larger displacements, as does higher α. The increased α provides a larger membrane frontal area (cb'sin$\alpha\cdot$) and greater effective dynamic pressure forces ($F_{q_{eff}} \sim \frac{\rho U_\infty^2 \cdot cb' \sin \alpha}{2}$) on average. The maximum average displacements occur near the geometric center of the membrane and slightly toward the TE for larger distention. Also, the pattern of the mean membrane deformation shows

that the higher pre-tension model does not significantly change between 12° and 16°, while the deformation of the low pre-tension membrane increases ~20% over the range, implying the mean shape is a stronger function of pre-tension than the effective dynamic pressure forces (as based on frontal area).
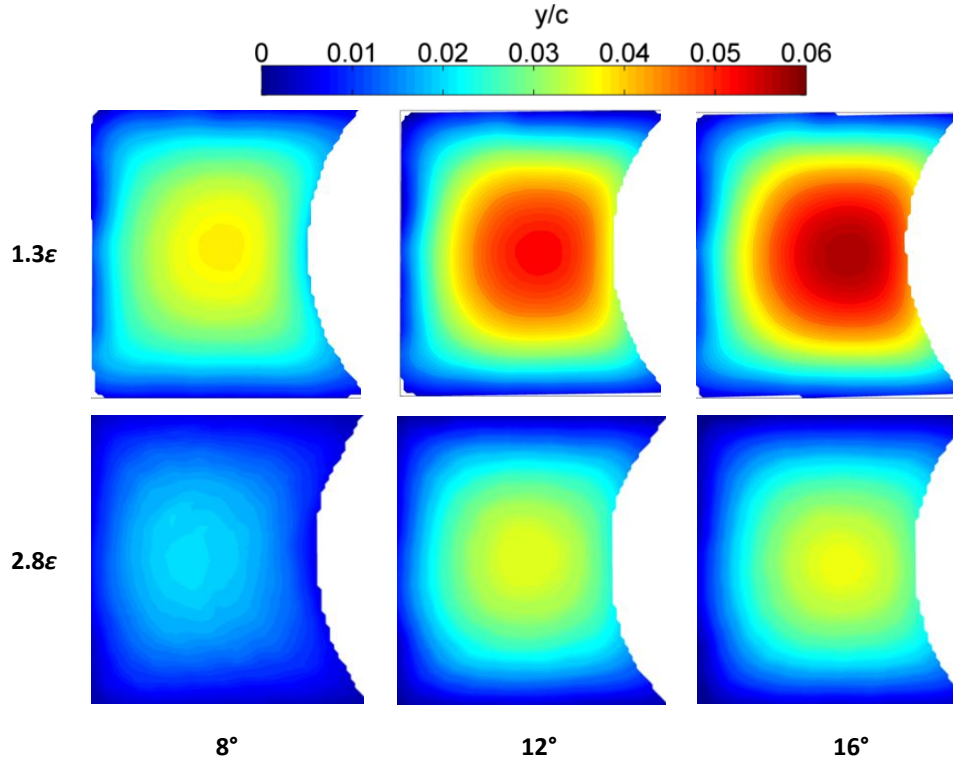
Figure 55. Mean membrane displacements normalized by chord: 8°, 12° and 16°

The normalized RMS membrane displacement contours are plotted in Fig. 56 . They show that the maximum membrane fluctuations occur at the trailing edge and a smaller second peak occurs near the geometric center. At higher angles-of-attack, the RMS tapers off significantly in magnitude and the vibration pattern becomes steadier as the flow tends toward greater separation. Specific points on the membrane surface such as the mid, side, and TE points as designated in Fig. 57 are utilized to further investigate how the membrane behaves over a large range of α. In Fig. 58, the mean and RMS (as bars) of the mid and TE points are plotted versus α for both membrane wings. The time-averaged displacements generally increases with angle-of-attack, while the vibration amplitudes are much larger at lower angles-of-attack ($\alpha \leq 12°$) when the shear layer interacts with membrane and before the flow tends towards being massively separated. Additionally at these lower angles-of-attack the membrane is not subject to large amounts of aerodynamic tensioning which would tend to damp out vibrations. The largest fluctuations occur between 4°–8° range, during which L/D was maximum and significantly higher than the baseline. These fluctuations are larger for the lower pre-tension wing, as was L/D, indication of the possibility of the unsteady behavior passively manipulating the flow to aerodynamic benefit in addition to the steady camber effect discussed below.
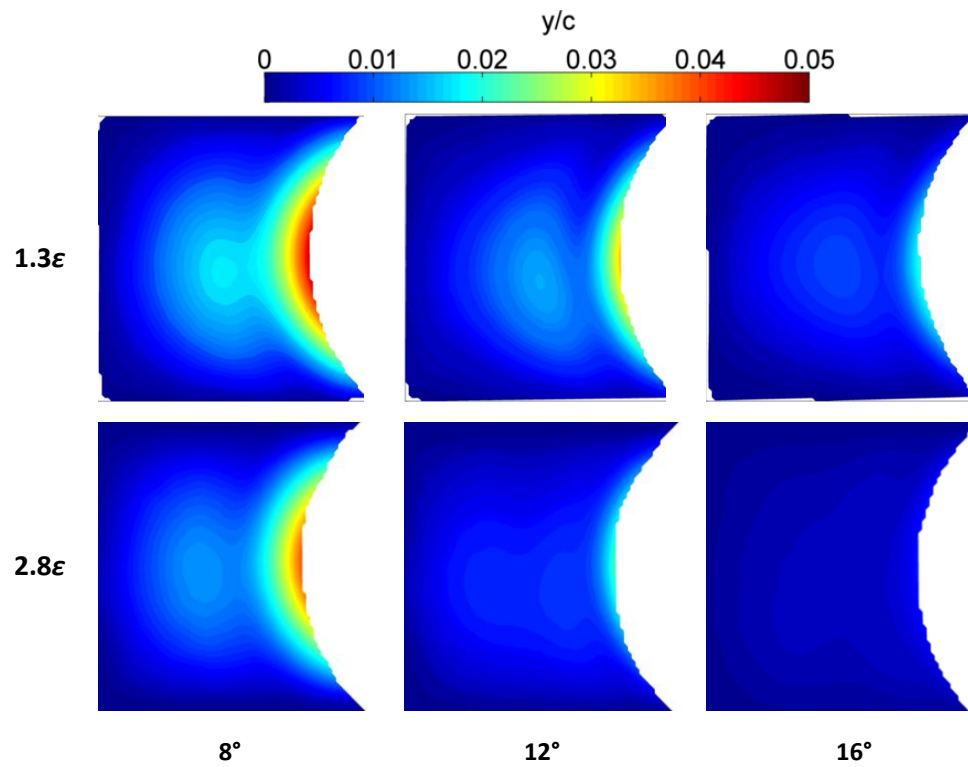
Figure 56. RMS membrane displacements normalized by chord: 8°, 12° and 16°
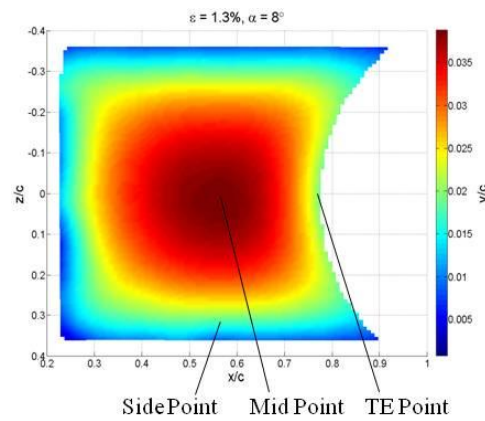
Figure 57. Indication of mid, side, and TE points on 1.3ε wing mean displacement plot: α = 8°
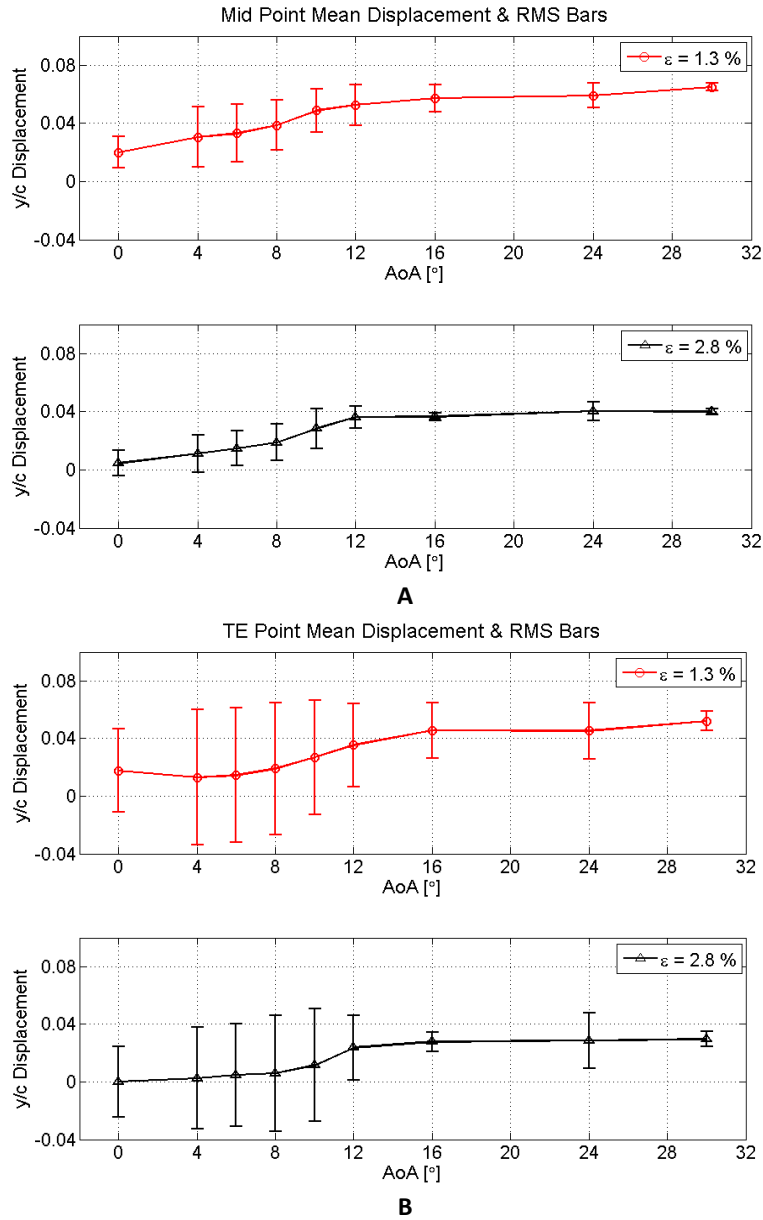
Figure 58. Mean and RMS displacements vs α for A) membrane mid points and B) membrane TE points

In a steady sense, the membranes show an adaptive camber effect. The time-averaged mid and TE points are plotted vs α together for both wings in Fig. 59A, where the difference between the mid and TE displacement represents an effective camber. Further analysis shows that this effect increases with angle-of-attack to a peak at α = 10° for both wings (2.2% c for ε = 1.3% wing and 1.7% c for ε = 2.8% wing), then declines and stabilizes, existing over the whole α-range (Fig. 59B). In this manner, the membrane passively forms a cambered shape, adapting to changing α (pressure) or during gusty conditions (gust alleviation or rejection). Comparing the two membrane wings, the effective camber of the 1.3% pre-tension wing is 1.4 times greater (averaging over the tested α range) and 1.81 times

greater in the maximum efficiency range (4–8°) than the 2.8% pre-tension wing. The effective time-averaged camber over all tested angles was found as 1.5% c and 1.1% c for ε = 1.3% and 2.8%, respectively.
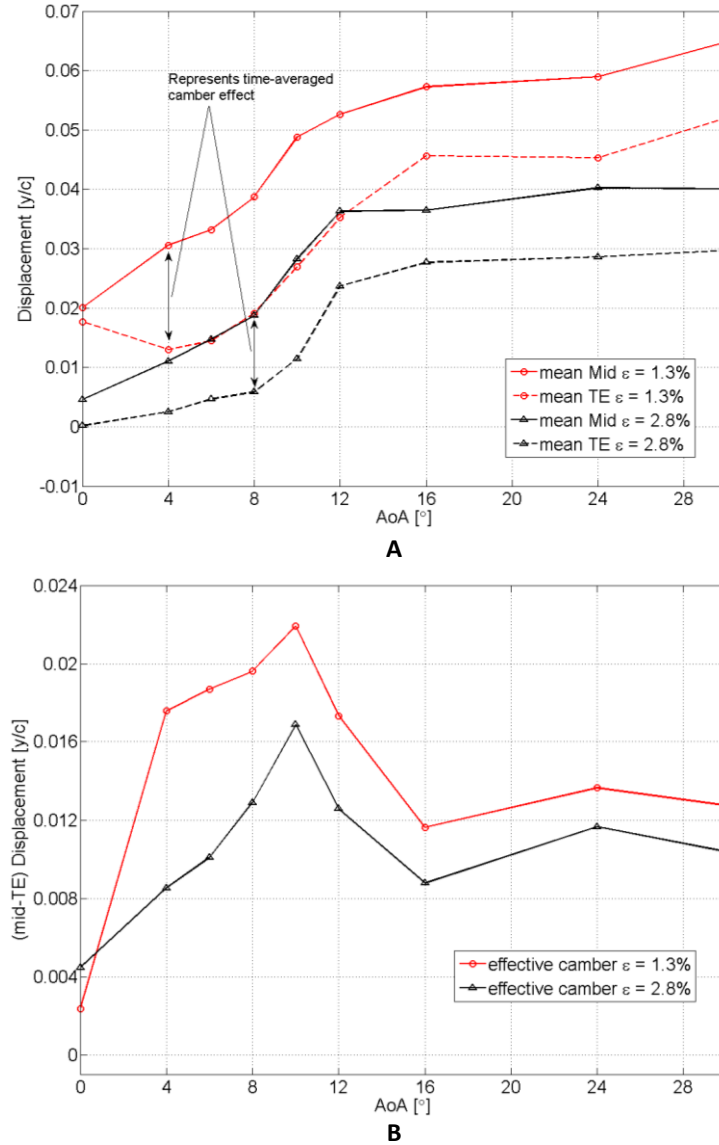
Figure 59. Effective camber of membrane wings: A) time-averaged displacements of mid and TE points vs α and B) effective camber comparison vs α

The time-resolved membrane signals were utilized to compute the power spectra allowing for analysis of the frequency content of their motions. Typical curves of the power spectra computed from the fluctuating displacements for the mid, side, and TE points are plotted in Fig. 60. The spectra show clear peaks at the dominant vibration frequency and often many strong harmonics. The dominant spectral peaks of these wings can be tracked for the full α-sweep, and the peak vibration frequencies are plotted vs α for each wing in Fig. 61. For both wings there is a similar trend of increasing frequency with angle from 4 to 12°, presumably as the average overall tension is increased and also associated with when the flow remaining at least partially attached. The peak frequencies are essentially constant after 12°, plateauing near 60 Hz. As expected, the high pre-tension wing (ε = 2.8%) vibrates faster than the low pre-tension wing: 7.6% increase for the full α-range and 10.8% increase over the pre-stall range of α < 12°. For the pre-stall range, assuming a linear trend with pre-tension, the vibration frequency increases by 7.2% per 1% increase in pre-strain or 3.7 $Hz/\%\varepsilon$. The 1.3% pre-tension wing vibrates at an overall average peak frequency of 54 Hz and the 2.8% pre-tension wing at 58 Hz, each near an estimated natural frequency of 55 Hz based on the membrane stiffness, *Et*, and mass.

Of interest is that the membrane vibration frequency at low angle-of-attack (< 12°) increases with angle-of-attack (aerodynamic tensioning, similar to Song *et al.,* 2008) and membrane pre-tensioning. If this was driven by blunt-body shedding, then as the projected height of the model increased with angle-of-attack the corresponding frequency would decrease, assuming constant Strouhal scaling (not increase as shown in Fig. 61). Typically, flat plates do not present blunt-body shedding at low angle-of-attack (Knisely 1990). It is believed that the selected membrane vibration frequency at low angles-of-attack is determined by the material and geometric properties of the membrane as well as the membrane pre-tension once a threshold (onset) level of broadband turbulent intensity within the shear layer excites the membrane (Scott *et al.,* 2012). At higher angles-of-attack, blunt-body shedding likely plays a more significant role. As Fig. 61 displays, above 12°, the dominant frequency for both pre-tension values are now about the same (tensioning-independent) and have decreased relative to the peak frequency values at lower angle-of-attack. Based on the projected chord height at 24°, the corresponding Strouhal number of the measured membrane frequency is 0.18—a value indicating a relationship to blunt-body shedding. This value is close to the 0.17 value presented in Rojratsirikul *et al.* (2011) although there some ambiguity of the proper length to use with the wings in the current study due to the scalloping.
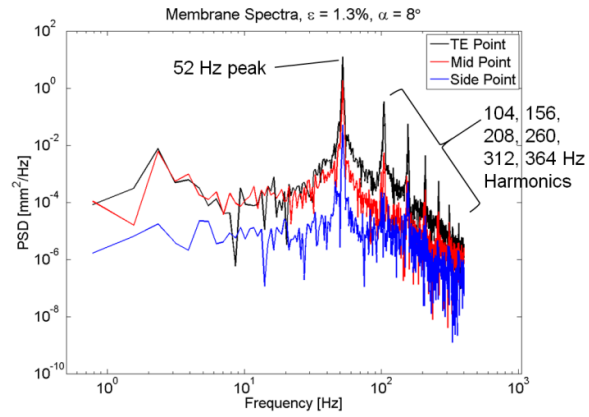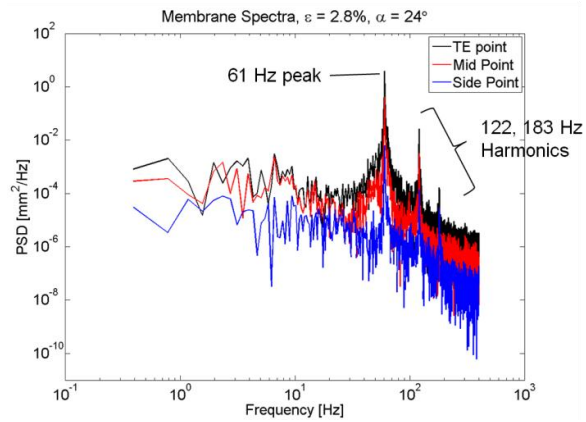
Figure 60. PSD computed from fluctuating signals: A) 1.3ε wing at α = 8° and B) 2.8ε wing at α = 24°
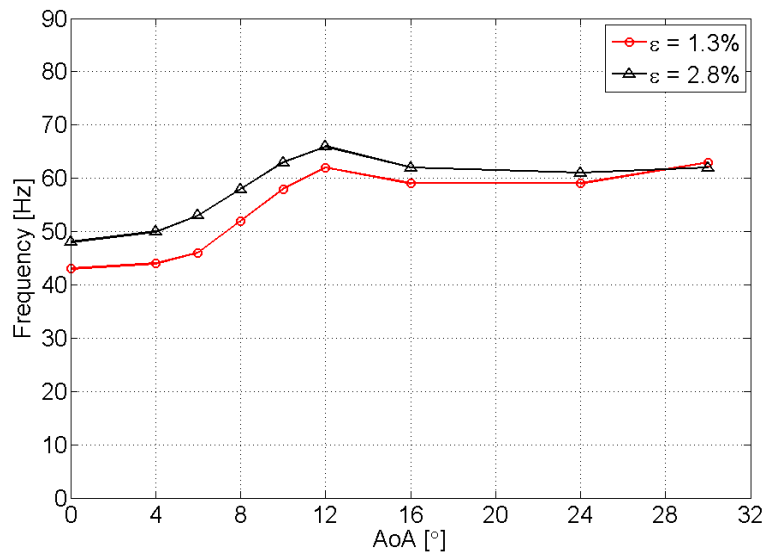
Figure 61. Dominant vibration frequency vs α comparing 1.3ε and 2.8ε

In a dynamic sense, the dominant periodic feature of the membrane motion appeared as a leeside bulging usually emanating near the quarter-chord of the model then traveling (and growing in size) toward the trailing-edge where the windward pressure could be released. Correspondingly, flow streamlines show fluid emanating from under the membrane as the TE distends upward (Fig. 54, τ_f = 0.0). At the highest tested angles-of-attack (α = 24° and 30°), specifically for higher pre-tension, the pressure bulge does not always reach the TE and seemingly reverses direction. Overall, the vibrations of the free trailing-edge membrane appear different from the modal and standing wave behaviors found for membrane wings with fully supported membrane edges (Rojratsirikul *et al.*, 2011; Tregidgo *et al.*, 2011), indicating a traveling wave phenomena with less definitive nodes. Figure 62 shows a segment of instantaneous membrane surface deflections at the center of the model (center of the middle membrane of a 3-cell, *AR* = 2 wing). In these plots the vertical axis represents the chordwise direction of the wing while the horizontal axis represents time. The plots are for a 4% pre-tension at α of 8°, 12°, and 16°; however, a 1 percent pre-tension membrane wing exhibited similar behavior. These normalized deflections visually show the wave type behavior of the membranes motions. The membranes motions have features of both a standing wave and traveling wave. A pure standing wave would plot straight vertical lines of alternating colors; this can be seen in the lower portion of the plots (leading edge of wing). A pure traveling wave would plot diagonals line of alternating colors; this can be seen in the upper portion of the plots (trailing edge of wing). This behavior represents an interesting phenomenon since the convection of the traveling wave will lead to the temporal behavior of the vorticity being shed at the trailing edge. Further investigation and analysis of this wave phenomenon is ongoing.
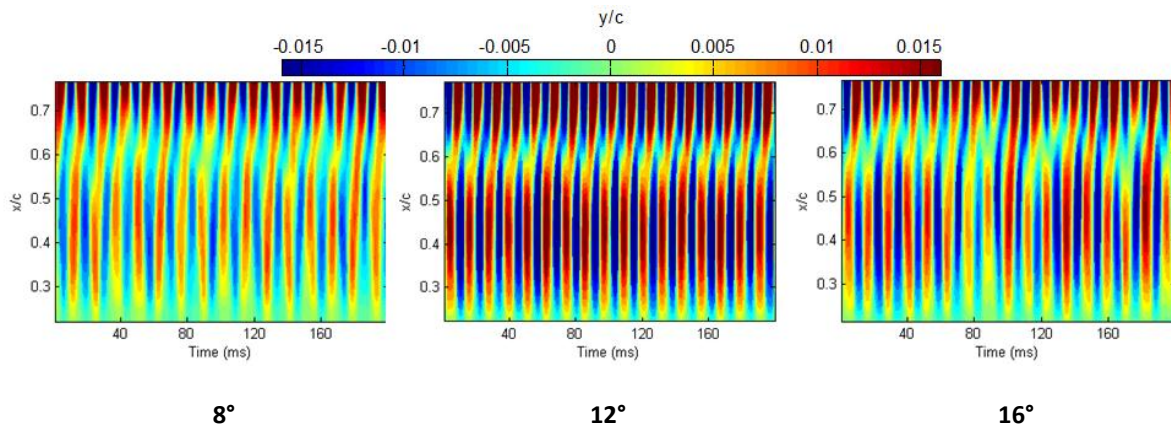
Figure 62. Instantaneous membrane surface deflections of the 4% pre-tension membrane at α of 8°, 12° and 16°

Fluid-Structure Coupling

To further demonstrate that the membrane drives the flow at low angles-of-attack, velocity spectra and correlations between the membrane and the flow are presented and discussed in this section. In a similar manner to that described in the previous section, velocity power spectra are used to find the dominant frequencies of the fluctuating velocity.

Figure 63 Figure 63 is an example data set showing PSD of the fluctuating velocity computed at the indicated flow locations for the 1.3ε wing at α = 8° overlaid with the PSD of the membrane TE location. The dominant flow fluctuation frequency of 52 Hz as well as many of the harmonics associated with the membrane oscillations are retained further downstream in the flow, well into wake. This

supports the results discussed above distinguishing the free trailing-edge membrane effect on the wake at low angles-of-attack. Within the recirculation region or near the LE shear layer, dominant membrane frequencies were generally not detected, giving way to broadband spectra.

A

B
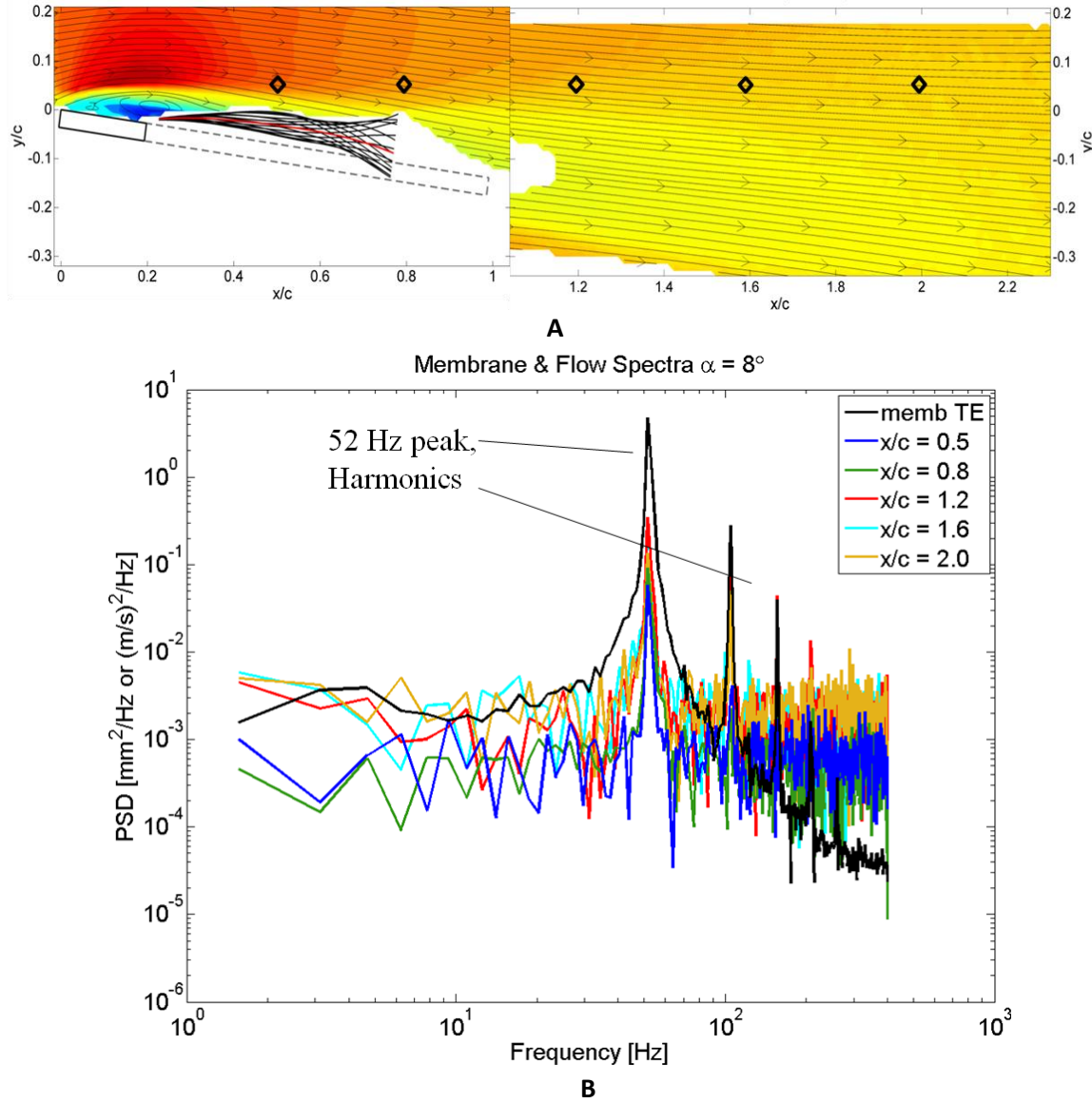
Figure 63. PSDs showing membrane frequency in the flow field for 1.3ε, α = 8°: A) locations of PSD indicated by diamonds over $\overline{u}$ plot and B) PSD of membrane TE and corresponding wake fluctuations

Correlations between the membrane and the velocity field were computed between several locations on the membrane and the center span PIV plane. The correlations were calculated as a linear correlation coefficient with zero time-lag, defined as:

$$\rho(\tau_0) = \frac{1}{N}\sum_{i=1}^{N}(d'_i u'_i) \ / \ (\sigma_{d'}\sigma_{u'}) \tag{7}$$

In this equation d' represents the fluctuating membrane displacements while u' represents the fluctuating velocity component i.e., u' or v'. These correlations were computed with data from the 1.3ε wing synchronized acquisition sets.

Figure 64 contains contours of the correlation coefficient between d' fluctuations at the TE point of the membrane, indicated with diamond symbols in the plots, with v' fluctuating velocity components for $\alpha = 8°$, 12° and16°. The use of the TE location as the correlation point on the membrane was due to the larger fluctuations in the signal at this location although the results are similar when using other points on the membrane. Throughout these plots there are positive and negative correlation values indicating either in-phase or out-of-phase relationships between the membrane motion and the velocity field. The correlation plots displayed are for zero time lag. Although not shown here, varying time lags show a periodic translation of the correlated flow fluctuation convected downstream. The contours of the correlation coefficients between the vertical velocity and the membrane exhibit an evolving behavior as the angle-of-attack is increased. For the smallest angle-of-attack ($\alpha = 8°$), there is a large positive, highly correlated region near and above the TE of the wing. This implies that the velocity fluctuations in this area are in-phase with and induced by the membrane motion. While the large negative values of the correlation coefficient in the wake imply an out-of-phase relationship. As the angle-of-attack is increased to 12° and 16°, the region of highly correlated, in-phase motion diminishes in intensity and moves away from membrane, indicating less importance of the membrane interaction with the flow as the wing acts more like a bluff body. This evolution is consistent with the discussions from the previous section. Namely, that for relatively low angles-of-attack the membrane motion is driven by the membranes natural frequency, which is due to the combination of pre-tension and aerodynamic tensioning, and it is forcing the features in the wake. However, as the angle-of-attack is increased enough to where the wing can set up bluff-body shedding the phenomena of vortices rolling up in the wake begins to dominate.

Vibration Scaling (Zheng *et al.*, 2013b)

As discussed in the previous sections, the vibration is a function of flow velocity, wing angle-of-attack, membrane geometry, membrane properties, and membrane pre-tensioning. Figure 61 is a representative example which shows the dominant membrane vibration frequency of a batten-reinforced, scalloped membrane wing over a 30° angle-of-attack range and two pre-strain levels. For low angles-of-attack, prior to the onset of stall conditions ($\alpha \leq 12˚$), the frequency increases with angle-of-attack (aerodynamic loading) and membrane pre-strain. At higher angles-of-attack, the frequency shows less dependency on pre-strain and angle-of-attack. In this post-stall region, the effective tensioning of the membrane is relatively constant and becomes more susceptible to blunt-body shedding effects.

Three commonly used nondimensional scalings for frequency, material stiffness and membrane tension relative to flow conditions (Eqs. 8, 9 and 10, respectively) are

$$St = \frac{fc}{U} \tag{8}$$

and
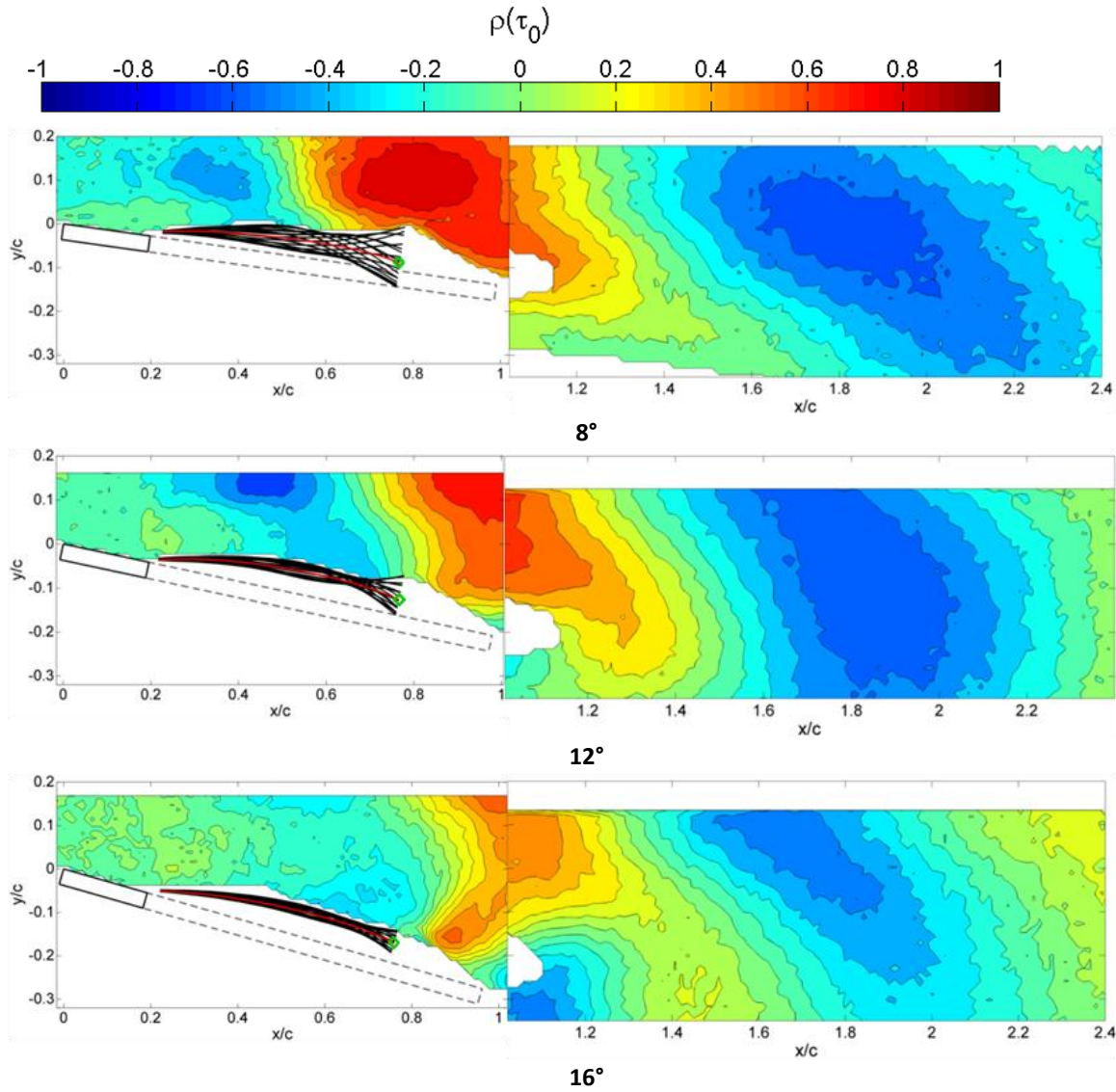
Figure 64. Cross-correlation coefficient of membranes trailing edge with the vertical component of velocity

$$\Pi_1 = \left(\frac{Et}{qc}\right)^{1/3} \tag{9}$$

or

$$\Pi_2 = \frac{\sigma t}{qc} \tag{10}$$

where aeroelastic similarity parameter Π_1 is applicable in the case of vanishing membrane tension and Π_2 in the case of vanishing material stiffness [Shyy *et al.*, 2007]. The chord is often used as the characteristic aerodynamic length, but this will be discussed later. These two aeroelastic parameters arise from the nondimensional form of the Young-Laplace equation for a uniformly tensioned 2D

membrane. The one-third power of Eq. 9 arises from a nonlinear solution of rectangular membranes [Seide, 1978] such that when pre-tensioning is negligible relative to the flow-induced membrane stress, the maximum membrane deflection is proportional to c/Π_1.

Strouhal scaling is often appropriate for blunt-body shedding, e.g. the $St_{cyl} \sim 0.2$ for a wide range of Re. For low-thickness (streamlined) bodies at high-α, the projected chord, $c\sin\alpha$, is usually used as the scaling parameter. At low-α, flat plates do not exhibit strong blunt-body shedding [Knisely, 1990], and membrane vibration is instead driven by broadband turbulent energy exciting the structural frequency of the membrane. As shown in Fig. 61, as the angle-of-attack increases, the frequency increases. However, neglecting aerodynamic tensioning, a relatively constant Strouhal number phenomenon based on blunt-body shedding would predict a decrease in frequency due to the increase of the projected chord as angle-of-attack increases.

Figure 65 demonstrate the wide scatter in data for Strouhal scaling of free trailing-edge membrane wings (see Table 3 for data sources) relative to Π_1 and Π_1/C_L, respectively. For all of these models, membrane cells were formed by attaching the membrane along three sides of a rigid cell, leaving the TE free to vibrate. Some models had multiple spanwise cells. In the case of Π_1 (Fig. 65A), dynamic pressure is considered (one source of aerodynamic tensioning), but the scaling does not account for applied tensioning, ε_o, or lift tensioning (by means of α). Dividing by the lift coefficient (Fig. 65B) is an alternative scaling to account for lift-based aerodynamic tensioning (an inverse form of Weber number, Song *et al.*, 2008). While a negative correlation is present for data set 1 (square symbol), a broad range of data scatter exists when comparing different membrane spans and pre-tension levels from the other data sets. The vanishing material stiffness aeroelastic parameter, Π_2, would seem to be a more appropriate scaling parameter since it accounts for membrane tension. Figure 66 plots the Strouhal-scaled trend where pre-stress is approximated by $\varepsilon_o E$. Again, the data exhibits a negative correlation but does not collapse along a general trend. One reason for this is that the applied strain and the aerodynamically-induced strain are effectively multiplied; thus, when either one is zero, the tensioning effect is zero—a false case.

Table 3. Test and membrane conditions for various free trailing-edge membrane investigations (data for Figs. 65 and 66).

	Data Set	Re	q [Pa]	AR	α [°]	b'/c	Cells	ε_o	Scalloped
1	Timpe *et al*, 2012	50K	60	4.3	0-12°[a]	80%	5	1.3,2.8,4.2	Yes
2	Zhang *et al*, 2013	50K	60	2	8°	60%, 93%	2,3	1,2,4	Yes
3	Hubner and Hicks, 2011	25K-50K	30-60	∞[b]	8°	40%-80%	5,9	0[c]	Yes
4	Scott *et al*, 2012	10K-30K	2.5-22	∞[b]	8°	40%-80%	1	0[c]	No

a. Higher angles-of-attack tested but outside the linear lift range
b. $AR = 5$ but the membrane was within the potential core of an open jet
c. No applied pre-tension other than membrane self-weight
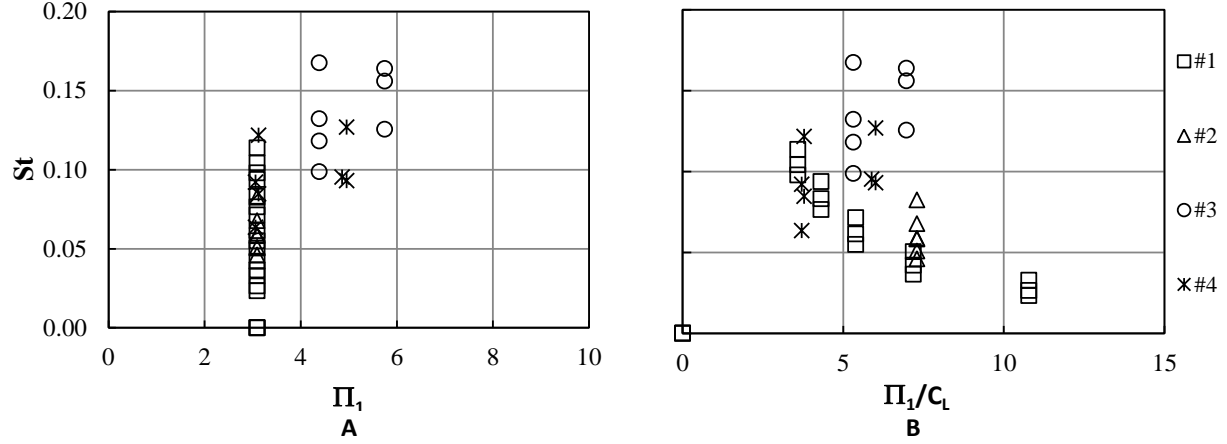
Figure 65. The nondimensional membrane vibration frequency in terms of Strouhal number vs the aeroelastic similarity parameters A) Π_1 and B) Π_1/C_L (Note: St = 0 points correspond to α = 0 and Π_1/C_L = ∞)
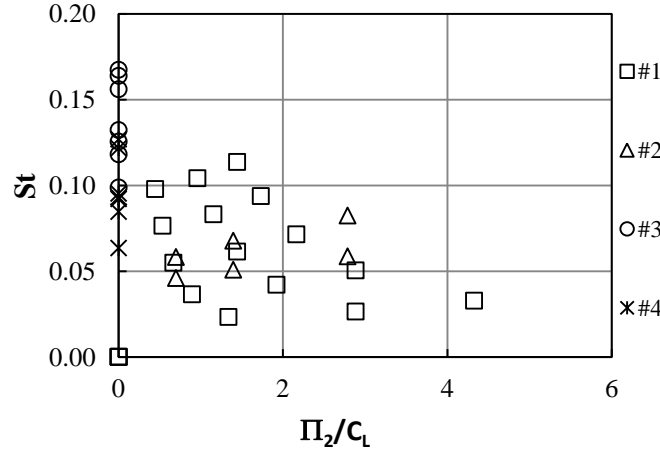
Figure 66. The nondimensional membrane vibration frequency in terms of Strouhal number vs the aeroelastic similarity parameters Π_2/C_L

Clearly, the Strouhal scaling is not appropriate. A simplified theoretical framework is proposed and developed, applicable to membrane wing geometries at low or moderate angles-of-attack that includes both applied and aerodynamically-induced strain as well as membrane properties of modulus of elasticity, thickness, and aspect ratio. Then, the proposed scaling is compared and evaluated with tests results from models with a free leading and trailing edge and with previously published results from data sources listed in Table 3.

<u>Scaling Model</u>

As a starting point, only the fundamental frequency is considered, and higher harmonics and mode shapes of the membrane vibration are neglected. As shown in Abudaram *et al.* (2013), the spanwise strain of a free trailing-edge membrane is greater and more uniform than the chordwise strain. Thus, the resulting flow-induced membrane vibration is broadly analogous to a vibrating string or

2D membrane tensioned in the spanwise direction. As such, the fundamental frequency for a tensioned string is

$$f \propto \sqrt{\frac{T}{ml}} = \sqrt{\frac{T}{mb'}} \tag{11}$$

where the characteristic length l is set to b', the membrane span, and the mass is related to the membrane density and volume:

$$m = \rho_m c'b't . \tag{12}$$

The tension in the membrane arises due to applied pre-tension, aerodynamic loading, and membrane weight. In terms of strain and the membrane modulus, the spanwise tension is modeled as

$$T = \varepsilon E c't . \tag{13}$$

Substituting Eqs. 12 and 13 into Eq. 11 yields

$$f \propto \sqrt{\frac{\varepsilon E}{\rho_m} \frac{1}{b'}} \tag{14}$$

Defining a nondimensional frequency in terms of Eq. 11 results in

$$f^* = fb' \sqrt{\frac{\rho_m}{(\varepsilon_o + \varepsilon_a)E}} . \tag{15}$$

The strain is modeled as the linear summation of two components: applied pre-strain and aerodynamically-induced strain

$$\varepsilon = \varepsilon_o + \varepsilon_a . \tag{16}$$

This is a reasonable assumption for membranes as long as the strain does not induce nonlinear characteristics, $\varepsilon < 10\%$. To model the effect of aerodynamic loading, the 2D membrane analogy is expanded by assuming a uniform pressure loading that produces a catenary membrane shape. The average aerodynamic loading acting across the unit span of a wing is estimated by lifting-line theory (neglecting low Reynolds number and separation effects):

$$L' = C_l qc = a\alpha qc , \tag{17}$$

where a is the lift curve slope,

$$a = \frac{2\pi}{1 + \frac{2}{AR}(1+\tau)} , \tag{18}$$

If the membrane is mounted in the horizontal plane, the effect of distributed weight can also be considered. Because the lift is assumed to act upward, the effect of the weight is subtracted. Thus, the membrane lift distribution adjusted for weight is

$$L'_w = L' - \frac{W_m}{b'} = a\alpha qc - \rho_m gc't. \tag{19}$$

The induced catenary shape due to a uniform load distribution is (Beer and Johnston, 2007)

$$y = \frac{T_o}{L'_w} \cosh\left(\frac{L'_w x}{T_o}\right) . \tag{20}$$

Eq. 20 can be solved iteratively by matching the spanwise strain based on the change in the membrane length due to the distributed load,

$$\varepsilon_a = \frac{b_l' - b'}{b'} \tag{21}$$

to the spanwise strain based on the calculated membrane tension,

$$\varepsilon_a = \frac{\bar{T}}{E c' t} . \tag{22}$$

The tension, T, is not uniform across the membrane; therefore, an average tension is used. That said, the difference between the maximum and minimum tension is usually less than 10%.

For a vertical membrane, the weight does not affect the catenary shape. Instead, the weight-induced strain is added to the applied pre-strain,

$$\varepsilon_o = \varepsilon_{o,app} + \frac{\rho_m b' g}{2E} . \tag{23}$$

For typical applied and aerodynamically-induced strains, the weight effect for the vertical or horizontal orientation is small and negligible: $\varepsilon_w < 0.1\%$.

Model Assessment

To assess the proposed frequency scaling, a 2D membrane attached between two rigid (aluminum) plates was tested in low-Re flow, Fig. 67. This set-up is designated as the free LE-TE configuration because the membrane's leading and trailing edges were unattached—free to vibrate. This configuration was chosen to create a spanwise dominated applied stress. The rigid plates were extended to the walls of the tunnel to eliminate tip vortex effects. The vertical position of the bottom plate was connected to a PC-controlled linear traverse to set the desired pre-tension. Target markers were painted on the membrane leading edge (LE), midpoint (MP) and trailing edge (TE) to track the membrane vibration frequency by means of high-speed imagery. Further details are discussed in the following sub-sections.
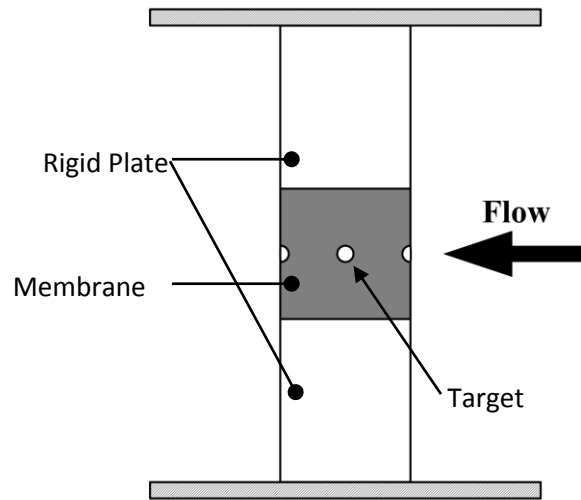

Figure 67. Schematic of the spanwise tensioned membrane in flow

70

Three variants of silicone rubber membrane were tested with cell aspect ratios of 0.5 and 1. Properties of the material are listed in Table 4. Table 5 lists the range of tests performed—a total of 36.

Table 4. Properties of silicone rubber material

	t [mm] $\pm0.3\%$	E [Pa] $\pm5.5\%$	ρ_m [kg/m^3] $\pm1\%$	Hardness[a]
Membrane 1 (M1)	0.32	450	1065	20A
Membrane 2 (M2)	0.52	500	1075	20A
Membrane 3 (M3)	0.08	1900	1030	55A

a. As reported by the manufacturer

Table 5. Wind tunnel and membrane test conditions

	b'/c'	q [Pa]	α [°] $\pm0.2°$	ε_o [%] $\pm0.05\%$	Tests
Membrane 1 (M1)	1.0	15, 60, 135	$0-16, \Delta4$	$0-8, \Delta2$	21[a]
	0.5	60	4, 8	4, 8	4
Membrane 2 (M2)	1.0	60	4, 8	4, 8	4
Membrane 3 (M3)	1.0	60, 135	4, 8	2, 4, 8	7[a]

a. Not all permutations tested

Theoretical aerodynamic strain results based on the simplified catenary load model proposed in the earlier section are plotted in Fig. 68 for a range of typical lift per unit span values, L'. The baseline membrane model is similar to M2 in Table 4. The trend lines follow a power law trend of $^2/_3$, thus,

$$\varepsilon_a = AL'^{2/3}. \tag{24}$$

The constant, A, increases as the membrane span increases and modulus of elasticity, thickness and membrane chord decrease.
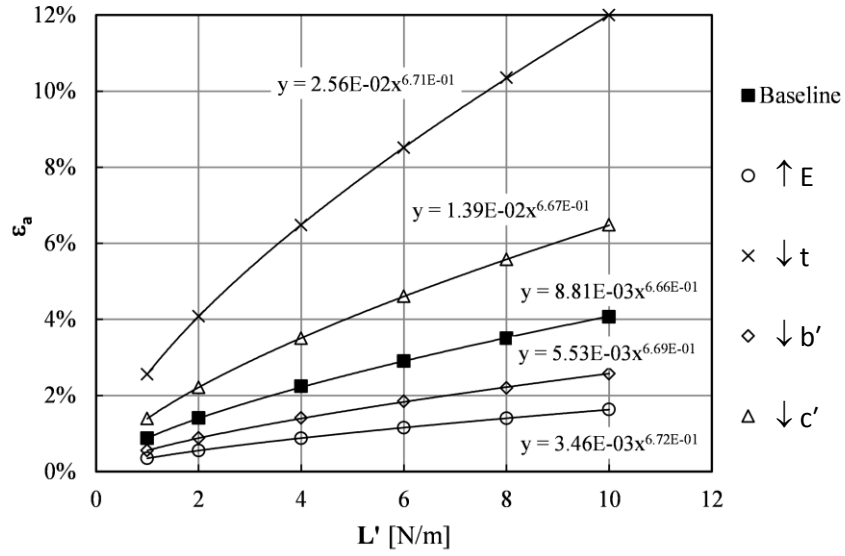
Figure 68. The calculated aerodynamically-induced strain due to lift generation relative to various membrane parameters

The curves of Fig. 68 can be collapsed by defining the following constant of the relevant membrane parameters to the eliminate the units of L':

$$k = \frac{b'}{Etc'} \tag{25}$$

and rearranging Eq. 24 with a non-dimensional coefficient A^*. Plotting A versus $k^{2/3}$, Fig. 69, yields a value of $A^* = 0.348$. Thus, Eq. 24 becomes:

$$\varepsilon_a = A^*(kL')^{2/3} = 0.348(kL')^{2/3}. \tag{26}$$

Figure 69. Calculation of the nondimensional coefficient, A^* for Eq. 26

Equation 26 provides an estimate of the aerodynamically-induced strain based on membrane parameters, implementing the assumptions that the lift-generating pressure distribution across the membrane is uniform and stationary—both are simplifications of the true state of the membrane. To express this in terms of the vanishing tension aeroelastic parameter, Eqs. 17 and 25 are substituted into Eq. 26 to yield

$$\varepsilon_a = A^* C_l^{2/3} \Pi_1^{-2}. \tag{27}$$

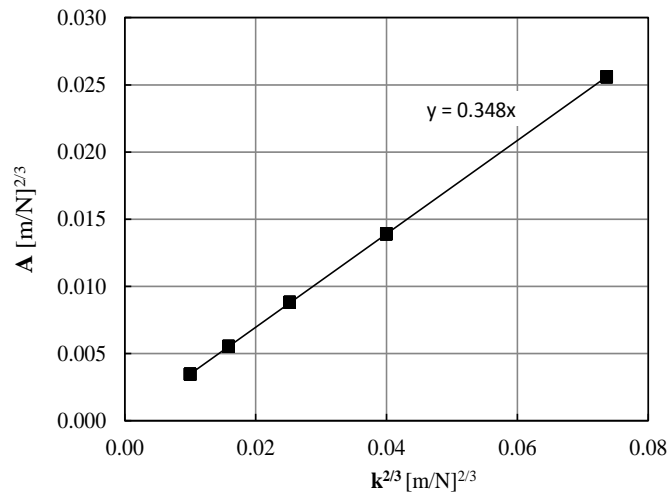Now, Π_2 can be defined relative to Π_1. Defining both relative to the membrane span—the predominant direction of the applied and aerodynamically-induced strain due to the free leading and trailing edges—and estimating the stress as εE, Π_2 becomes

$$\Pi_2 = \frac{\varepsilon E t}{q b'} = \frac{(\varepsilon_o + \varepsilon_a) E t}{q b'} = \varepsilon_o \Pi_1^3 + \varepsilon_a \Pi_1^3 \tag{28}$$

Substituting Eq. 27 into Eq. 28 yields

$$\Pi_2 = \varepsilon_o \Pi_1^3 + A^* C_l^{2/3} \Pi_1. \tag{29}$$

Thus, the lift coefficient acts as a tensioning agent (positive power) as opposed to a material stiffening agent (negative power). For the membranes studied in this investigation, Π_1 ranged between 2.4 and 4.9, and wing lift coefficients ranged between 0 and 1. Figure 70 plots the effect of applied strain, ε_o, on the tensioning aeroelastic parameter, Π_2, for a range of Π_1 values (2.0, 3.5 and 5.0) and lift coefficient values (0.5 and 1.0). Trends from the plot show that the applied strain dominates aerodynamic strain once $\Pi_1 > 2$ (comparing the slope of the lines relative to step change between like symbols). Increasing the lift coefficient tensions the membrane (increases Π_2) and plays a more significant role when the material stiffness is small ($\Pi_1 < 2$).

The fundamental membrane vibration frequency was determined by analyzing, by means of image-processing software, the time-dependent image intensity change induced by the applied surface target points passing through specified regions of interest. Three positions along the centerline chord of the membrane were monitored (as shown in Fig. 67): LE, MP and TE. Figure 71 shows a typical set of power spectral density (PSD) plots of the M1 membrane ($b'/c' = 1.0$, $\alpha = 4°$; $q = 60$ Pa, $\varepsilon_o = 4\%$) normalized by the peak spectral energy of each point. The fundamental frequency and a second harmonic are clearly present. The LE and, particularly, the TE of the membrane, where the chordwise stress is effectively zero, consistently exhibited more vibration energy throughout the spectrum. Thirty percent of the cases, the frequency associated with the peak energy did not match between the three target points. Of these cases, the MP target matched the LE or TE 67% of the time. In cases where the frequency peaks were different, the MP frequency was used in the calculations.
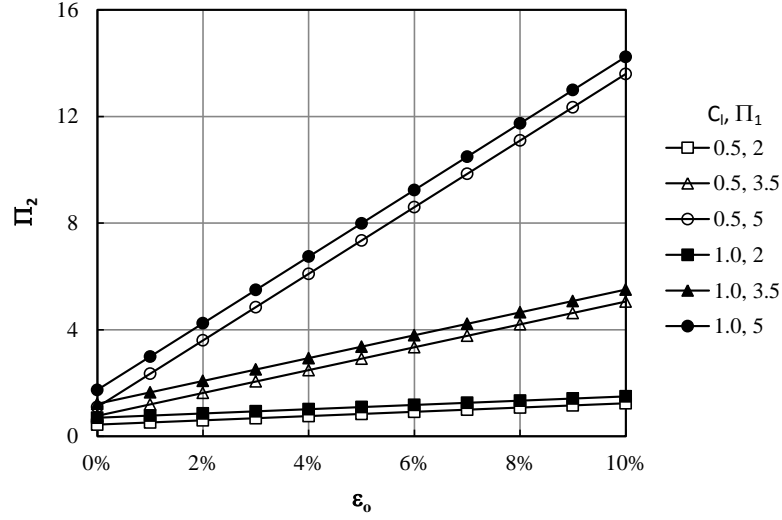
Figure 70. The effect of applied strain, ε_o, on the tension aeroelastic parameter, Π_2, relative to the material stiffness aeroelastic parameter (2.0, 3.5 and 5.0) and lift coefficient (0.5 and 1.0)

Figure 72 plots the scaled frequency, f^*, versus the tensioning aeroelastic parameter, Π_2, for the free LE-TE configuration. The characteristic length is set to b' because the predominant strain orientation is in the spanwise direction. The aerodynamic strain was determined using Eq. 27. The symbol shape designates the membrane type. As displayed, the data exhibits much less variance compared to Figs. 65 and 66. Nominal uncertainty estimates of Π_2 and f^* based on the propagation of the contributing terms (E, t, ρ, b', ε_o, ε_a, V, α, f) are 9% and 4%, respectively. For higher tension, $\Pi_2 > 2$, nondimensional frequency is relatively independent of the tensioning aeroelastic parameter. Based on the bias uncertainty and the precision confidence interval about the *sample mean* and of the *next measure*, respectively, the nondimensional frequency, f^*, is 0.62 ± 0.04 (95%) and 0.62 ± 0.16 (95%). In this high tension region, the membrane frequency, f, increases proportionally with square root of the membrane stress, $\sqrt{\sigma}$, due to either the applied or aerodynamic load:

$$f \sim \frac{0.62}{b'} \sqrt{\frac{(\varepsilon_o + \varepsilon_a)E}{\rho_m}} . \tag{30}$$

As the tensioning decreases ($\Pi_2 < 2$), the nondimensional frequency trends upward. There is one noticeable outlier (arrow). For this test condition (M3, $\alpha = 4$, $\varepsilon_o = 2\%$, $q = 60$ Pa), the LE and MP frequencies matched but were much lower than the TE frequency and other measured membrane frequencies at higher pre-tension or angle-of-attack. If the TE frequency is used to calculate f^* for this specific case, then the measurement falls in line with other membrane measurements. A power law curve fit shows an inverse relationship of $-\frac{1}{3}$. Thus,

$$f \sim \frac{5}{6b'\Pi_2^{1/3}} \sqrt{\frac{(\varepsilon_o + \varepsilon_a)E}{\rho_m}} \tag{31}$$

when $\Pi_2 < 2$. In this region where membrane tension and dynamic pressure are balanced, the membrane frequency is proportional to $\sigma^{1/6}$ due to the dependency of Π_2 on the membrane stress.
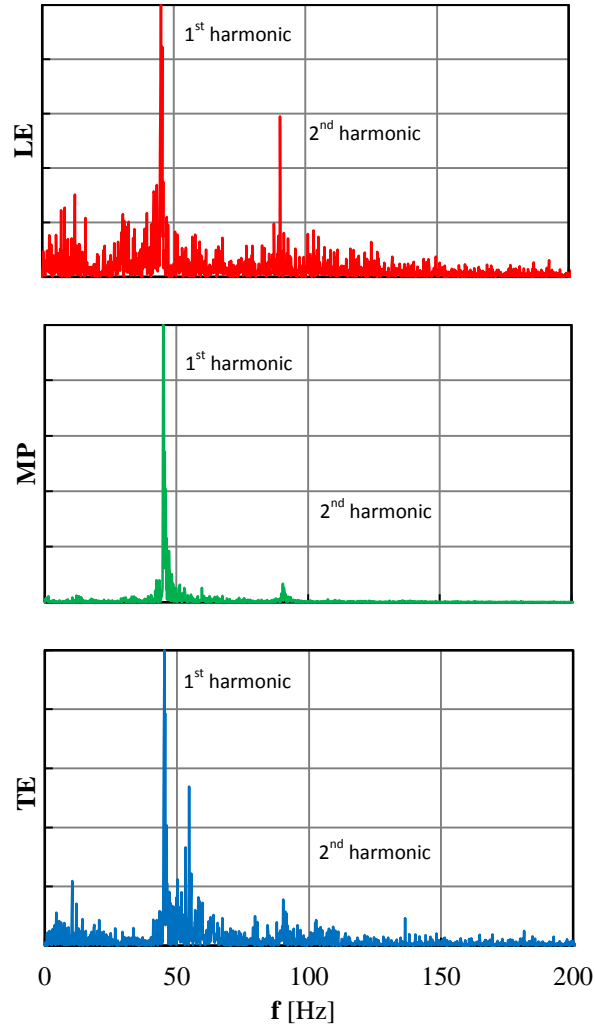
Figure 71. Comparison of the normalized PSD of the LE, MP and TE target points for the M1 membrane: $b'/c' = 1.0$, $\alpha = 4\degree$, $q = 60$ Pa, $\varepsilon_o = 4\%$
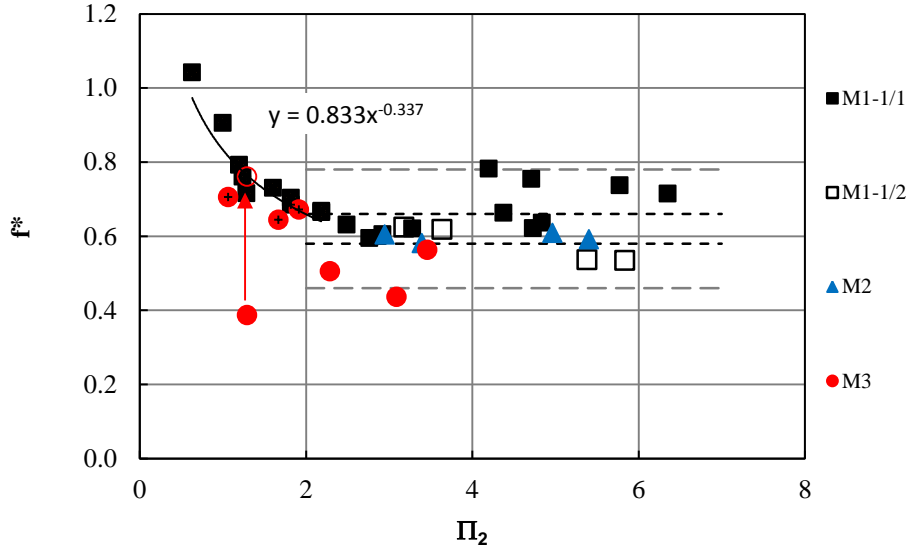
Figure 72. Nondimensional frequency scaling results for the free LE-TE membranes: short dashed lines represent 95% confidence interval of the *sample mean* and long dashed lines represent 95% confidence of the *next measure*

Plotted in Fig. 73 is the proposed scaling applied to the data sets of Table 3, where the membrane is bounded on three sides (free TE only). Some models have multiple cells and finite spans, creating a more complicated flow field that includes spanwise effects. As before, the aerodynamic load is predicted using Eq. 27, where the lift coefficient depends on *AR* as modeled with lifting-line theory (Eq. 19). Despite the wide range of angle-of-attack, dynamic pressure, membrane properties and geometries, and four different flow facilities, the data collapse reasonably well—much better than Figs. 65 and 66. The free TE configuration exhibits a higher nondimensional frequency magnitude compared to the free LE-TE configuration—an effect of the third rigid boundary increasing stiffness. Additionally, the nondimensional frequency does not appear to rise as rapidly as the tensioning decreases. Again, for higher tension, $\Pi_2 > 2$, nondimensional frequency is relatively constant. For this data set, $f^* = 0.80 \pm 0.05$ (95%) and $f^* = 0.80 \pm 0.18$ (95%) based on the *sample mean* and *next measure*, respectively. Based on a two-sample t-test ($P < 0.001$), the difference in f^* between the free LE-TE configuration and the free TE configuration is significant.

As discussed in Zhang *et al* (2013a) for *AR* = 2 wings, the high-tensioned membranes ($\Pi_2 > 2$ and $b'/c' < 0.5$) show less improvement in lift and efficiency due to lower time-averaged cambering and lower amplitude vibration of the membrane. It is the low-tensioned membranes ($0.5 < \Pi_2 < 2$) that exhibit lift augmentation, especially in the post-stall region. In this region, similar to Fig. 72, the f^* and Π_2 are inversely related. The power law relationship is not as steep for the free LE-TE models and could be a result of the third boundary, scatter in the data set ($R^2 \sim 0.8$), or over-simplification of the aerodynamic strain assessment. To assess the latter, known experimental lift coefficient measures (from two of the four data sets) were used to calculate Π_2. Figure 74 is a replot of the data. For $\Pi_2 > 2$, $f^* = 0.84 \pm 0.05$ (95%) and 0.84 ± 0.19 (95%) based on the *sample mean* and *next measure*, respectively. The power law fit for $\Pi_2 < 2$ exhibits a steeper inverse relationship, closer to the free LE-TE configuration and a frequency trend proportional to $\sigma^{3/10}$. Thus, measured lift coefficients result in a moderate increase in nondimensional frequency of 5%.

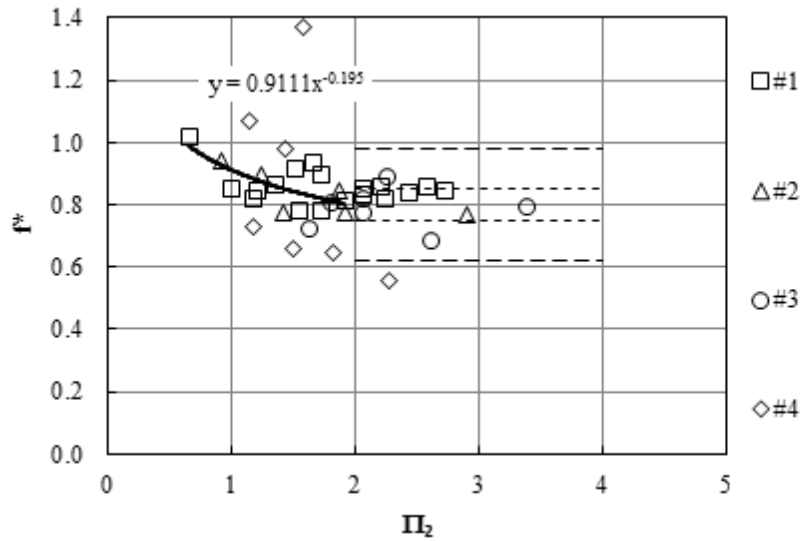**Figure 73.** Nondimensional frequency scaling results for the free TE membranes (published results from Table 3) using theoretical lift: short dashed lines represent 95% confidence interval of the *sample mean* and long dashed lines represent 95% confidence on the *next measure*
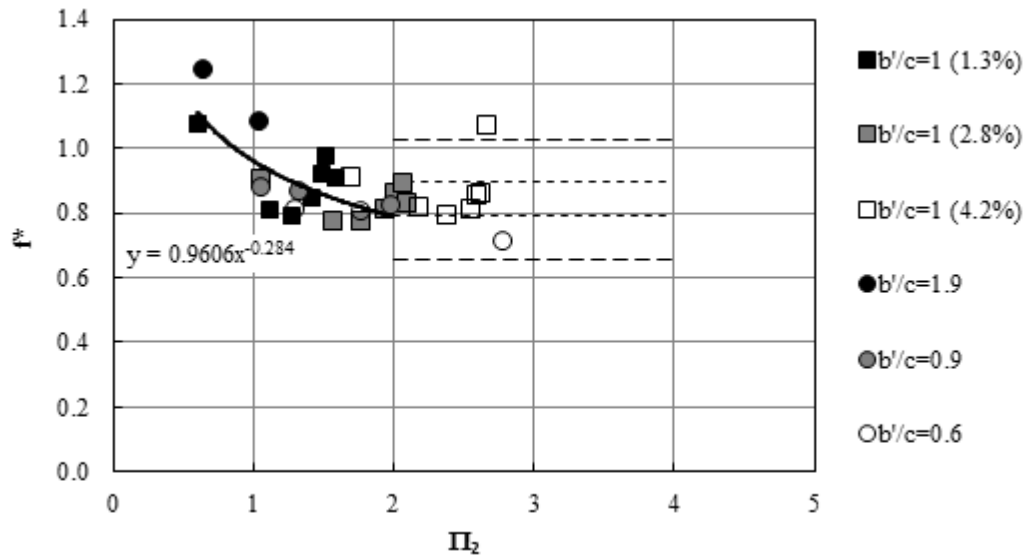

Figure 74. Nondimensional frequency scaling results for the free TE membranes (published results from Table 3) using measured lift

Conclusions

The following conclusions pertain to low-*AR* membrane wings (2 – 5) in low-*Re* flow (25,000 – 75,000) with various applied pre-strain levels (<10%). The membrane, silicone rubber, is attached to a rigid metallic frame forming multiple spanwise cells with unattached (free) trailing edges.

1. Small-amplitude membrane vibration exists prior to the onset of large, visible membrane vibration (flutter) and subsequent limit cycle oscillations at higher speeds. For this state, the corresponding energy from the low-amplitude membrane vibration is not detectable in the flow shear layer, above the broadband turbulent kinetic energy. The coherence between the membrane vibration and the flow fluctuations is low. The material, geometric and pre-stress characteristics of the membrane governs the frequency of small-amplitude vibrations that are energized by the flow but independent of flow speed.
2. Large-amplitude vibrations (or limit cycle oscillations) initiate once the membrane fluctuation energy approached or exceeded 0.01 $m^2s^{-2}Hz^{-1}$. A sharp spectral peak is easily detectable in the flow and high coherence exists between the membrane and flow measurements (laser vibrometer and hotwire anemometer). The corresponding vibration frequency increases with increased flow velocity due to aerodynamic tensioning of the membrane.
3. Time-averaged, mid-plane, streamwise velocity fields show that the growth of a separation bubble and subsequent separation into the wake is greatly reduced with smaller peak wake deficit velocities aft of the wing when compared to rigid wings. Time-resolved measurements show that the peak fluctuating streamwise and normal velocities shift closer the membrane. Additionally, counter-clockwise (positive) vorticity forming at the membrane TE sheds into the shear layer and pulls higher momentum flow above the separated region downward closer to the membrane.
4. At low angle-of-attack, the membrane's mean and fluctuating deformations are a strong function of pretension and angle-of-attack. The vibration frequency and energy correlates positively with pretension and angle-of-attack in the linear region and pre-stall region of the lift curve if the flow is predominately attached. At higher angles-of-attack, close to stall and the peak lift coefficient, the membrane vibration frequency settles to a near constant value more consistent with bluff-body shedding and becomes relatively independent of the pretension in the membrane.
5. The membrane vibration exhibits features of both a standing wave and traveling wave. Looking at the membrane in a dynamic sense, a leeside bulge of high pressure forms near the membranes leading edge; this bulge instantaneously affects the membranes camber. As the pressure builds, it then travels down the membrane where it's released at the trailing edge into a low pressure region. This process occurs during each of the membranes limit cycle oscillations.
6. The aerodynamic effect of the modified flow field is to increase lift, particularly in the post-stall region, and increase aerodynamic efficiency if the trailing edge is scalloped to reduce undesirable, low-tensioned oscillation of the trailing edge. The lift curve for the *AR* = 4 planform shows three distinct regions: a) low angle-of-attack region ($\alpha <$ ~8°) modeled effectively well with lifting-line theory because the leading-edge separation reattaches, b) a pre-stall region (~8° < $\alpha <$ ~16°) where the lift curve slope decreases substantial but still is positive (here the membrane wing has substantially more lift than the rigid planform) and c) a stall-region where the lift coefficient peaks and decreases (but still higher than the rigid planform). Aerodynamic efficiency peaks just prior to the transition between regions (a) and (b) as the lift increase attenuates and the drag amplifies.
7. The aerodynamic benefits of increased lift curve slope, increased maximum lift coefficient and increased aerodynamic efficiency persist relative to the rigid planform as the aspect ratio decreases down to *AR* = 2. The lift curve slope and maximum aerodynamic efficiency decrease with aspect

ratio; however, the stall angle increases and the maximum lift coefficient remains relatively constant.

8. Membrane wings generally outperform contoured rigid wings printed in the time-average shape of the vibrating membrane wings in two areas: lift and efficiency. The time-averaged shaped wings show lower lift generation due to effective negative geometric twist. While membrane vibration is essential for generating the additional lift and not just a time-average effect, the vibration adversely affects drag compared to the time-averaged shaped wings.

9. The optimal sizing and tension of the membrane is a cell aspect ratio of ~1 and a tension-based aeroelastic parameter, $\Pi_2 = \frac{\sigma t}{qc'}$, of ~1. Membrane vibration is significant if the cell aspect ratio is greater than 2 or Π_2 is less than 0.5. In this case the membrane wing acts like a blunt lifting-body with high drag due to the large-amplitude vibration of the loose membrane. While lift is greater than a rigid counterpart, the drag is large (drag coefficient ~ 0.3) and relatively angle-of-attack independent. When the cell aspect ratio is less than 0.5 or Π_2 is greater than 2, then the wing acts similarly to a rigid wing.

10. At pre-stall conditions, Strouhal scaling of the membrane vibration is not appropriate. Instead, the vibration of the membrane is related to its structural natural frequency which is a function of the applied pre-strain, aerodynamic strain (dynamic pressure, angle-of-attack), material properties, and geometry. A proposed tension-based scaling, when the tension is predominantly in the spanwise direction and less than 10%, is

$$f^* = fb' \sqrt{\frac{\rho_m}{(\varepsilon_o + \varepsilon_a)E}} .$$

where both the applied strain and aerodynamic strain are considered. The aerodynamic strain (assuming linearly lifting line theory—hence low angle of attack—and simplifying the pressure field as spatially constant) is proportional to the lift coefficient to the power of $^2/_3$. As such, a relationship is established between the two aeroelastic parameters where material stiffness dominates, Π_1, and membrane tension dominates, Π_2:

$$\Pi_2 = \varepsilon_o \Pi_1^3 + .348 C_l^{2/3} \Pi_1. \tag{29}$$

For highly tensioned membranes ($\Pi_2 > 2$), the nondimensional frequency is relatively constant and for lower tensioned membranes the nondimensional frequency increases as Π_2 decreases.

References

Abudaram, A, B Stanford and P Ifju (2009) "Wind Tunnel Testing of Load-Alleviating Membrane Wings at Low Reynolds Numbers," AIAA Paper 2009-1468, January.

Abudaram, YJ, PG Ifju, JP Hubner and LS Ukeiley (2013) "Controlling Pre-tension of Silicone Membranes on Micro Air Vehicle Wings," to appear *Journal of Strain Analysis*.

Aki, M, M Waszak and S Shkarayev (2006) "Development of Micro Air Vehicles with in-Flight Adaptive Wing," *Introduction to the Design of Fixed-Wing Micro Air Vehicles: Including Three Case Studies*, AIAA, Reston, VA, 241-276.

Albertani, R, B Stanford, JP Hubner and PG Ifju (2007) "Aerodynamic Characterization and Deformation Measurement of a Flexible Wing Micro Air Vehicle," *Experimental Mechanics*, 47(4):625-636.

Albertani R, P Khambatta, A Hart, L Ukeiley, M Oyarzun, L Cattafesta, and G Abate (2009) "Validation of a low Reynolds number aerodynamic characterization facility," AIAA Paper 2009-0880, January.

Anderson, JD (2011) *Fundamental of Aerodynamics*, 5th ed. McGraw-Hill, New York, 462-463.

Arce, MA, A Timpe, LS Ukeiley, JP Hubner and PG Ifju (2013) "Passively Compliant Membranes of Low Aspect Ratio Wings," 51th Aerospace Sciences Meeting and Exhibit, AIAA Paper 2013-0681, January.

Beer, F, E Johnston, E Eisenberg and D Mazurek (2007) *Vector Mechanics of Engineering: Statics 8th Ed*, McGraw Hill, Boston, 394-398.

Bendat JS, and AG Piersol (2010) *Random Data: Analysis and Measurement Procedures*, 4th ed. Wiley & Sons, Hoboken, 93-94.

Carmichael, BH (1981) "Low Reynolds number Airfoil Survey: Vol 1," *NASA CR 165803*.

Gordnier, RE and PJ Attar (2009) "Implicit LES Simulations of a Low Reynolds Number," AIAA Paper 2009-0579, January.

Hu, H, M Tamai, and JT Murphy (2008) "Flexible-Membrane Airfoils at Low Reynolds Numbers," *Journal of Aircraft*, 45(5):1767-1778.

Hubner, JP, and T Hicks (2011) "Trailing-Edge Scalloping Effect on Flat-Plate Membrane Wing Performance," *Aerospace Science and Technology*, 15(8):670-680, DOI: 10.1016/j.ast.2011.01.004.

Ifju, PG, S Ettinger, DA Jenkins and L Martinez (2001) "Composite Materials for Micro Air Vehicles," *SAMPE Journal*, 37(4):7-12.

Ifju, PG (2005) "Flexible-Wing-Based Micro Air Vehicles," *Compliant Structures in Nature and Engineering*, ed. CH Jenkins, Wit Press, Chp 8:171-192.

Ifju, PG, R Albertani, BK Stanford, DJ Claxton and MJ Sytsma (2006) "Flexible Wing Micro Air Vehicles," *Introduction to the Design of Fixed-Wing Micro Air Vehicles: Including Three Case Studies*, AIAA, Reston, VA, 185-240.

Jenkins, DA, PG Ifju, M Abdulrahim and S Olipra (2001) "Assessment of the Controllability of Micro Air Vehicles," 16th Bristol International RPV/UAV Conference, Paper 30, April.

Johnston, JW, W Romberg, PJ Attar, and R Parthasarathy (2010) "Experimental Characterization of Limit Cycle Oscillations in Membrane Wing Micro Air Vehicles," *Journal of Aircraft*, 47(4):1300-1308.

Knisely, CW, (1990) "Strouhal Numbers of Rectangular Cylinders at Incidence: A Review and New Data," *Journal of Fluids and Structures*, 4(4):371–393.

Laitone, EV (1997) "Wind Tunnel Tests of Wings at Reynolds Numbers below 70000," *Experiments in Fluids*, 23:405-409.

Lian, Y, and W Shyy (2006) "Laminar-Turbulent Transition of a Low Reynolds Rigid or Flexible Airfoil," AIAA Paper 2006-3051, June.

Lissaman, PBS (1983) "Low Reynolds Number Airfoils," *Annual Review of Fluid Mechanics*, 15:223-239.

Madhani, A (2008) "Spy birds and bugs may have place in U.S. battle and rescue operations," *San Diego Tribune*, AP News, October 2.

Mastramico, N, and JP Hubner (2008) "A Study of Separation Reattachment on Membrane Flat and Cambered Plates," AIAA Paper 2008-4369, June.

Miller, M (2007) Keynote Address at the 2007 Northwest Florida MAV Workshop, July.

Mueller, TJ, JC Kellogg, PG Ifju and SV Shkarayev (2006) *Introduction to the Design of Fixed-Wing Micro Air Vehicles: Including Three Case Studies*, AIAA, Reston, VA, 1-287.

Mueller, TJ (1999) "Aerodynamic measurements at Low Reynolds Numbers for Fixed Wing Micro-Air Vehicles," *VKI Special Course*.

Okamoto, M, and A Azuma (2011) "Aerodynamic characteristics at low Reynolds numbers for wings of various planforms," *AIAA Journal*, 49(6):1135-1150.

Prasad A (2000) "Particle image velocimetry," *Current Science,* 79(1):51-60.

Rae, A, and WH Pope (1984) *Low-speed Wind Tunnel Testing*, 2nd ed., Wiley & Sons, New York, 364-374, 419-424.

Rojratsirikul, P, Z Wang and I Gursul (2009) "Unsteady Fluid–Structure Interactions of Membrane Airfoils at Low Reynolds Numbers," *Experiments in Fluids*, 46(5):859-872.

Rossing, TD, and NH Fletcher (1995) *Principles of Vibration and Sound*, Springer-Verlag, New York, 63-67.

Schreier, H, J Braasch and M Sutton (2000) "Systematic Errors in Digital Image Correlation Caused by Intensity Interpolation," *Optical Engineering,* 39(11):2915-2921.

Scott, KD, JP Hubner and LS Ukeiley (2012) "Cell Geometry and Material Property Effects on Membrane and Flow Response," *AIAA Journal*, 50(3):755-761.

Seide, P (1978) "Large Deflections of Rectangular Membranes under Uniform Pressure," *International Journal of Non-linear Mechanics*, 12:397-406.

Shindo S (1995) "Simplified tunnel correction method," *Journal of Aircraft*, 32(1):210-213.

Shyy, W, DA Jenkins and RW Smith (1997) "Study of Adaptive Shape Airfoils at Low Reynolds Number in Oscillatory Flows," *AIAA Journal*, 35(9):1545-1548.

Shyy, W, PG Ifju and D Viieru (2005) "Membrane Wing-Based Micro Air Vehicles," *Applied Mechanics Reviews*, 283-301.

Shyy, W, Y Lian, J Tang, D Viieru, and H Liu (2007) *Aerodynamics of Low Reynolds Number Flyers*, Cambridge University Press, Cambridge.

Song A, X Tian, E Israeli, R Galvao, K Bishop, S Swartz and K Breuer (2008) "Aeromechanics of membrane wings with implications for animal flight," *AIAA Journal*, 46(8):2096-2106.

Stanford, B, R Albertani and P Ifju (2007) "Static Finite Element Validation of a Flexible Micro Air Vehicle," *Experimental Mechanics*, 47(2):283-294.

Stanford, B, P Ifju, R Albertani and W Shyy (2008) "Fixed Membrane Wings for Micro Air Vehicles: Experimental Characterization, Numerical Modeling, and Tailoring," *Progress in Aerospace Sciences*, 44:258-294.

Sutton, M, M Cheng, W Peters, Y Chao and S McNeill (1986) "Application of an Optimized Digital Correlation Method to Planar Analysis," *Image and Vision Computing,* 4(3):143-151.

Swartz, S, J Iriaite-Diaz, D Riskin, A Song, X Tian, D Willis and K Breuer (2007) "Wing Structure and the Aerodynamic Basis of Flight in Bats," AIAA Paper 2007-0042, January.

Timpe, A, Z Zhang, JP Hubner and L Ukeiley (2013) "Passive Flow Control by Membrane Wings for Aerodynamic Benefit," *Experiments in Fluids*, 54, DOI 10.1007/s00348-013-1471-0.

Tregidgo L, Z Wang and I Gursul (2011) "Fluid-structure interactions for a low aspect-ratio membrane wing at low Reynolds numbers," AIAA-2011-3436, June.

Torres, GE, and TJ Mueller (2004) "Low-Aspect Ratio Wing Aerodynamics at Low Reynolds Numbers," *AIAA Journal*, 42(5):865-873.

Wahidi, R, Z Zhang and JP Hubner (2012) "Volumetric Three-Component Measurements of the Flowfield Around Low-Aspect Ratio Flat and Periodic Cambered Plates," 50th Aerospace Sciences Meeting and Exhibit, AIAA Paper 2012-0049, January.

Wilson, JR (2009) "UAV Worldwide Roundup—2009," *Aerospace America*, April:30-36.

Zhang, Z, JP Hubner, LS Ukeiley, Y Abudaram and PG Ifju (2012) "Effect of Aspect Ratio on Flat-Plate Membrane Airfoils," 50th Aerospace Sciences Meeting and Exhibit, AIAA Paper 2012-1084, January.

Zhang, Z, N Martin, A Wrist, JP Hubner, Y Abudaram, L Ukeiley and PG Ifju (2013) "Force and Deformation Measurement of Low Aspect Ratio Membrane Airfoils," 51th Aerospace Sciences Meeting and Exhibit, AIAA Paper 2013-0682, January.

Zhang, Z, L Hopper, A Wrist, JP Hubner and L Ukeiley (2013) "Nondimensional Frequency Scaling of Aerodynamically-Tensioned Membranes," in review *Journal of Fluids and Structures*, Presentation: SEM 2013 Annual Conference and Exposition, Paper 443, June.

Appendix

Funded Student Participation

Graduate Students

        Amo Timpe, MS 2012

        Alex Arce, MS expected 2013

        Yakkov Abudaram, PhD expected 2013

        Zheng Zhang, PhD expected 2014

Undergraduate Students

        Kyle Scott, BS 2012

        Alex Jordan, BS 2012 (via NSF REU program)

        Anderson Lovelace, BS 2013

        Nathan Martin, BS 2013 (via NSF REU program)

        Andrew Wrist, BS expected 2014